



university of  
groningen

# Self-Assembly and Ion-Conduction in PS-*b*-PEO: A computational study

Master Thesis

by  
Fabian Grünewald  
born on 5 February 1995  
in Ahaus Germany

8th July 2018

Supervisor:  
Dr. Siewert-Jan Marrink

Assessors:  
Dr. Siewert-Jan Marrink  
Dr. Giuseppe Portale

# Contents

<b>Acknowledgments</b>	<b>i</b>
<b>1 Introduction</b>	<b>1</b>
1.1 Scope	2
1.2 Solid Polymer Electrolytes	3
1.3 Molecular Dynamics	5
1.3.1 The Force-Field	5
1.3.2 Sampling & Ensemble	7
1.3.3 Error Estimation and Convergence	9
1.4 The MARTINI Force-Field	10
1.4.1 MARTINI polymer models	11
<b>2 A transferable MARTINI model of polyethylene oxide</b>	<b>17</b>
2.1 Summary	18
2.2 Introduction	18
2.3 Methods	20
2.3.1 Free Energy Calculations	21
2.3.2 CG simulations of PEO systems	23
2.4 Results and Discussion	26
2.4.1 Parametrization of PEO and associated compounds	26
2.4.2 Validation of the new model	34
2.5 5.0 Conclusions	46
<b>3 MARTINI model for Lithium Bistriflimide</b>	<b>51</b>
3.1 Summary	52
3.2 Introduction	52
3.3 Methods	53
3.4 Atomistic Model	56
3.4.1 Charges and Atom-Types	56

3.4.2	Dihedral Potential TFSI . . . . .	58
3.4.3	Lithium TFSI interaction energy . . . . .	60
3.5	MARTINI LiTFSI . . . . .	62
3.5.1	Mapping and Bonded Interactions . . . . .	63
3.5.2	Non-bonded interactions . . . . .	64
3.5.3	Conclusion . . . . .	67
<b>4</b>	<b>Self-Assembly and Charge Transport of LiTFSI in PS-b-PEO</b>	<b>71</b>
4.1	Introduction . . . . .	72
4.2	Methods . . . . .	74
4.2.1	CG-simulations . . . . .	74
4.2.2	Quantifying Phase-Separation . . . . .	76
4.2.3	Quantifying Salt Distribution . . . . .	77
4.3	Self-Assembly . . . . .	78
4.3.1	Effect of Time and Concentration . . . . .	80
4.3.2	Correlation Salt Phase-Separation . . . . .	81
4.3.3	Annealing . . . . .	82
4.4	Transport Properties . . . . .	86
4.5	Conclusion & Outlook . . . . .	87
<b>A</b>	<b>Polymer Structures</b>	<b>93</b>
<b>B</b>	<b>2016H66 with the Verlet cut-off scheme and modifiers</b>	<b>95</b>
<b>C</b>	<b>Error and Convergence Estimation</b>	<b>101</b>
<b>D</b>	<b>Estimating the radius of gyration at low molecular weights</b>	<b>107</b>
D.0.1	Extrapolation from high molecular weights . . . . .	107
D.0.2	Estimation based on intrinsic viscosity data . . . . .	107
<b>E</b>	<b>Brush and Mushroom dimensions for PEG grafted to a lipid bilayer</b>	<b>113</b>
E.1	Mushroom dimensions . . . . .	113
E.2	Brush dimensions . . . . .	114
E.3	Estimating the Kuhn Length . . . . .	115
<b>F</b>	<b>Dimension and Aggregation Number of Micelles</b>	<b>119</b>

# Acknowledgments

The big art in writing a scientific publication lies (presumably) in presenting results in an objective way while not boring the reader to death. By this standard the acknowledgment section should be the most easy to write. It comprises all the thanks to fellow researcher, family and the people we hold most dear. But it appears to be a common standard among scientists to find this part of the thesis the most difficult to write. I do not present an exception to this trend. There are so many things left to say, people to thank and experiences of non-scientific nature worthy of mentioning that it seems impossible to put them all on paper and not write another thesis. The following presents my attempt to this challenge. I would like to thank:

- Siewert-Jan and Alex not only for their support with the research and the many insightful discussions about MD and science, but also for their trust and relaxed way in which research is organized in their group. I am looking very forward to continue working in the group.
- Luca for welcoming me to Lyon and the intensive work as well as resources spent on the new PEO model. Besides that I am also grateful for the many good book recommendations and introduction to the French cuisine.
- Remco and Ria for their scientific and administrative support relating to the TCCM program; and the many interesting discussions on quantum mechanics.
- Jeremy for welcoming me in his lab in Leuven and helping with the research despite the fact that my model for the largest part ignores the existence of electrons.

- Jonathan, who in my opinion is one of the most patient and helpful rubber-duck debuggers known in the world. I am very thankful for all the help with putting my insane ideas into (mostly) sane python code.
- Riccardo, for very insightful discussions on self-assembly, computer modeling and the communication problems between theoreticians and experimentalists.
- Tsjerk, for the unvarnished truth (or his opinion?) on my figures, design and layout; but even more for helping to improve the aforementioned.
- Paulo, for his patience in explaining the inner workings of MARTINI and the interesting discussions on how to coarse-grain a single bare ion that is just a little larger than  $H^+$ .
- finally, my family for always supporting me. I am especially very grateful for all the help and patience related to my frequent moves for this work; in addition my brother deserves special thanks for finding time to read and spell-check the thesis.

This work is supported by:



**university of  
groningen**



Co-funded by the  
Erasmus+ Programme  
of the European Union

**KU LEUVEN**



*TCCM*





# Chapter 1

## Introduction

“ *You can know the name of a bird in all the languages of the world, but when you’re finished, you’ll know absolutely nothing whatever about the bird... So let’s look at the bird and see what it’s doing – that’s what counts.*

”

---

Richard P. Feynman,

## Scope

This thesis describes an attempt to simulate and characterize the self-assembly of the block-copolymer system polyethylene oxide (PEO) and polystyrene (PS) in the presence of Lithium Bistriflimide (Li[TFSI]) salt. The self-assembly is modeled using molecular dynamics (MD) with the MARTINI force-field. The MARTINI force-field employs a coarse-grained but explicit description for all system components. As such it is one of the first attempts to simulate this self-assembly process without resorting to a mean-field type description of the system at any level. A second focus of this thesis is devoted to the advantages and limitations of using MARTINI for simulating polymer systems. In this context a new MARTINI model for PEO is presented as well as software for facilitating high throughput sampling.

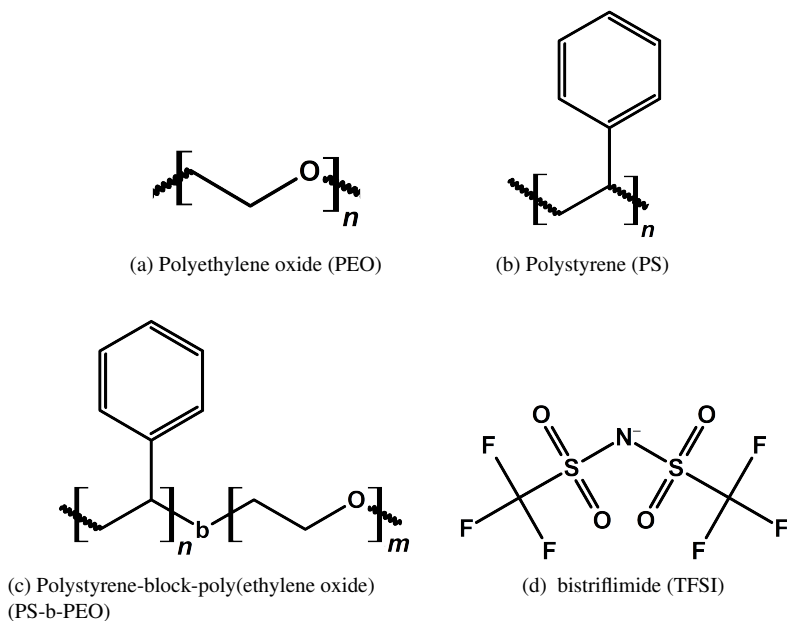


Figure 1.1: Chemical structures of PEO (a), PS (b), PS-b-PEO (c) and TFSl (d)

## Solid Polymer Electrolytes

Since the introduction of the Lithium-ion battery (LIB) by Sony 1991<sup>2</sup> LIBs have become ubiquitous in modern day life. LIBs are not only powering almost every mobile device on the planet, but also become more and more important in the context of renewable energies. Although the recent completion of a 100 mega-watt LIB based energy storage facility in Australia demonstrates the possibility of using LIBs for large scale storage, problems remain<sup>3</sup>; the electrolyte in current LIBs is highly flammable and toxic<sup>4</sup>. The seriousness of these risks involved is highlighted by a recent event: The LIB electrolyte in a faulty smart-phone caught fire upon charging. As consequence the manufacturer had to recall 2.5 million phones causing an estimated loss of \$ 5.3bn.<sup>5</sup> Fortunately no serious injuries were sustained by the users. However, smart-phone batteries are small compared to those used in for instance electric cars. Therefore one of the primary targets in battery research is the development of safe, sustainable and easy to manufacture electrolytes.

Since 1975, it is known that the polymer polyethylene oxide (PEO) can conduct Lithium ions at a comparatively high rate.<sup>6</sup> Whereas PEO would be a safe and easy to produce electrolyte, the mobility is intimately connected to the chain flexibility; only above the glass-transition temperature high conductivities are measured. For the application in batteries this is a major drawback, because above the glass-transition the shear modulus is low. Thus Lithium crystals can form and join to dendrites short circuiting the battery.<sup>2</sup> To overcome this problem PEO can be covalently linked to another polymer yielding a block-copolymer. Given sufficient length the

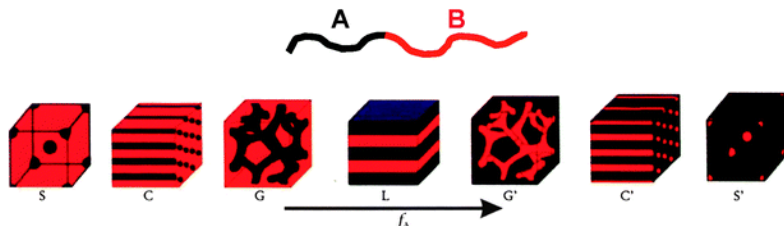


Figure 1.2: Schematic drawing of phase-separation of block-copolymers composed of the polymers A and B with decreasing amount of B in the chain; taken from<sup>1</sup>

two polymers will phase-separate and self-assemble into a material with domains of pure PEO and the other polymer (see Figure 1). The other polymer (e.g polystyrene) is normally non-conducting and used to increase the mechanical strength. At the same time one hopes that the ion conduction through the PEO domain remains mostly unaffected. The aim is to retain the good conduction properties of PEO, while increasing the mechanical strength (i.e. the shear modulus).

There are numerous experimental studies, which demonstrate that the conduction behavior observed in pure PEO is changed by adding the second polymer.<sup>27</sup> Normally it is found to be lower than in the homo-polymer. However, some peculiar phenomena are observed: For PS-*b*-PEO for instance the conduction is seen to decrease with molecular weight until a turning point is reached from which onwards it increases and finally starts oscillating.<sup>8</sup> This effect is in part contributed to zones near the interface where conduction is hindered. If these zones are about equal the lamellae thickness conduction is low and decreases with molecular weight. In turn once these zones are larger conduction increases with molecular weight.<sup>9,8</sup> In one of the first computational studies with a multi-scale coarse-grained atomistic resolution approach it was observed that less Lithium ions reside near the interface. This supports this hypothesis.<sup>10</sup> On the other hand for the same system (PS-*b*-PEO) Young and coworkers reported that the conductivity in cylindrical phases is larger than in lamellar phases. This is the case even though the conducting PEO phase in the cylindrical arrangement is much smaller and their values have been corrected for grain boundaries between the lamellae.<sup>11</sup>

Except for some examples<sup>10,12,13</sup> there are few fundamental theoretical studies focusing on the conduction mechanism and self-assembly of these block-copolymer SPEs. However, understanding both these processes is the first step towards predicting the conductivity of new unknown block-copolymer SPEs. Reliable predictions enable the rational choice of new and better materials; this reduces both the cost and time of developing block-copolymer SPEs with high conductivity compared to surveying many candidate materials in the lab.

## Molecular Dynamics

In the field of chemistry a theoretical understanding and description of chemical systems is a necessary supplement to experimental investigations. Historically, theoretical chemistry has its origins in the field of quantum mechanics. The laws of quantum mechanics govern how molecules move, transform and interact with their environment. Understanding and describing a chemical system therefore requires to be able to treat molecules at a full quantum mechanical level. However, a full quantum mechanical treatment is impossible for all but the smallest molecules. Only by employing approximations one is able to theoretically treat and understand larger chemical systems. Hence the art of approximation is what defines the field of theoretical chemistry; good approximations simplify the description in a way that retains the essential physics of the system while sufficiently reducing the computational effort.

The method Molecular Dynamics (MD), sometimes also referred to as Molecular Mechanics (MM), can be regarded as such an approximation. Treating molecules by MD means describing the interactions and movements between molecules by classical mechanics; transformations (i.e. chemical reactions) are usually neglected. Despite omitting any quantum phenomena in the description, it has been shown over the past two decades that MD is able to yield accurate thermodynamic properties and phenomena related.<sup>14</sup> For example free energies or phase behavior of soft matter can be accurately reproduced by MD, while the QM description is far out of reach. However, due to the omission of any quantum mechanical detail, two choices are of the uppermost importance when performing MD: The choice of the ensemble under which to conduct the simulation is equally important as the choice of the force-field.

### The Force-Field

The force-field defines the interaction rules for the simulation. It is common to divide the contributions to the potential energy into bonded interaction terms and non-bonded interaction terms (cf. eq. 1.1).

$$V_{total} = V_{bonded} + V_{non-bonded} \quad (1.1)$$

Bonded interactions usually account for the degrees of freedom related to chemical bonding. In order to maintain the equilibrium structure of a

molecule one uses simple potentials as function of the bond length, angles and dihedral angles.

$$V_{bonded} = V_{bonds} + V_{angles} + V_{dihedral-angles} \quad (1.2)$$

These simple potentials are often in the form of the harmonic oscillator potential (cf. eq. `refeq:simharmon`) for bonds and angles; dihedral angles are treated by a variety of potential functions most commonly in form of cosine dependent potentials (e.g. eq. 1.4).

$$V_{harmon.-bond} = \frac{1}{2} k_B \times (r_i - r_{ref})^2 \quad (1.3)$$

$$V_{dih.} = k_{dih} \times (1 + \cos(n\phi - \phi_{ref})) \quad (1.4)$$

Non-bonded interactions on the other hand are used to represent the interactions between molecules and fragments or distant atoms within a molecule. It is common to divide non-bonded interactions into an electrostatic term and a term representing dispersive interactions. The electrostatic term is often described by the Coulomb potential (cf. eq. 1.6), while the dispersive term given by a Lennard-Jones (LJ) potential (cf. 1.5). Sometimes a special term accounting for polarization is included.

$$V_{LJ} = 4\epsilon \times \left( \left( \frac{\sigma_{i,j}}{r_{i,j}} \right)^{12} - \left( \frac{\sigma_{i,j}}{r_{i,j}} \right)^6 \right) \quad (1.5)$$

$$V_{coulomb} = \frac{1}{4\pi\epsilon_0\epsilon} \times \frac{q_i q_j}{r_{i,j}} \quad (1.6)$$

Each force-field normally has its own procedure for determining both non-bonded and bonded interactions for a specific molecule. Nevertheless, it is common practice to use a cut-off for both the Lennard-Jones and Coulomb interactions in order to reduce the computational effort. The neglected interactions are in turn often compensated by correction schemes. Correction schemes for electrostatic interactions are most notably the reaction-field method and the Particle-Mesh-Ewald (PME) summation technique; the missing Lennard-Jones interactions are only rarely accounted for, although similar techniques exist (e.g. LJ-PME). As the interaction energy is strongly depending on both cut-off and correction schemes, they should both be regarded as fixed parts of the force-field. Any changes should be verified to yield acceptable properties before usage. The same holds for combining parameters from different force-fields.

## Sampling & Ensemble

All MD simulations are intimately related to the choice of the ensemble. In a qualitative sense the ensemble of an MD simulation represents the conditions (constant pressure, constant temperature, constant concentration etc.) under which a simulation is conducted; these conditions are in general similar to the conditions under which corresponding experiments are conducted. Most of the time the appropriate ensemble is characterized by constant pressure, number of particles and temperature (i.e. the isobaric-isothermal ensemble).

More formally any MD simulation is governed by the laws of statistical mechanics.<sup>14</sup> As a consequence the system is not characterized by lowest potential energy but rather the free energy (cf. eq. 1.7).<sup>14</sup> The free energy in turn is given by the negative Boltzmann constant ( $-k_B$ ) times temperature and times the natural logarithm of the partition function  $Q(N, V, T)$ . Equations 1.7 to 1.8 show this connection for the constant particle, temperature, volume case (i.e. canonical ensemble).<sup>15</sup>

$$F = -k_B T \times \text{Ln}[Q(N, V, T)] \quad (1.7)$$

$$Q(N, V, T) = \sum_j \Omega(N, V, E) \times e^{-\frac{E_j(\mathbf{p}, \mathbf{r})}{k_B T}} \quad (1.8)$$

Equation 1.8 is a sum over the exponent of the energy ( $E_j$ ) of all QM levels of the system divided by  $k_B T$ ;  $\Omega$  is the degeneracy of each level. In the classical approximation (appropriate here) the potential energy can be defined purely in terms of the momenta and positions of the particles.<sup>1</sup> Thus  $E_j$  represents a state in which the particles have one specific configuration of momenta and coordinates. Following this line of reasoning we see that the free energy is dependent on a set (or ensemble) of configurations, which have a high Boltzmann weight. Other ensembles might depend in addition on other quantities. For example the isobaric-isothermal partition function (cf.1.9 ) reveals that the configurations and free energy also depend on the

---

<sup>1</sup>For the sake of completeness: In the classical limit one can substitute the sum in equation 1.8 by a multidimensional integral over all momenta and coordinates. Furthermore one has to account for dimensionality and indistinguishability by a factor of  $(h^d N!)^{-1}$ , where  $h$  is Planck's constant and  $d$  the dimensionality (usually 3). This leads to the formally correct partition function in the classical limit<sup>14</sup>:

$$Q(N, V, T) = \frac{1}{h^d N!} \times \int \int e^{-\frac{E(\mathbf{p}, \mathbf{r})}{k_B T}} d\mathbf{r} d\mathbf{p}$$

pressure.

$$\Delta(N, p, T) = \sum_j \Omega(N, V, E) \times e^{-\frac{E_j(\mathbf{p}, \mathbf{r})}{k_B T}} \times e^{-\frac{Vp(j)}{k_B T}} \quad (1.9)$$

We have established: A system in a MD simulation is macroscopically defined by the free energy. The free energy depends on an ensemble of configurations of momenta and positions. Consequently any observable  $A$  is formally obtained as an ensemble average (cf. 1.10).<sup>14</sup>

$$\langle A(\mathbf{p}, \mathbf{r}) \rangle = \frac{\int \int A(\mathbf{p}, \mathbf{r}) \times e^{-\frac{E_j(\mathbf{p}, \mathbf{r})}{k_B T}} d\mathbf{p} d\mathbf{r}}{\int \int A(\mathbf{p}, \mathbf{r}) d\mathbf{p} d\mathbf{r}} \quad (1.10)$$

To obtain a meaningful ensemble average by MD all relevant configurations should have been sampled. The space spanned by all relevant configurations is also referred to as phase space. If the phase space is sufficiently explored, sampling is good enough.

From a sampling point of view observables from MD simulations may be divided into two categories: (1) qualitative observations, and (2) numerical observables. (1) Qualitative observations can be made by visually inspecting the MD trajectory. For example, the formation of a lipid-bilayer from initially random lipids in water is such an observation. Another example would be the types of phases observed for different concentrations of non-ionic surfactants in water (see chapter 2.4). Both these observations have in common that no mathematical analysis has to be performed after the simulation: What one sees is what one gets. With the exception of kinetically trapped structures, sampling is sufficient once a structure is observed and stable in time. (2) Numerical observables, in contrast, are formally ensemble averages, calculated from the positions, energy or forces recorded during an MD simulation. However, in general we treat these ensemble averages as averages over time, since we assume they are equivalent in the limit of sufficient sampling. This assumption is also known as the ergodic hypothesis.<sup>16</sup>

$$\langle A(\mathbf{p}, \mathbf{r}) \rangle = \frac{1}{T_{total}} \sum_t^N A(\mathbf{p}, \mathbf{r})_t \quad (1.11)$$

## Error Estimation and Convergence

In the previous chapter we established that we can write ensemble averages as time averages in the limit of sufficient sampling. However, two important aspects remain: We need to assess when sufficient sampling has occurred and determine an error in the observed variable. Both aspects are closely related and in fact computing the error can be used as measure for sampling.

The error of an ensemble average obtained from MD is not representative of the true error, because MD simulations produce correlated data sets.<sup>17</sup> It can be shown that the standard-error in the mean (SEM) of the true uncorrelated data set is larger than those of the correlated data set by a factor of  $g$ . The quantity  $g$ , called the statistical inefficiency, is a measure for how much smaller an uncorrelated data set is, with respect to the correlated data set.<sup>17</sup> Stated differently:

$$N_{\text{uncorrelated}} = \frac{N_{\text{correlated}}}{g} \quad (1.12)$$

Thus,  $g$  provides a connection between the correlated data set obtained directly by MD and the corresponding uncorrelated data set. To estimate the error in an observable such as the radius of gyration, one can now first estimate  $g$ . Subsequently, to obtain an approximate uncorrelated data set, the original data set is sub-sampled at intervals of length  $n \times g$ . In this case  $n$  is increased by 1 until the length of the data set is exceeded. Finally the average and standard error of this uncorrelated data set should be equivalent to those of the ensemble average.<sup>18 19</sup> <sup>II</sup> Since  $g$  is also related to the dominant autocorrelation time of the system by:<sup>21</sup>

$$g = 1 + 2 \tau \quad (1.13)$$

we can use the same procedure to assess convergence. Obtaining sufficiently many uncorrelated samples (i.e. the ratio is large) ensures, at least in principle, that the simulation is longer than the autocorrelation time. Unfortunately, molecular systems in general, but also simulations of polymers in particular, can have multiple long autocorrelation times. However, the method for estimating assumes per default, that there are sufficiently

---

<sup>II</sup>This protocol is itself already part of the pymbar package. It follows the implementation for free energy calculations by Shiels and Chodera.<sup>18 19</sup> In almost all cases tested here (see Appendix C), the error estimate was found to be identical to the one obtained by the method suggested by Hess<sup>20</sup>, which is implemented in the "gmx analyze" utility provided with the GROMACS package.

many samples. In other words, in cases of large under sampling, one may obtain a smaller autocorrelation time than the one relevant for the system. To combat this problem, one can plot the mean with error-bar as fraction of simulation time as well as the estimate of autocorrelation and monitor convergence.<sup>14</sup>

## The MARTINI Force-Field

The MARTINI force-field<sup>22</sup> is one of the most commonly used force-fields for coarse-grained bio-molecular simulations. However, it has also been successfully applied to a variety of synthetic and bio polymers. A molecule within the MARTINI force-field is modeled by a set of building blocks (beads). Each bead represents about 4 heavy atoms of the molecule and multiple beads are joined by bonds, angles and dihedral angles to make up the full molecule. The non-bonded interactions between beads are modeled by Lennard-Jones (LJ) potentials. In addition if the bead represents a charged group, a full charge is assigned to the bead; except for such case MARTINI does not employ partial charges.<sup>22</sup>

The non-bonded LJ interactions between beads are defined through an interaction matrix, which has 10 levels. Each level has a specific value of  $\epsilon$ , which goes from strongly interacting ( $\epsilon=5.0kJ \times mol^{-1}$ ) to repulsive interactions ( $\epsilon=2.5 kJ \times mol^{-1}$ ). On the other hand there are only two values used for  $\sigma$ . A  $\sigma$  value of 0.47 nm is used for linear unbranched groups of 4 heavy atoms, whereas a value of 0.43 nm is used for 3 or less atoms and branched or ring like moieties. A combination of  $\sigma$  and  $\epsilon$  is referred to as the type of a bead. Bead types with a  $\sigma$  value of 0.47 are referred to as normal beads and have 10 labels divided in four categories. Each category represents chemical moieties of different polarity ranging from charged (Q), polar (P) and neutral (N) to hydrophobic (C). Bead types with  $\sigma=0.43$  nm are referred to as small beads; their interaction levels are scaled by 0.75 with respect to the normal beads and their labels get a prefix S (e.g. SQ).<sup>22</sup>

In order to obtain a set of bead types for a molecule, the molecule first needs to be divided into small fragments each represented by a bead. Subsequently the bead types are selected such that the partition free energy of the molecule is reproduced within  $2.5 kJ \times mol^{-1}$ . For more complex molecules such as proteins or polymers, the partitioning of small molecules

reminiscent of the fragment within the complex molecule are often used as basis for selecting the bead type. Bonded interactions are usually determined such that their distribution matches atomistic reference distributions. Since the MARTINI bonds, angles and dihedral angles do not represent one-to-one their atomistic counterparts, the CoM of a bead is used to generate the reference distributions.

## MARTINI polymer models

The MARTINI force-field has been successfully applied to many biomolecular systems ranging from complex plasma membranes<sup>23</sup> with more than 63 different lipid types over DNA<sup>24</sup> to even proteins<sup>25</sup>. However, MARTINI has also been used in the context of polymer simulations. Some of the polymers which have been used in MARTINI are listed in table 1.1. Table 1.1 also shows which of the models employ a non-standard bead-type (i.e. uses a modified bead). Out of the 12 models considered here, 6 use non-standard bead types. These non-standard bead types were introduced, because no sufficient agreement with reference data could be achieved by only using the standard MARTINI beads. This fact illustrates: when using MARTINI for simulating polymers, it should at least be checked that polymer properties are in reasonable agreement with reference data.

Through their pioneering<sup>35 26 27 36 31</sup> work Rossi and coworkers have established rules of good practice for simulating polymers with MARTINI. Extending these based on the results and experiences presented in chapter 2 yields the following guidelines:

- First, the free energy of transfer of a single repeat unit or a representative compound should be in agreement with the value obtained from experiment or atomistic simulations.
- Furthermore, the polymer should display correct long-range structural properties (e.g. radius-of-gyration, end-to-end distance).
- Moreover, it is desirable to verify to what extent the polymer model can be transferred between different environments (i.e. solvents). Usually MARTINI is used with water as solvent. However, polymers are also frequently used with apolar organic solvents. Such transferability has been a problem especially with the previous models of PEO as outlined in chapter three. Therefore special awareness should be given to the fact that a polymer model can be good in water but bad in other environments.

Table 1.1: MARTINI Polymer Models

Polymer	repeat unit	modified*	ref.
Polyethylene Glycol (PEO)	$-\text{[O} - \text{CH}_2 - \text{CH}_2\text{]}_n-$	yes	this work
Polyethylene (PE)	$-\text{[CH}_2 - \text{CH}_2\text{]}_n-$	no	26
Polypropylene (PP)	$-\text{[CH} \begin{array}{c} \text{CH}_3 \\   \end{array} - \text{CH}_2\text{]}_n-$	no	26
Polystyrene(PS)	$-\text{[CH} \begin{array}{c} \text{C}_6\text{H}_6 \\   \end{array} - \text{CH}_2\text{]}_n-$	yes	27
Polypropylene oxide (PPO)	$-\text{[O} - \text{CH} \begin{array}{c} \text{CH}_3 \\   \end{array} - \text{CH}_2\text{]}_n-$	yes	28
Polystyrene sulfonate (PSS)	$-\text{[CH} \begin{array}{c} \text{SO}_3^- \\   \\ \text{C}_6\text{H}_4 \\   \end{array} - \text{CH}_2\text{]}_n-$	yes	29
Poly acrylic-acid (PAA)	$-\text{[CH} \begin{array}{c} \text{COOH} \\   \end{array} - \text{CH}_2\text{]}_n-$	no	30
Poly diallyl-dimethylammonium (PDADMA)	appendix A	no	29
Polyester (resin)	appendix A	no	31
Polysaccharide(s)	appendix A	yes**	32
Poly(3-hexylthiophene (P3HT)	appendix A	no	33
Chitosane	appendix A	yes	34

\* modified: one or more non-standard bead types have been developed

\*\* as result of the deficiencies of regular MARTINI an extension of the force-field was presented

- Finally, in the case where special beads are used compatibility needs to be verified. Often special beads are only parametrized to work in a specific system environment with a limited number of normal beads. Using the same model in a different system with other beads can lead to undesired artifacts. Artifacts are often the consequence of non-verified interactions between special beads and normal beads.

When applying these guidelines MARTINI polymers can have significant advantages over other coarse-grained polymer. One of the biggest assets of MARTINI is the transferability and compatibility with other compounds. The scope of other coarse-grained force-fields<sup>10,37</sup> recently used in simulations of polymers in the context of SPEs is only limited. In contrast MARTINI systems can be readily be combined with other materials such as carbon-nanotubes<sup>38</sup>, lipid-bilayer membranes<sup>39</sup> or gold-clusters<sup>40</sup> without much additional parametrization. Furthermore the building-block approach allows for a simple procedure to construct block-copolymers or polymer derived compounds (e.g. PEGylated lipids). In the context of this work (simulating the self-assembly of PS-b-PEO in the presence of LiTFSI), MARTINI is the only coarse-grained force-field (the author is unaware of any other), which combines an explicit polymer model with explicit salts and explicit solvent models.

Looking into the future there is still some room for improving MARTINI polymer models.

- **Consistent parametrization** is one of the most important improvements in the view of the author. At the moment the verifications used for the MARTINI polymer models are very heterogeneous and limited. For example, the PS model is verified in terms of radii of gyration in different solvents, temperature transferability, end-to-end distance.<sup>27</sup> In contrast the model for acrylic acid has only been shown to form vesicles (when combined with PS in water) that are in good agreement with experiment.<sup>30</sup> To ensure comparability and transferability a minimum standard of parametrization and verification would be desirable.

- **A data-bank of monomers** of the most common commercial polymers would be an extension of this concept. It would allow for the systematic exploration of polymer properties in MARTINI in comparison to experiment. In addition it could give insight into which properties of polymers MARTINI can reproduce without difficulties and which are problematic. The problematic ones in turn could be targets for a force-field optimization.
- **Combination with theory** in polymer physics could be another interesting and insightful step. One aspect could be to search a relationship between MARTINI interaction parameters and the Flory-Huggins interaction parameter ( $\chi$ ).  $\chi$  is reminiscent of the second virial coefficient and in the frame-work of Flory-Huggins theory accounts for solvent-polymer and polymer-polymer interactions. In previous simulations the LJ interactions have been directly obtained from this parameter. Because  $\chi$  is experimentally accessible and measured for many polymer-polymer and solvent-polymer couples, finding a relationship could speed up parametrization drastically.
- **A flexible program** for setting up complex polymer simulations similar to those programs available for lipids, could potentially be a route to high-throughput sampling of polymers with MARTINI.

# References

- [1] Mai, Y.; Eisenberg, A. *Chemical Society Reviews* **2012**, *41*, 5969–5985.
- [2] Xue, Z.; He, D.; Xie, X. *J. Mater. Chem. A* **2015**, *3*, 19218–19253.
- [3] McCurry, J. *The Guardian UK - online* **2017**,
- [4] Hammami, A.; Raymond, N.; Armand, M. *Nature* **2003**, *424*, 635–636.
- [5] Parkinson, G. *The Guardian UK - online* **2018**,
- [6] Wright, P. V. *Polymer International* **1975**, *7*, 319–327.
- [7] Young, N. P.; Devaux, D.; Khurana, R.; Coates, G. W.; Balsara, N. P. *Solid State Ionics* **2014**, *263*, 87–94.
- [8] Yuan, R.; Teran, A. A.; Gurevitch, I.; Mullin, S. A.; Wanakule, N. S.; Balsara, N. P. *Macromolecules* **2013**, *46*, 914–921.
- [9] Bouchet, R.; Phan, T. N. T.; Beaudoin, E.; Devaux, D.; Davidson, P.; Bertin, D.; Denoyel, R. *Macromolecules* **2014**, *47*, 2659–2665.
- [10] Sethuraman, V.; Mogurampelly, S.; Ganesan, V. *Macromolecules* **2017**, *50*, 4542–4554.
- [11] Young, W. S.; Epps, T. H. *Macromolecules* **2012**, *45*, 4689–4697.
- [12] Sethuraman, V.; Mogurampelly, S.; Ganesan, V. *Soft Matter* **2017**, *13*, 7793–7803.
- [13] Mogurampelly, S.; Borodin, O.; Ganesan, V. *Annual Review of Chemical and Biomolecular Engineering* **2016**, *7*, 349–371.
- [14] Van Gunsteren, W. F. et al. *Angewandte Chemie - International Edition* **2006**, *45*, 4064–4092.
- [15] McQuarrie, D. *Sausalito, Calif.: University Science Books* **2004**, *12*, 641.
- [16] Frenkel, D.; Smit, B. *New York: Academic*
- [17] Janke, W. *Quantum* **2002**, *10*, 423–445.
- [18] Shirts, M. R.; Chodera, J. D. *Journal of Chemical Physics* **2008**, *129*.

- [19] Chodera, J. D.; Swope, W. C.; Pitera, J. W.; Seok, C.; Dill, K. A. *Journal of Chemical Theory and Computation* **2007**, *3*, 26–41.
- [20] Hess, B. *Journal of Chemical Physics* **2002**, *116*, 209–217.
- [21] Klimovich, P. V.; Shirts, M. R.; Mobley, D. L. *Journal of Computer-Aided Molecular Design* **2015**, *29*, 397–411.
- [22] Marrink, S. J.; Risselada, H. J.; Yefimov, S.; Tieleman, D. P.; De Vries, A. H. *Journal of Physical Chemistry B* **2007**, *111*, 7812–7824.
- [23] Ingólfsson, H. I.; Melo, M. N.; Van Eerden, F. J.; Arnarez, C.; Lopez, C. A.; Wasseenaar, T. A.; Periole, X.; De Vries, A. H.; Tieleman, D. P.; Marrink, S. J. *Journal of the American Chemical Society* **2014**, *136*, 14554–14559.
- [24] Uusitalo, J. J.; Ingólfsson, H. I.; Akhshi, P.; Tieleman, D. P.; Siewert, J. **2015**,
- [25] Monticelli, L.; Kandasamy, S. K.; Periole, X.; Larson, R. G.; Tieleman, D. P.; Marrink, S.-J. *Journal of chemical theory and computation* **2008**, *4*, 819–834.
- [26] Panizon, E.; Bochicchio, D.; Monticelli, L.; Rossi, G. *Journal of Physical Chemistry B* **2015**, *119*, 8209–8216.
- [27] Rossi, G.; Monticelli, L.; Puisto, S. R.; Vattulainen, I.; Ala-Nissila, T. *Soft Matter* **2011**, *7*, 698–708.
- [28] Nawaz, S.; Carbone, P. *Journal of Physical Chemistry B* **2014**, *118*, 1648–1659.
- [29] Vögele, M.; Holm, C.; Smiatek, J. *Journal of Chemical Physics* **2015**, *143*.
- [30] Sun, X. L.; Pei, S.; Wang, J. F.; Wang, P.; Liu, Z. B.; Zhang, J. *Journal of Polymer Science, Part B: Polymer Physics* **2017**, *55*, 1220–1226.
- [31] Rossi, G.; Giannakopoulos, I.; Monticelli, L.; Rostedt, N. K. J.; Puisto, S. R.; Lowe, C.; Taylor, A. C.; Vattulainen, I.; Ala-Nissila, T. *Macromolecules* **2011**, *44*, 6198–6208.
- [32] Lo, C. A. et al. *Journal of Chemical Theory and Computation* **2009**, *5*, 3195–3210.
- [33] Alessandri, R.; Uusitalo, J. J.; De Vries, A. H.; Havenith, R. W.; Marrink, S. J. *Journal of the American Chemical Society* **2017**, *139*, 3697–3705.
- [34] Xu, H.; Matysiak, S. *Chem. Commun.* **2017**, *53*, 7373–7376.
- [35] Rossi, G.; Fuchs, P. F.; Barnoud, J.; Monticelli, L. *Journal of Physical Chemistry B* **2012**, *116*, 14353–14362.
- [36] Rossi, G.; Elliott, I. G.; Ala-Nissila, T.; Faller, R. *Macromolecules* **2012**, *45*, 563–571.
- [37] Webb, M. A.; Savoie, B. M.; Wang, Z.-G.; Miller III, T. F. *Macromolecules* **2015**, *48*, 7346–7358.
- [38] Lee, H. *The Journal of Physical Chemistry C* **2012**, *116*, 9327–9333.
- [39] Lee, H.; Larson, R. G. *Biomacromolecules* **2016**, *17*, 1757–1765.
- [40] Dong, J.; Zhou, J. *Macromolecular Theory and Simulations* **2013**, *22*, 174–186.

## Chapter 2

# A transferable MARTINI model of polyethylene oxide

“ *The most exciting phrase to hear in science, the one that heralds new discoveries, is not "Eureka" but "That's funny..."*. ”

”

---

Isaac Asimov,

This chapter is based upon the manuscript: A transferable MARTINI model of polyethylene oxide, by F. Grunewald, G. Rossi, A. H. de Vries, S. J. Marrink and L. Monticelli, J. Phys. Chem. B. 2018 - accepted

## Summary

Motivated by the deficiencies of the previous MARTINI models of polyethylene oxide (PEO), we present a new model featuring a high degree of transferability. The model is parameterized on (a) a set of 8 free energies of transfer of dimethoxyethane (PEO dimer) from water to solvents of varying polarity; (b) the radius of gyration in water at high dilution; and (c) matching angle and dihedral distributions from atomistic simulations. We demonstrate that our model behaves well in five different areas of application: (1) it produces accurate densities and phase-behavior of small PEO oligomers and water mixtures; (2) it yields chain dimensions in good agreement with experiment in three different solvents (Water, Diglyme and Benzene) over a broad range of molecular weights ( 1.2 kg/mol to 21 kg/mol); (3) it reproduces qualitatively the structural features of lipid bilayers containing PEGylated lipids in the brush and mushroom regime; (4) it is able to reproduce the phase-behavior of several PEO-based non-ionic surfactants in water; (5) it can be combined with the existing MARTINI PS to model PS-PEO block-copolymers. Overall, the new PEO model outperforms previous models and features a high degree of transferability.

## Introduction

Polyethylene glycol (PEG), also known as polyethylene oxide (PEO), is one of the few polymers with an exceptionally wide scope of applications ranging from bio-medical applications, over cosmetics and food additives to the active material in polymer batteries. Many applications of PEO involve multiple chemical components and supra-molecular assemblies in non-crystalline phases, for which structural information is typically only available at low resolution (if at all). Molecular dynamics (MD) simulations are a powerful method to gain an insight into the structure and dynamics of liquids and soft matter, including biological macromolecules and polymers. Depending on the time and length scales relevant for the specific system at hand, either atomistic or coarse-grained (CG) molecular dynamics simulations can be used to characterize and even predict the properties of materials. One of the most commonly used CG models for biomolecular simulations is the MARTINI model. MARTINI is based on a building block approach, i.e., each building block represents a chemical moiety and is parameterized separately; larger molecules are obtained by stitching together multiple building blocks. MARTINI represents a group of about 4 heavy atoms as

one particle (bead). Each bead has a specific type, which is defined by a set of Lennard-Jones potentials for the interaction with the other beads in the force-field. Electrostatic interactions are calculated for particles holding a full charge. The choice of the bead type for a given group of atoms is based on matching the free energies of transfer of the chemical moiety with experimental data.<sup>1</sup>

MARTINI has been used successfully to model a range of polymers,<sup>2 3 4 5 6 7</sup> and several MARTINI models have been published also for PEO.<sup>8 9 10 11 12</sup>. Yet, it was realized already in the first published parametrization that none of the standard MARTINI beads is appropriate for modeling a PEO type repeat unit because some structural and thermodynamic properties could not be matched accurately enough.<sup>13</sup> As similar observations were made for other models, new beads with custom made interactions were introduced on several occasions.<sup>8 9 12</sup> Usually the authors intended to approach a specific problem, so the new PEO beads were optimized to reproduce some specific property of the system of interest. Some of these initial PEO parametrizations have since been refined in multiple steps to extend their scope. From here onwards, we shall define a model as a parametrization of PEO, including a new bead type, for which an interaction matrix with all other MARTINI beads is provided. The first model of PEO was put forward by Lee et al.,<sup>13</sup> shortly followed by the model of Rossi and coworkers.<sup>9</sup> The Lee model started from one of the standard MARTINI beads (SNa), but the authors found: the radius of gyration and end-to-end distance in water can only be reproduced by using the SNda bead type. On the other hand, they anticipated that the rest of the interactions were more appropriately represented by the SNa type. Thus it was proposed to take the self-interaction and the interaction with water from the SNda type. All the other interactions were modeled using the SNa type, effectively creating a new bead.<sup>13</sup> In a later study based on PEGylated lipids, the SNa was then changed to SN0 to reduce the excessive adsorption of PEO tails onto lipid head groups.<sup>8</sup> The last refinement on the model was completed in 2013 with the introduction of new bonded parameters, which reduced the instability the model suffered from due to its dihedral potentials in the backbone of the polymer.<sup>10</sup> In contrast, the Rossi model was aimed at reproducing the experimental free energy of transfer of dimethoxyethane (PEO dimer) from water to octanol. Since none of the standard beads was able to yield a sufficiently accurate free energy of transfer, the authors decided to create a new bead. The self-interaction was subsequently determined from the long-range structural properties. Since the new bead was an intermediate to the standard Nda and P1, the rest of the interaction table was provided

based on similarity. As the Rossi model had no dihedral potential, its numerical stability was superior to the Lee model.<sup>9</sup> While both models proved successful in their special cases and have been reused in similar environments, transferability to different chemical environments remained problematic. In particular, the interaction with hydrophobic phases was much too unfavorable for both models. First Huston and Larson<sup>14</sup> pointed out that the behavior of PEO at hydrophobic interfaces is incorrect for both models. Later Carbone et al. noticed that the Rossi model displays too collapsed conformations in hydrophobic solvents.<sup>7</sup> It was already realized earlier that the water-hexadecane free energy of transfer was far off for both models compared to an estimate based on experimental data.<sup>15</sup> Later, free energies of transfer obtained from atomistic simulations confirmed that both PEO models were too hydrophilic by a large amount.<sup>12</sup> The excessive hydrophilic character made both models problematic to use in non-polar environments, which are relevant in the field of materials science – for example, lithium ion batteries, where polystyrene (PS)-PEO copolymers are self-assembled in apolar solvents.<sup>16 17 18</sup> Here we present a new model for PEO, characterized by a high transferability between different environments, especially extending the domain of usage to non-polar solutions. The new model is based on reproducing free energies of transfer of dimethoxyethane, obtained either from experiment or from atomistic simulations, and it is applicable over a wide range of molecular weights, spanning three orders of magnitude. We show that the new model reproduces essential features of previous models and improves on their results; models of PEGylated lipids show reasonable performance, and excellent agreement with experimental data is obtained for the phase-behavior of nonionic surfactants. In addition, we show that the new model can be combined with the current MARTINI polystyrene (PS) model to give one of the technologically most relevant block-copolymers, PS-*b*-PEO.

## Methods

As in previously published polymer models<sup>2 5 9 19</sup> the parametrization of the new PEO model is based on (A) free energies of transfer of dimethoxyethane between a range of solvents, and (B) long range structural properties of isolated polymer chains – namely the radius of gyration of a long polymer chain (477 residues) in water, calculated at high dilution. Target values for the free energies of transfer and the radii of gyration are taken from experiments whenever available; when unavailable, target values are cal-

culated from atomistic simulations. Below we describe first the setup and parameters for free energy calculations and simulations of individual chains in solution; then we report the methods used for validation of the new model (radius of gyration in different solvents, the phase-behavior of PEO oligomers, PEGylated lipids, non-ionic surfactants, and PS-PEO micelles).

## Free Energy Calculations

Free energies of transfer of dimethoxyethane were calculated at the atomistic and coarse-grained level as differences between free energies of solvation in different solvents. Solvation free energies were computed by alchemical free energy transformations as implemented in the GROMACS package.<sup>20</sup> The free energy of the transformation was estimated using the Multi-state-Bennetts-Acceptance-Ratio (MBAR) method<sup>21</sup>, obtained using a python tool available on github (<https://github.com/davidlmobley/alchemical-analysis>). For each calculation, the convergence and quality of the calculations were checked following the guidelines suggested by Klimovich, Shirts and Mobley.<sup>22</sup> The error reported with the calculations is the statistical error estimate. For both sets of simulations, the intra-molecular interactions were not switched off.

## Atomistic calculations

All atomistic simulations were run using the GROMOS 2016H66 force-field. This force-field has been validated against bulk properties of many solvents<sup>23</sup> and has ether oxygen parameters, which have been shown to reproduce correct solvation free energies for dimethoxyethane<sup>24</sup>, as well as a correct phase-behavior for non-ionic surfactants<sup>25</sup>, of interest for the present work. Lennard-Jones (LJ) and Coulomb interactions were cut-off at 1.4 nm, which is the standard GROMOS cut-off. Long-range Coulomb interactions were treated by the reaction field approach, with the relative dielectric constant set to the value of the bulk solvent (also following the GROMOS standard treatment). All bond lengths were constrained, as in the original work.<sup>23</sup> Our simulation conditions differ from the standard GROMOS conditions in two respects: (1) we ran all simulations with the GROMACS software, which implements a highly efficient Verlet cut-off scheme (Verlet buffer tolerance of  $10^{-6} \text{ kJ} \times \text{mol}^{-1} \times \text{ps}^{-1}$  per particle) for the non-bonded interactions instead of the standard GROMOS twin-range cut-off (used in the GROMOS parametrization and unavailable in GROMACS); (2) LJ and Coulomb modifiers were used to shift the potential

to zero at the cut-off, to avoid discontinuities in the potential and improve energy conservation. To verify that our settings reproduce GROMOS results and yield acceptable solvent properties, we calculated the density and heat of vaporization of each bulk solvent (see Appendix B). Our results compare very favorably with the values from the original publication and experiment, with deviations in the heat of vaporization below  $1.9 \text{ kJ} \times \text{mol}^{-1}$  in both cases. Two different sets of simulation parameters were employed for the simulations of polar and apolar bulk solvents. In the case of propanethiol, butanol, acetone and propanol the lambda vector for switching off the interactions was split into its Coulomb and Lennard-Jones components; first, we switched off the Coulomb interactions between solvent and solute, then the LJ interactions. For the simulations in Cyclohexane, Octane and Benzene, which are less polar, only one lambda vector was used. In order to improve convergence, in both sets of simulations soft-core potentials were employed, using the parameters detailed by Shirts and coworkers.<sup>26</sup> Each window was run for either 16 ns or 20 ns, and a variable amount of equilibration time was discarded based on convergence analysis (following Klimovich and coworkers<sup>22</sup>). The derivative of the potential energy with respect to lambda was computed every 50 steps. All simulations were performed using the stochastic dynamics (SD) integrator<sup>27</sup> implemented in GROMACS (version 2016.4), with a time step of 2 fs. Production runs were performed in the NpT ensemble at 298.15 K (with inverse friction constant of 2 ps), using the Parrinello-Rahman barostat<sup>28</sup> to fix the pressure at 1 bar (time constant of 2 ps and compressibility set to the experimental value or the value used in the original simulations<sup>23</sup>).

### Coarse-grained calculations

For the coarse-grained (CG) simulations, the MARTINI force-field version 2.2 was used as available online (<http://mmsb.cnrs.fr/en/team/mobi> or <http://cgmartini.nl>). The run settings were the same as suggested by de Jong et al.<sup>29</sup> (cut-off for non-bonded interactions: 1.1 nm; Verlet neighborlist scheme) with the exception of the verlet-buffer-tolerance, which was decreased from the GROMACS default value to  $10^{-6} \text{ kJ} \times \text{mol}^{-1} \times \text{ps}^{-1}$  per particle. Since none of the MARTINI models in the system of interest have partial charges, only one lambda vector of 15 non-uniformly spaced points was used to switch off the LJ component of the potential energy. All 15 windows were run for 16 ns and the derivative with respect to lambda was computed every 10 steps. All CG simulations were carried out with the GROMACS software (version 2016.4)<sup>20</sup>, using

the stochastic dynamics integrator<sup>27</sup> (with inverse friction constant 1.0 ps) and a time step of 20 fs. Production runs were carried out in the NpT ensemble at 298.15 K and 1 bar using the Parinello-Rahman barostat<sup>28</sup> (time constant 4.0 ps and compressibility  $4.510^{-5} \text{bar}^{-1}$ ).

## CG simulations of PEO systems

We used our newly developed PEO model for all simulations of PEO systems. All topology files and starting structures were generated using the python tool Polyply, which can generate starting structures and topology files (compatible with the GROMACS software) for both atomistic and coarse-grained polymer chains. The tool will be described in detail in a separate publication (manuscript in preparation), and a preliminary version including instructions can be found on GitHub ([https://github.com/fgrunewald/Martini\\_PolyPly](https://github.com/fgrunewald/Martini_PolyPly)).

### Single Chain in Solution

The radius of gyration and end-to-end distance of PEO in three different solvents (water, Benzene and Diglyme) was obtained by simulating a single chain in a box of solvent. For the first two solvents, the temperature was fixed at 298.15 K using the velocity rescale thermostat introduced by Bussi and coworkers.<sup>30</sup> In contrast the simulation in Diglyme was performed at 323.5 K, which is the experimental theta temperature of this solvent.<sup>31</sup> For all simulations, the pressure was fixed at 1 bar using the Parrinello-Rahman barostat<sup>28</sup> (time constant of 10 ps and compressibility of  $4.510^{-5} \text{bar}^{-1}$ ). For each solvent, 5 different molecular weights were considered, from about  $1.2 \text{kg} \times \text{mol}^{-1}$  to  $11 \text{kg} \times \text{mol}^{-1}$ ; in the case of water, one additional simulation with a molecular weight of  $21 \text{kg} \times \text{mol}^{-1}$  (corresponding to 477 monomers) was performed. All simulations in Water and Diglyme were run for at least  $30 \mu\text{s}$ , while the simulations in Benzene were run for at least  $20 \mu\text{s}$ . For all systems of PEO the standard GROMACS MD integrator with a time step of 20 fs was used.

To avoid artifacts from periodic boundary conditions and interactions between periodic images, all simulations were conducted in the dilute regime, at concentrations below the approximate overlap concentration. The overlap concentration is given by:<sup>32</sup>

$$\phi^* \approx \frac{N \times b^3}{\langle R \rangle^3} \approx \frac{1}{N^v} \quad (2.1)$$

In this case  $N$  is the number of repeat units, with length  $b$ , of an equivalently jointed chain.  $\langle R \rangle$  is the end-to-end distance. The exponent  $\nu$  is approximately 0.5 for theta solvents and 3/5 for good solvents.  $N$  can be approximated from the characteristic ratio, as explained in Appendix E.

### Solutions of PEO oligomers

Solutions of PEO oligomers in water were simulated at 298.15 K and 1 bar pressure, using the same run parameters as for the simulation of single chains in solution. For the four oligomers Dimethoxyethane (DXE), Diglyme (DEG), Triglyme (TIG) and Tetraglyme (TRG) the density was computed from simulations of 200 ns (after equilibration for 12 ns with Berendsen pressure coupling<sup>33</sup>).

### PEGylated lipids

Two bilayer systems containing mainly DPPC and smaller amounts of DOPE as well as PEGylated DOPE (PEL) (see 2.1) were simulated at 283 K. The concentration of PEL in bilayers A and B corresponds to the diluted (mushroom) and crowded (brush) regime, respectively. Each system was prepared by first generating a smaller bilayer patch using the python tool `insane.py`,<sup>34</sup> and contained 1 DOPE lipid in each leaflet and the appropriate number of DPPC lipids to reach the desired concentration. Subsequently, PolyPly was used to grow a 45-repeat unit PEO chain onto one of the DOPE lipids. PEO chains were terminated by one SP2 bead (to represent the terminal hydroxyl group). Details on mapping and bonded interactions are provided in the next section. Afterwards the system was stacked in the xy-plane to obtain the final bilayer. Note that only one leaflet contained the PEGylated lipids. This choice was made to ensure the PEO tail does not interact with its periodic image. The equilibrium box dimensions were 21.72 nm by 21.72 nm by 37.60 nm for system A and 18.57 nm by 18.57 nm and 50.01 nm for system B, respectively. Note the higher amount of water (normal W and anti-freeze WF beads) in system B due to the expectation of a more stretched chain. The simulations were run for about 4  $\mu$ s. The run parameters were the same as those used for the radius of gyration simulation, with the exception of the pressure coupling scheme (semi-isotropic instead of isotropic).

Table 2.1: Composition of bilayers with PEGylated lipids

Molecule	#in bilayer A	# in bilayer B
DPPC	2016	864
DOPE	16	144
PEL/Na+	16	144
W	125,984	127,872
WF	1600	1440

### Nonionic Surfactants

The self-assembly of 3 types of nonionic surfactants (C12E6, C12E4, C12E2) mixed with water at three different concentrations (50w%, 53w%, and 71.15 w%) were simulated. The run parameters were the same as those used for measuring the radius of gyration. However, the pressure coupling in this case was done using a semi-isotropic Berendsen barostat<sup>33</sup> with both the z and xy component of the pressure fixed to 1 bar using a coupling time of 2ps and a compressibility of  $4.5 \cdot 10^{-5} \text{bar}^{-1}$ . The surfactants and water molecules were coupled separately to the thermostat using a coupling time constant of 4 ps and a reference temperature of 298.15 K. Each system was run 6 times, each time with a different 6 digit long random-seed for generating random velocities from the same initial structure. Each simulation was run for  $5 \mu\text{s}$ , to ensure the observed structures were stable in time.

### PS-PEO Micelles

A system containing 370 and 740 oligomers of the block-copolymer PS-PEO with lengths of 10 and 23 repeat units, respectively, was simulated at 298.15 K and 1 bar pressure. The simulation parameters were the same as used for the radius of gyration simulations except for the pressure coupling (Berendsen instead of Parrinello-Rahman barostat). The initial structure of PS-PEO was generated using PolyPly. A single chain was equilibrated in water, then the systems of interest were generated by inserting 370 or 740 copies of the polymer chain at random positions with random rotation into a box, and solvating with water (182,942 and 388,630 MARTINI water particles, respectively). The dimensions of the final box sizes were  $28.4 \times 28.40 \times 28.4$  and  $36.4 \times 36.4 \times 36.4 \text{nm}^3$ , respectively. The simulations were run for  $3.4 \mu\text{s}$ . The dimension and aggregation number were determined using a homemade python script, which utilizes the

scikit-learn<sup>35,36</sup> library implementation of DBSCAN<sup>37</sup> to cluster beads of PS-b-PEO into aggregates based on the number density. Reading and processing of topology and trajectory information is done with MDAnalysis.<sup>38,39</sup> Details on the procedure for computing the radius of gyration and aggregation number are outlined in the Appendix F. The script is available online free of charge ([https://github.com/fgrunewald/tools\\_for\\_MD\\_analysis](https://github.com/fgrunewald/tools_for_MD_analysis)).

### Assessment of convergence and error estimation

Assessment of convergence and error estimation is crucial when determining any property of polymer chains (e.g., radius of gyration, end-to-end distance, etc.). To ensure reproducibility, a three-step protocol was used to assess convergence: (1) average properties were plotted as a function of the fraction of total simulation time; (2) the same was done for the autocorrelation time (estimated with a procedure proposed by Chodera and coworkers<sup>21,40</sup>); (3) the autocorrelation time was also estimated using the block averaging approach described by Hess.<sup>41</sup> The error was estimated from the uncorrelated data set after subsampling the original data using the pymbar package (<https://www.github.com/choderalab/pymbar>). All analyses were carried out with a python tool provided online on GitHub ([https://github.com/fgrunewald/tools\\_for\\_MD\\_analysis](https://github.com/fgrunewald/tools_for_MD_analysis)); details on its usage and on the analysis of convergence and error estimation are reported in Appendix C.

## Results and Discussion

### Parametrization of PEO and associated compounds

In this section, we present the parameters for the new PEO model as well as for related compounds: nonionic surfactants, polystyrene (PS)-PEO block copolymers, and PEGylated lipids.

#### Mapping Schemes

Representation of PEO and PEO-containing compounds. The fragment of a chemical structure represented by a bead is indicated by a gray circle with the corresponding bead type displayed within the bead. The mapping procedure consists in selecting groups of atoms and representing them by one interaction center (bead). In MARTINI, the number of atoms per

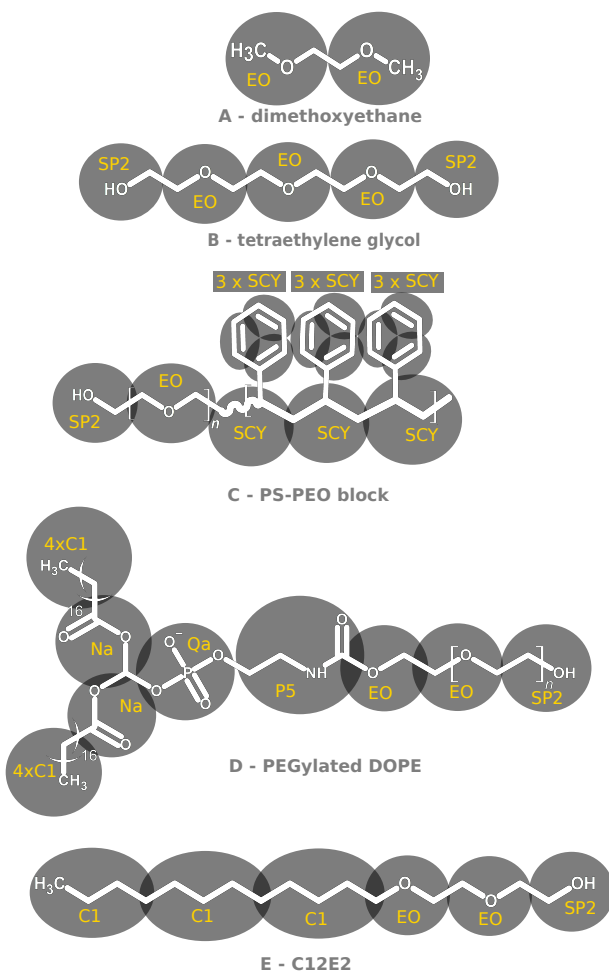


Figure 2.1: Representation of PEO and PEO-containing compounds. The fragment of a chemical structure represented by a bead is indicated by a gray circle with the corresponding bead type displayed within the bead

bead usually varies between three and five and there are no strict mapping rules. Hence there can be several equally valid mappings for the same molecule. After the mapping scheme has been defined, the interactions between the different beads are chosen from an interaction matrix based on reproducing the free energy of transfer of the individual beads (or related compounds). The previous models of PEO have essentially used the same mapping scheme, with differences in the way end-groups were treated. In this mapping scheme, a PEO repeat unit consists of the sequence  $-\text{CH}_2 - \text{O} - \text{CH}_2\text{-}$  as opposed to the definition of a repeat unit in polymer chemistry textbooks, which usually is  $-\text{O} - \text{CH}_2 - \text{CH}_2\text{-}$ .<sup>32,42</sup> There are two distinct advantages of using the first representation: first, there is a more chemically intuitive connection between the small-molecules dimethylether (DME) and dimethoxyethane (DXE, Figure 2.1), representative of the monomer and dimer of the repeat unit. Second, the same mapping scheme has been used before, therefore, one can hope to retain much of the previous parametrization in terms of bonded interactions. However, a disadvantage arises with respect to (1) the way the length of the polymer chain is defined, and (2) the way end groups are treated. The first mapping scheme is not fully commensurate with the underlying atomistic structure.

For instance, compound B in Figure 2.1 (tetraethylene glycol) is a PEO tetramer; using the first mapping scheme, we can define three repeat units; this, however, suppresses two terminal  $\text{CH}_2\text{OH}$  groups. Lee et al.<sup>13</sup> suggested to neglect such detail, and simply add an additional bead of the same type, so that an  $n$ -mer of PEO consists of  $n$  beads of the same type. While this choice is intuitive and a good enough approximation for long chains, it reduces the polarity of shorter chains (hydroxyl groups are significantly more polar than ether groups). To take into account the higher polarity of OH-terminated chains, it is possible to add one SP2 bead at the chain end. While mapping two heavy atoms into one bead is unusual for MARTINI, it has previously been shown that including a more polar end-group is crucial for obtaining the correct phase-behavior of nonionic surfactants.<sup>9</sup> Furthermore, this choice improves the properties of small oligomers. Thus, we will represent the tetramer of PEO by five beads: three of one type, which we call EO, and two of the polar SP2 type. In general, for OH terminated chains, we will use  $n-1$  PEO beads and two SP2 beads. In contrast, for methyl-terminated chains (such as DXE in Figure 2.1A), only EO beads are used. For cases where another end group or possibly another polymer is attached to one end of the chain, as is the case for nonionic surfactants (Figure 2.1E), or a PS-PEO block-copolymer (Figure 2.1C), the PEO part

of length  $n$  will contain  $n$  beads of type EO plus one SP2 end-group and the rest of the molecule. For example, the surfactant C12E2, shown in figure 2.1E, contains 12 carbon atoms and two PEO repeat units, which are OH terminated. Thus, we will represent this molecule by three normal beads of type C1, two EO beads and the SP2 end group. The same reasoning can be applied to PS-PEO block copolymers (Figure 2.1C). We notice that, if the linking unit contains more polar atoms, a different approach might be needed.

### Non-bonded interactions for the EO type bead

The MARTINI force-field uses Lennard-Jones (LJ) potentials to model non-bonded interactions. In the current version of MARTINI (v2.2), the LJ  $\epsilon$  parameter (related to the minimum of the potential) can assume 10 different values, whereas  $\sigma$  (related to the size of the particle) can only take two values: 0.47 nm (used for standard beads, representing about 4 heavy atoms on a linear chain); and 0.43 nm (used for ring and small beads, representing less than 4 heavy atoms). The interaction between standard and small beads has a  $\sigma$  value of 0.47 nm. Since EO beads represent three non-hydrogen atoms, they should be considered as small beads ( $\sigma = 0.43$ ); this leaves the values of  $\epsilon$  as the parameter to be adjusted to reproduce the free energies of transfer.

As detailed in the introduction, the repeat unit of PEO is poorly represented by any standard MARTINI particle type. Moreover, PEO models using non-standard particle types (e.g., the Lee model and the Rossi model) are too hydrophilic.<sup>12 14 15</sup> In such models, the free energy of hydration of dimethoxyethane (DXE) is equal to or lower than the experimental value (-20.2 kJ/mol<sup>9</sup>). In contrast, the free energy of hydration for all standard MARTINI beads is higher (more positive) than observed in experiment. For these models, as a consequence, to match partitioning of DXE between water and octanol, the interactions of the non-standard PEO beads with hydrophobic particles needed to be less attractive. This caused a shift of the interaction matrix with respect to the other MARTINI beads, artificially enhancing the hydrophilicity.

The new model developed here is also based on matching the free energies of transfer for DXE between different solvents. Only one experimental value for water-solvent partitioning is reported in the literature – the one for water-octanol. Therefore, in this work, we used free energies of transfer calculated from atomistic simulations as a reference for our parametrization. The solvents we chose span the entire MARTINI interaction matrix,

from very hydrophilic to very hydrophobic. In this way, one can make sure not to fall victim to the same trap as the previous models did. The reference atomistic force-field used was a special variant of GROMOS named 2016H66, which has been optimized with respect to ether properties and includes a sufficiently large number of well parametrized solvents.<sup>23</sup>

The individual solvation free energies are shown in Appendix B.

The free energies of transfer for DXE are reported in Table 2. Here we make a few remarks. First, DXE prefers water over hydrocarbons. However, Benzene is a special case: the free energy of transfer from water is about 0, meaning that DXE does not have a preference between Benzene and Water. While this seems quite counterintuitive at first, it is well documented that Benzene is a good solvent for PEO.<sup>43</sup> DXE has a preference for acetone and propanethiol over water, while it prefers water over short chain alcohols. Comparison of the reference free energies with the results obtained for the Lee and Rossi models shows that, in most cases, partitioning was not reproduced very well, with the exception of water-octanol. In this case, the underestimation of the interaction with the alkane chain is compensated by the overestimation of the interaction with the more hydrophilic components. Since free energies of transfer are just differences between free energies of solvation, an absolute reference is also needed in order to define all interactions. One possibility is to choose the free energy of hydration as an absolute reference, as suggested by Carbone and coworkers.<sup>12</sup> However, in MARTINI, free energies of hydration are generally higher (less negative) than the experimental ones. Matching experimental values would be very simple, and would imply setting stronger interactions (higher values of the Lennard-Jones  $\epsilon$ ) all across the MARTINI table. The consequence of such choice would be that liquids with strong inter-molecular interactions (e.g., alcohols, glycols, polar ones) would become solid at room temperature. Considering all this, it is clear that matching free energies of hydration should be avoided (a) to maintain consistency with the rest of the MARTINI model without a complete reparametrization of the force-field, and also (b) to avoid freezing of all polar liquids at room temperature. We set a value of 3.5 kJ/mol for the interaction of PEO with water (the same value as for N0), resulting in a hydration free energy of  $-14.73 \pm 0.05$  kJ/mol, which is 5.5 kJ/mol higher than the experimental value. With this choice for the water interaction, the other  $\epsilon$ -values of the new EO bead were obtained by iteratively computing the free energies of transfer between water and selected solvents, and adjusting the epsilon value to yield the best possible agreement with the reference values. The interactions with C1, SC1, C5, SC5, Na and P1 were parametrized by matching the free energies

Table 2.2: Free energies of transfer of dimethoxyethane (DXE) from different solvents to water. The values reported for the Lee model and the Rossi model were calculated in the present work, using the published models. Reference values are taken from experiments or from atomistic calculations. The last two solvents were used for validation, whereas the rest were used as target.

Solvent	Bead Type	Reference	Lee et al.	Rossi et al.	this work
Octane	C1	$-7.3 \pm 0.3^*$	$-13.96 \pm 0.06$	$-18.86 \pm 0.06$	$-7.75 \pm 0.06$
Cyclohexane	SC1	$-6.8 \pm 0.3^*$	$-24.87 \pm 0.07$	$-29.64 \pm 0.07$	$-8.66 \pm 0.07$
Benzene	SC5	$0.2 \pm 0.3^*$	$-9.72 \pm 0.08$	$-14.94 \pm 0.08$	$0.24 \pm 0.08$
Propanethiol	C5	$2.2 \pm 0.3^*$	$1.79 \pm 0.06$	$-3.28 \pm 0.06$	$2.03 \pm 0.06$
Acetone	Na	$1.2 \pm 0.3^*$	$-1.53 \pm 0.06$	$12.09 \pm 0.07$	$1.04 \pm 0.06$
Propanol	P1	$-1.5 \pm 0.3^*$	$-3.92 \pm 0.07$	$8.70 \pm 0.07$	$-3.15 \pm 0.07$
Butanol	Nda	$-2.2 \pm 0.3^*$	$-5.39 \pm 0.07$	$8.91 \pm 0.07$	$-3.05 \pm 0.07$
Octanol	P1-C1	$-1.2^\dagger$	$-0.15 \pm 0.07$	$0.18 \pm 0.07$	$-1.11 \pm 0.06$

\* from atomistic simulations

† from experiment

Table 2.3: Interaction matrix of the new PEO bead.

Bead	$\epsilon$ ( $\text{kJ} \times \text{mol}^{-1}$ )	Bead	$\epsilon$ ( $\text{kJ} \times \text{mol}^{-1}$ )
Qda*	3.5	Nda*	3.1
Qd*	3.5	Nd*	3.1
Qa*	3.5	Na*	3.1
QO*	3.5	N0*	3.1
P5*	3.5	C5‡	2.95
P4*	3.5	C4*	2.95
P3*	3.5	C3*	2.95
EO†	3.4	C2*	2.70
P2*	3.1	C1‡	2.53
P1*	3.1		

of transfer from water to octane, cyclohexane, propanethiol, acetone and ethanol, respectively. \* for small beads  $\epsilon = \epsilon \times 0.75$  † only as small bead with  $\epsilon = \epsilon \times 0.75$  ‡ for small beads  $\epsilon = \epsilon \times 0.90$

The rest of the interaction table (Table 3) was filled in by interpolation, using the same interaction for similar bead types. This approach was validated by verifying the free energies of transfer from water to octanol and butanol; these were not used as targets in the parametrization, and yet the agreement with the reference values is very good. The s-versions of each bead are obtained by scaling the  $\epsilon$ -value of the normal bead by 0.75, except for the case of Benzene and Cyclohexane, for which a scaling factor of about 0.9 was required to obtain good partitioning free energies. Overall the free energies of transfer improve greatly from our model to the previous models, especially in the case of Benzene and Octane. The self-interaction of the PEO bead was fit to reproduce the experimental radius of gyration of a single chain in water. To obtain a most reliable result, we chose a chain length of 477 repeat units (corresponding to a molecular weight of about 21 kg/mol), because scattering data is available for this chain length.<sup>44</sup> Moreover, at such long chain length, the effect of the end-groups is negligible. Since the radius of gyration also depends on the bonded interactions, the self-interaction was optimized by trial-and-error in several cycles alongside the bonded interactions. In the final iteration, the value of the self-interaction was set to 3.4 kJ/mol. This yields a radius of gyration of  $6.6 \pm 0.2$  nm, in excellent agreement with the experimentally determined value of 6.5 nm.<sup>44</sup>

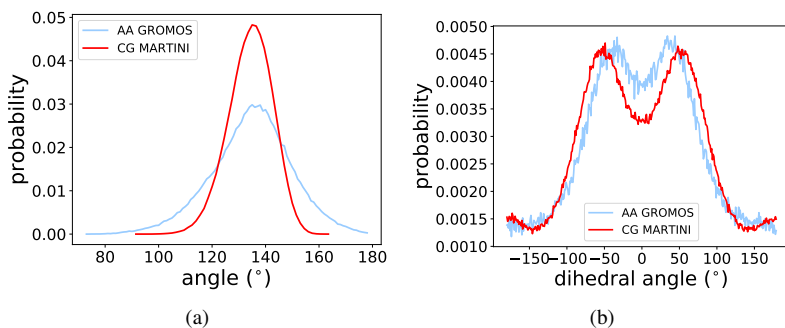


Figure 2.2: Comparisons of angle (a) and dihedral (b) distributions of PEO from atomistic and coarse-grained simulations

### Bonded Interactions for PEO

For the bond between two PEO beads, a simple harmonic potential was used with a reference length set to 0.322 nm and a force-constant of 7000 kJ/mol, following the original values from the Rossi model.<sup>9</sup> As described by Rossi et al. and verified here, this bond length results in better properties for the nonionic surfactants compared to the bond length of 0.33 nm used in the Lee model.

The angle and torsion potentials were optimized to reproduce the atomistic distributions of GROMOS 53A6oxy<sup>24</sup> PEO in water. The target distributions were taken from the paper of Rossi and coworkers.<sup>9</sup> Moreover, we aimed at having high numerical stability, even for long chains, with an integration time-step of 20 fs. It has been noticed previously that MARTINI models employing a dihedral potential along the backbone may have stability problems when one of the angles approaches the value of 180 degrees. To solve this stability issue, we used the “restricted bending” potential developed by Bulacu and coworkers.<sup>10</sup> Figure 2.2 shows the distributions of the angle and dihedral for the atomistic and the CG representation. The CG distribution for the dihedral angle matches fairly well the atomistic reference, thus no optimization was performed. The angle distribution for the CG model has the same average as the atomistic target, but the width is reduced. This choice was required to ensure numerical stability with a time-step of 20 fs, as verified in runs with 370 PEO chains of length 20 over 900 ns (totaling over 7000 dihedral potentials, much larger than the system used in previous tests). The parameters chosen here represent

a reasonable compromise between accuracy (with respect to reproducing atomistic distributions) and numerical stability.

## Validation of the new model

In order to demonstrate the transferability of the model and assess the range of molecular weights over which it can be applied, we performed a number of tests on PEO and PEO-containing compounds, considering five different application areas.

### PEO oligomer phase-behavior and density

Table 2.4: Densities for mixtures of Triglyme (TIG) and Water at 303.15 K as well as pure solutions of Dimethoxyethane (DXE), Diglyme (DGL) and Tetraglyme (TRG) at 298.15.

Compound	mol% PEO	exp.	Lee model	present work
DXE	100	868.0*	937.0*	$878.7 \pm 0.4$
DGL	100	945.0*	1002.0*	$965.6 \pm 0.3$
TRG	100	1040.0*	1067.0*	$1037.7 \pm 0.3$
TIG	100	975.86*	$1040.0 \pm 0.3$	$1007.3 \pm 0.3$
TIG	80	979.80†	$1033.2 \pm 0.3$	$1000.2 \pm 0.4$
TIG	50	990.01†	$1017.3 \pm 0.3$	$984.5 \pm 0.4$
TIG	30	1002.98†	$1000.5 \pm 0.3$	$968.4 \pm 0.4$
TIG	20	1012.61†	$988.1 \pm 0.3$	$957.6 \pm 0.3$
TIG	10	1020.68†	$973.5 \pm 0.3$	$954.5 \pm 0.3$

Phase-behavior of PEO oligomers was not used as a target property during the parametrization of the new model. However, we checked that it is correctly reproduced for the specific case of triglyme (PEO tetramer). Simulations of water/triglyme mixtures (at 303.15 K and 1 bar pressure) were carried out at 6 different concentrations in the range from 10 mol% PEO to 80 mol% PEO. In this concentration range no demixing is observed, consistently with experiments.<sup>45</sup>

Table 4 shows the density of these mixtures measured in experiment, simulation using the Lee model and simulation using our model. Both MARTINI models deviate less than 5% from the experimentally measured values and our model improves over the Lee model in the high concentration regime. Moreover, we calculated the density of pure liquids for four short PEO

oligomers, namely dimethoxyethane, Diglyme, Triglyme, and Tetraglyme, at 298.15 K. The calculated densities agree fairly well with experimental values (Table 4), with a maximum deviation of 3%, lower than observed with the Lee model. Such agreement suggests that small PEO oligomers could be used as bulk solvents in MARTINI.

### Long range structural properties

To obtain long range structural properties we simulated single PEO chains with different molecular weights, ranging from 1.2 kg/mol ( 27 monomers) to 21 kg/mol ( 477 monomers), in three different solvents. The simulations in Water and Benzene, which are both good solvents<sup>43</sup>, were carried out at 298.15 K and 1 bar pressure. The simulation in Diglyme (DGL) was run at 323.15 K (50degC), at which the otherwise bad solvent becomes a theta-solvent.<sup>31</sup>

**Radius of gyration** It is possible to compute the radius of gyration ( $R_G$ ) directly from simulation data.  $R_G$  is defined as the root mean square of the distance of all ( $N$ ) atoms of the polymer chain from their center of mass ( $CoM$ ).

$$R_G = \frac{1}{N} \sum_{k=1}^N (\vec{R}_k - \vec{R}_{CoM})^2 \quad (2.2)$$

MARTINI polymer models are often parametrized not only to reproduce small oligomer free energies of transfer but also long range structural properties such as the radius of gyration ( $R_G$ ).<sup>25919</sup>  $R_G$  for PEO-477 (20.988 kg/mol) in water was our target during the parametrization stage. On the other hand, we also validate our model by comparing the  $R_G$  for 6 other molecular weights in three different solvents to radii of gyration derived from experiment.

Comparing  $R_G$  from experiment to simulation is not always straightforward. Experimental radii of gyration result from either direct or indirect measurements. Direct measurements, such as those obtained from light scattering, usually pertain to large molecular weights ( $M_w > 100$  kg/mol), generally beyond those used in simulations. Hence, direct measurements can only be compared to simulation results by extrapolation. Indirect measurements, on the other hand, yield physical properties of polymer solutions at low concentrations. These properties, such as the intrinsic viscosity, can then be related to using theoretical or empirical models of real polymers. Intrinsic viscosity measurements are accurate and possible also for lower  $M_w$  ( $> 1$  kg/mol), comparable to the PEO chains simulated here. To validate our

model, we used both approaches: extrapolation of  $R_G$  from direct measurements, and estimation of  $R_G$  from intrinsic viscosity data. The details of both approaches are reported in the Appendix D.

All radii of gyration obtained by simulation with our new PEO model in comparison to experimental reference data are shown in Figure 2.3. For water (panel A) the experimental reference data consists of an extrapolation from high molecular weight scattering data<sup>46</sup> (dashed blue line Figure 2.3), three single points (blue triangles Figure 2.3) measured by scattering experiments at high molecular weight,<sup>44</sup> and estimates based on low molecular weight intrinsic viscosity measurements.<sup>46</sup> All three data sets agree well with each other and also with the radius of gyration produced by our model. For the three molecular weights (2.0 kg/mol, 3.784 kg/mol, and 5.148 kg/mol) for which both simulation data and an estimate from viscosity data exists, a direct comparison can be made. For the two high molecular weights, the radius of gyration from simulation matches the one estimated from experiment within the standard error. At the lowest molecular weight, the match is not exact but the deviation is only 3% (see table S.3.1).

Using Flory theory to estimate the free energy of a polymer chain in a good solvent, it can be shown that the scaling relationship between radius of gyration and molecular weight is a power law, i.e.,  $R_G \propto M_w^\nu$ , with  $\nu = 0.6$ . However, a more sophisticated theoretical treatment gives an exponent of 0.588.<sup>32</sup> Fitting experimental scattering data<sup>46</sup> to the same power law yields an exponent of 0.58, and fitting the data from the new MARTINI model yields  $0.583 \pm 0.002$ ; this value is in excellent agreement with both the theories and the experimental data at higher molecular weight. On the other hand, we notice that a power law fit to the radii of gyration estimated from intrinsic viscosities yields an exponent of  $0.552 \pm 0.002$ . Considering that our model reproduces well the values of  $R_G$  from viscosity estimates, extrapolation and scattering over almost two orders of magnitude of  $M_w$ , we consider this deviation in scaling negligible. Overall, the agreement of our model and the experimental reference data is very satisfactory.

Figure 2.3B shows the radii of gyration for PEO in Benzene based on estimates from intrinsic viscosity measurements, and based on simulations with our new model. In general, the simulated values (red hexagons) are close to the reference values (blue squares). A direct comparison between the two is only possible for two molecular weights: 3.784 kg/mol (A) and 2.0 kg/mol (B). At the high molecular weight (A) we obtain a radius of gyration of  $2.40 \pm 0.02$  nm from simulations and a radius of gyration of  $2.11 \pm 0.01$  nm from experiment. The difference between the two values is 0.26 nm, corresponding to a relative deviation of about 14%. For the shorter

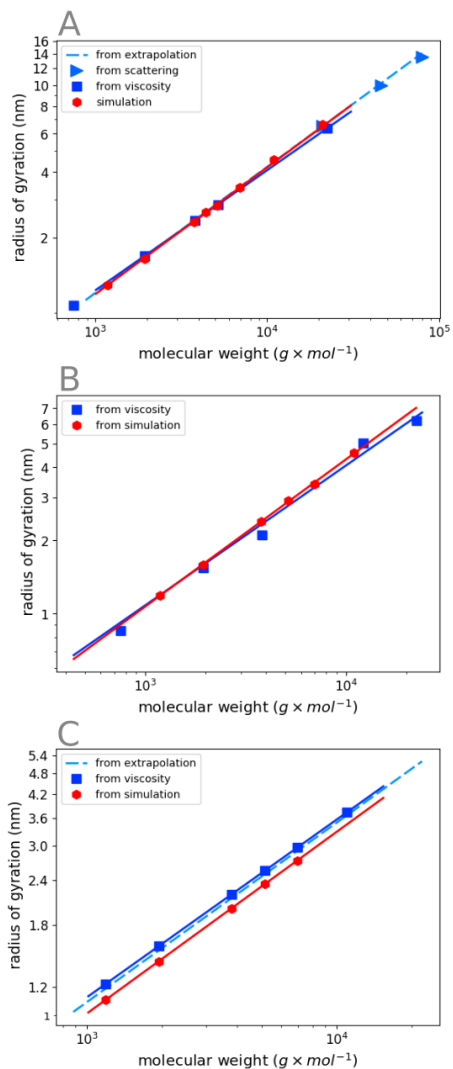


Figure 2.3: Radius of gyration for PEO as a function of molecular weight observed in different solvents: (A) Water, (B) Benzene, and (C) Diglyme. Blue markers are experimental reference values obtained by the methods outlined in Appendix D. The dashed lines are extrapolations and the solid ones fits to the corresponding (same color) data points.

PEO chain (B), the CG model yields a radius of gyration of  $1.585 \pm 0.005$  nm, which is much closer to the experimental value ( $1.539 \pm 0.007$  nm); the relative deviation is about 3%. Overall, the deviation of our new model from the experimental reference values appears to be acceptable, bearing in mind that the error for the reference radii of gyration is only a lower bound to the real error (see also Appendix D). In addition, the CG model produces a scaling exponent of  $0.603 \pm 0.004$ , in perfect agreement with the expected value for a good solvent and with the fit of the experimental data ( $0.602 \pm 0.003$ ).

Figure 2.3C shows the radii of gyration for PEO in Diglyme based on estimates from intrinsic viscosity measurements, based on extrapolation, and obtained from simulations with our new model. The estimates from intrinsic viscosity data (blue squares) are very close to the extrapolation from scattering data (blue dashed line). The estimated radii of gyration from our CG model are somewhat smaller. At a molecular weight of 3.784 kg/mol, the CG model predicts a radius of gyration of  $2.002 \pm 0.007$  nm, whereas the estimated reference value is  $2.189 \pm 0.009$  nm. The deviation is about 10%, similar to the deviation obtained at other molecular weights (see table S.3.1). Such deviation can be ascribed in part to the higher temperature, at which the performance of our CG model becomes worse. However, overall the results from our model are in reasonable agreement with both experimental data sets over the entire range of molecular weights. In addition, the scaling exponent for the CG model is  $0.511 \pm 0.003$ , in good agreement with experimental data (0.505 from scattering measurements<sup>46</sup>) and close to 0.5, which is the value predicted by ideal chain statistics for a chain in a theta solvent.<sup>32</sup>

**End-to-End distance and Kuhn Length** It can be shown from statistical calculations that, for sufficiently long chains, the squared end-to-end distance of a polymer chain ( $\langle R^2 \rangle$ ) in a theta solvent is proportional to the bond length ( $l$ ), the number of back-bone bonds ( $n$ ), and a constant referred to as Flory's Characteristic ratio ( $C_\infty$ ):<sup>32</sup>

$$\langle R^2 \rangle = C_\infty \times n \times l^2 \quad (2.3)$$

Diglyme at 50degC is a theta solvent for PEO<sup>31</sup> - in good agreement with our simulations, which is indicated by the scaling exponent of about 0.5. Therefore,  $C_\infty$  can be obtained by fitting the above relation to the squared end-to-end distance of our model in diglyme (see Figure 2.4). From this procedure we obtain a value for  $C_\infty$  of  $2.45 \pm 0.002$  nm, close to the value previously reported for the Lee model<sup>7</sup> (2.7 nm). The value of  $C_\infty$  is related

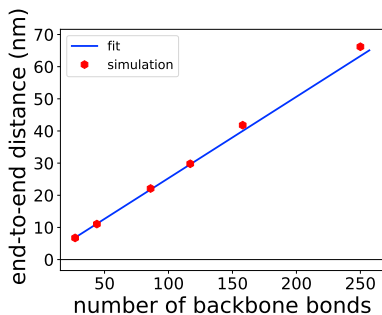


Figure 2.4: Squared end-to-end distance (red hexagons) and fit (blue line) for the new MARTINI model as function of the number of backbone-bonds (i.e. 1 in case of our CG model) in diglyme, which is a theta solvent.

to the Kuhn length ( $b$ ) and to the persistence length ( $l_p$ ), which both can be interpreted as a measure of the polymer stiffness. From  $C_\infty$  we can compute the persistence length according to:<sup>7</sup>

$$l_p = C_\infty \times \frac{1}{2} \times l \quad (2.4)$$

or the Kuhn length<sup>32</sup> following the equation:

$$b = \frac{C_\infty \times l}{\cos(\theta)} \quad (2.5)$$

The bond length ( $l$ ) is given by 3.22 Å and the angle in our model is 45 degrees. This leads to a persistence length of 3.95 Å, which compares fairly well to the experimental value of 3.7 Å.<sup>7</sup> Similarly, the Kuhn length of 11.56 Å calculated from simulations compares well with the value measured in the PEO melt (11.0 Å<sup>32</sup>).

### PEGylated lipids

PEGylated lipids are interesting from the pharmaceutical standpoint for their applications in drug delivery.<sup>48</sup> From a polymer physics standpoint, membranes containing PEGylated lipids mimic PEO grafted to a solid surface. Chain dimensions in grafted polymers can be sorted into two regimes depending on the grafting density. In the low grafting density regime, known as “mushroom regime”, the chains are well separated, interact minimally, and therefore move freely within a space approximating

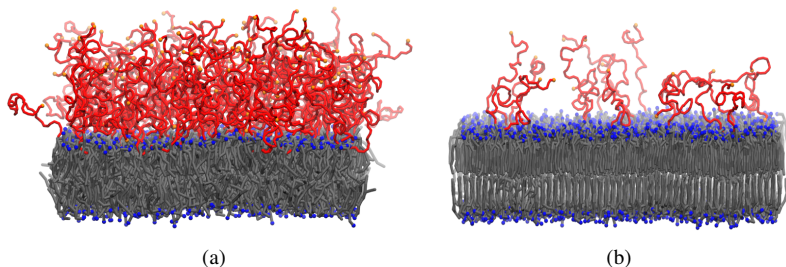


Figure 2.5: Lipid bilayers at low (a) and high (b) concentration of PEGylated lipids after 4  $\mu$ s. Acyl chains are colored in gray, choline head groups in blue, PEO chains in red and terminal SP2 bead in orange. Water is not represented for the sake of clarity. The image was prepared using the VMD program.<sup>47</sup>

a half-sphere.<sup>48</sup> In contrast in the high grafting density regime (“brush regime”), the polymer chains are close in space and repel each other. This repulsion leads to more extended chain dimensions than in the mushroom regime. To verify that our model can reproduce this difference in dimension and therefore can be used as a new model for PEGylated lipids, we simulated two patches of PEGylated lipid-bilayers in water.

The grafting densities of the patches were  $\sigma = 0.034 \text{ nm}^{-2}$  and  $\sigma = 0.42 \text{ nm}^{-2}$ ; the areas per lipid were  $0.46 \text{ nm}^2$  and  $0.598 \text{ nm}^2$  respectively. Although the first bilayer was in a gel state, as expected for a bilayer mainly containing DPPC lipids at 283K, the second bilayer appeared to be in the liquid crystalline state, probably due to the larger amount of unsaturated tails of the PEL lipids combined with the repulsive interaction among the polymer chains. We do not expect the phase of the bilayer to have an effect on the PEO chain dimensions, however. By visually inspecting the PEO chains, the dimensions look like the anticipated mushroom at low grafting density (Figure 2.5a) and brush at high grafting density (Figure 2.5b). To quantify the difference in dimension the end-to-end distance of the PEO chains was computed. In case of the low grafting density, a value of  $4.44 \pm 0.02 \text{ nm}$  is obtained, significantly smaller than the end-to-end distance in the brush regime ( $5.21 \pm 0.02 \text{ nm}$ ). The chains in the brush regime are more extended than in the mushroom regime, as expected from theory and observed experimentally.<sup>48 49 50</sup>

As evident from chain dimensions, our new model for PEGylated lipids

does not show strong adsorption of the PEO chains onto the lipid bilayer surface, contrary to the first Lee model.<sup>8</sup> Although some other coarse-grained models show enhanced adsorption onto the lipid bilayers, data from both atomistic simulations and experiment suggests that the PEO chains should not do so.<sup>48</sup> Thus our model displays the correct qualitative behavior without refinement.

The chain dimensions in the mushroom regime can be assessed in relation to experiment by estimating the end-to-end distance from an experimentally accessible parameter: the Kuhn length. According to Flory theory, the end-to-end distance for an isolated chain grafted to a surface (i.e., mushroom regime) is given by:<sup>32</sup>

$$R_F = b^{\frac{2}{5}} \times (3 \times n_{monomers} \times l \times \cos(\frac{\theta}{2}))^{\frac{3}{5}} \quad (2.6)$$

with being the Kuhn length, the number of bonds per chain, and the average bond length. The angle is 180 degrees minus the average angle between two consecutive bonds. Details on deriving the Kuhn length from experiment and the other quantities are presented in the Appendix E. For the low grafting density ( $\sigma = 0.034$ ), the end-to-end distance from our simulation ( $4.44 \pm 0.02$  nm) compares very well to the estimated value of ( $4.8 \pm 0.4$  nm). Similarly, the chain dimensions in the brush regime can be assessed by estimating the height of the brush ( $H$ ) in terms of the Kuhn length and the grafting density ( $\sigma$ ). Using Alexander - de Gennes theory, the height is given by:<sup>32</sup>

$$H = 3 \times n_{monomers} \times l \times \cos(\frac{\theta}{2} \times b^{\frac{3}{2}} \times \sigma^{0.65}) \quad (2.7)$$

where  $\sigma$  is the number of grafting points per unit area (i.e. the number of PEGylated lipid per unit area). Appendix D offers more details on the approximations and quantities involved in this equation. The estimated brush height is  $8 \pm 2$  nm.

To define the height of the brush from simulation is somewhat more difficult, as there is no well accepted procedure. Previously, Lee et al. have used the peak of the density profile computed with respect to the choline head group as the height of the brush.<sup>7</sup> Such profile is shown in Figure 2.6 (red line). The peak is located at 3.3 nm, smaller than the end-to-end distance and much smaller than the estimate based on Alexander-de Gennes theory ( $8 \pm 2$  nm). In contrast, the peak ( $7.5 \pm 1.0$  nm) of the density profile of only the SP2 chain-end beads (orange line in Figure 2.6), reminiscent of the less dense brush top, is in good agreement with the estimated value. Yet

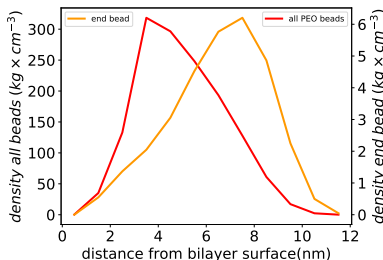


Figure 2.6: Density profile of the PEO beads (red) and of only the SP2 beads (orange) with respect to the bilayer surface, taken as the choline head group (indicated in blue in Figure 2.5).

a third measure of the brush height in simulation could be the average end-to-end distance ( $5.21 \pm 0.02$  nm), which lies in-between the two previous measures. Overall, a direct comparison between simulation results and Alexander-de Gennes theory appears to be problematic, possibly due to the assumption (in the theory) of idealized straight chains. In conclusion, the new model (1) can reproduce the difference in size of PEO chains in PEGylated lipids, both at low and high grafting densities; (2) does not suffer from artificially high aggregation of chains at the bilayer surface; (3) yields reasonable chain sizes in comparison to experimental estimates.

### Nonionic surfactants

Non-ionic surfactants with a PEO head group and an alkyl tail are another important application of PEO. In water, they display a rich phase-behavior. In simulations, such phase-behavior is very sensitive to both bonded and non-bonded interactions. Hence, the phase-behavior of non-ionic surfactants is an ideal, stringent test for any PEO model. Because of the richness of phase-behavior in non-ionic surfactants, we selected only 3 specific cases, in which surfactants produce different morphologies; these specific cases are the same selected in the previous work by Rossi et al., to simplify the comparison.<sup>9</sup> Three non-ionic surfactants, namely C12E6, C12E4 and C12E2, were simulated in water at three different concentrations, corresponding to unambiguous regions in their respective phase diagrams<sup>9</sup> (Figure 2.7, lower panels). Surfactant molecules were initially distributed randomly in the simulation box. Self-assembly simulations were repeated 6 times for each surfactant and each concentration, each time with a different

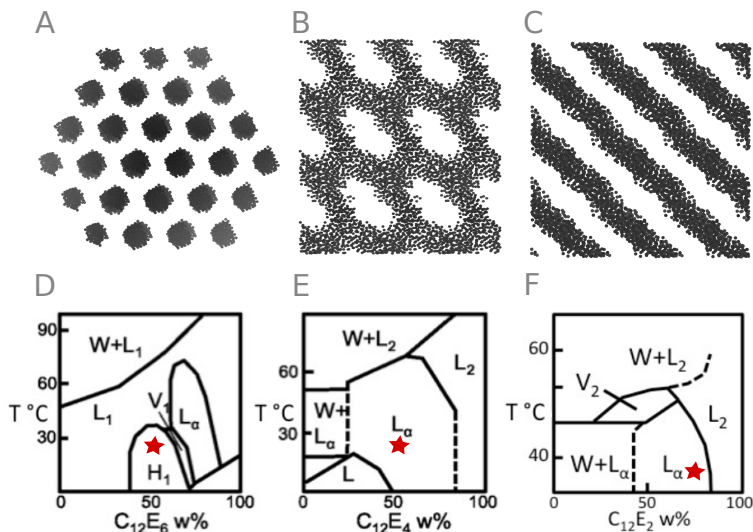


Figure 2.7: Figure 2.7 . Snapshots of non-ionic surfactant phases (A-C) after  $5 \mu\text{s}$  and corresponding phase diagrams (D-E) taken from ref.<sup>9</sup>. Only the carbon atoms are shown. Panels A and D correspond to C12E6, panels B and E to C12E4 and panels C and F to C12E2. In the phase diagram H1 indicates a hexagonal phase, while  $L\alpha$  indicates lamellar phases. The other phases observed experimentally are V1 (direct cubic), V2 (inverse cubic), L2 (water in surfactants) and W (surfactants in water).<sup>9</sup> The red star indicates the composition temperature point sampled. The pictures of panels A-C were made using VMD.<sup>47</sup>

random-seed to generate different random velocities from a Maxwell distribution at the appropriate temperature. C12E6 was simulated at 50% (w/w) water content. At the temperature of 298.15 K, the phase diagram indicates that a hexagonal phase should form<sup>9</sup>. In self-assembly simulations, we obtained tubular micelles in 5 out of 6 cases, and in 3 out of 6 the tubes have hexagonal symmetry (Figure 2.7, panel A). Only 1 out of 6 simulations yielded an unidentifiable phase. C12E4 at 53% (w/w) water at the temperature of 298.15 K forms lamellar phases, according to the experimental phase diagram<sup>9</sup>. In self-assembly simulations, we obtained lamellar structures (Figure 2.7, panel B), in 4 out of 6 cases (the remaining 2 simulations gave tubular micelles). However, the lamellae showed holes. Whereas the holes could not be identified in x-ray scattering experiments, more recent NMR data clearly shows that the order parameter is not compatible with intact lamellar phases, and instead are compatible with a perforated lamellar phase.<sup>51</sup> We notice that the Rossi model also produced perforated lamellae (3 cases out of 6).<sup>9</sup> Finally, C12E2 at 71.1% (w/w) water content and at 298.15 K forms lamellar phases, according to the phase diagram. In self-assembly simulations, the surfactant formed intact lamellae in 6 out of 6 cases (Figure 2.7, panel C). Overall, the new model is able to predict the correct phase-behavior as observed experimentally in the three cases tested here. Also, in such cases, the agreement with experimental phase-behavior is better than observed for the previous PEO model.<sup>9</sup>

### PS-PEO block-copolymer aggregates

PEO is not only frequently used as component of biomolecular systems, but is also a very important polymer in material science and engineering. Recently the block-copolymer of polystyrene (PS) with PEO (PS-*b*-PEO) has attracted some attention in theoretical studies on Lithium ion conducting polymers.<sup>52,53,54</sup> Short oligomers of PS-*b*-PEO form micelles in water. The size and the aggregation number of these micelles have been characterized by x-ray scattering.<sup>55</sup> We tested the possibility to combine the new PEO model with the existing MARTINI model of PS,<sup>2</sup> by simulating two systems of 370 and 740 PEO-*b*-PS oligomers in water; each chain contained 23 consecutive PEO units and 10 consecutive PS units.

In the beginning of both simulations, small micelles were formed, which later fused to generate bigger micelles. The PEO part of the polymer wrapped around the PS, creating a PS core and a PEO corona, as to shield PS from water. For the smaller system, after 2.5  $\mu$ s only 4 micelles remained (formed by 15, 34, 102 and 219 oligomers. For the larger system,

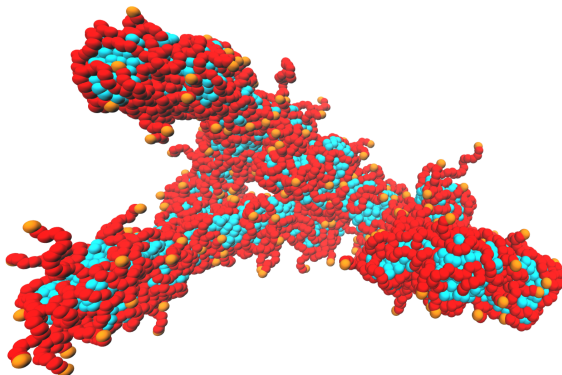


Figure 2.8: Single PS-PEO block copolymer micelle (219 oligomers) in water after 3.4 microseconds. The PEO part is shown in red while the PS part is cyan and water is omitted for clarity. The picture was made using VMD.<sup>47</sup>

after the same period of time, 9 micelles remained (formed by 456, 49, 37, 36, 64, 15, 41, 23, 20 oligomers). These micelles were stable for about  $1 \mu\text{s}$  in both cases. The aggregation number of the largest micelle does not match the experimentally determined aggregation number (370 oligomers<sup>55</sup>), in both of our simulated systems. At the same time, the radius of gyration of the largest micelle for the first system ( see Figure 2.8) (7nm) and for the second system (9nm) fall in the same ballpark as the experimentally determined value ( $6.3 \pm 1 \text{ nm}$ <sup>46</sup>). The discrepancy in micelle size may simply be due to time scale limitations: fusion of smaller micelles with the larger ones or division of larger micelles into smaller ones probably occurs on time scales larger than those accessible in our simulation. In addition, the large gap between the aggregation number of the small micelles and the large one suggests that the larger one is favored and kinetic barriers prevent further fusion or division. Length scale limitations may also play a role: in real systems, micelles are polydisperse, i.e., they have a range of different sizes and aggregation numbers, and exchange monomers dynamically; in simulations, such dynamic equilibrium would imply system sizes currently out of reach, even for coarse-grained models. We note that previous studies of micelle formation (with other surfactants<sup>8 11</sup>) using MARTINI models also yielded only qualitative agreement with experiment. Our results indi-

cate that the new PEO model can be combined with the existing PS-model without modifications.

## 5.0 Conclusions

Motivated by the deficiencies of the previous MARTINI PEO models in apolar environments, we developed a new PEO model based on (a) a set of 8 free energies of transfer of dimethoxyethane (PEO dimer) from water to solvents of varying polarity; (b) the radius of gyration of a PEO-477 chain in water at high dilution; (c) matching angle and dihedral distributions from atomistic simulations. The radius of gyration for PEO chains of different length in different solvents was not used in the parametrization, but it turned out to be in good agreement with experiments. We showed that the model can be used on a molecular weight range from about 1.2 kg/mol to 21 kg/mol (27 to 477 monomers) and possibly even higher. The new model successfully reproduces the phase-behavior and densities of small PEO oligomers in water. It can be used in polar as well as apolar solvents, such as Benzene. We also verified that the new model can be used as part of PEGylated lipids, and reproduces qualitatively the structural features of the lipid bilayers with PEGylated lipids in the brush and mushroom regime. Furthermore, the model is able to reproduce the phase-behavior of various non-ionic surfactants in water. Finally, we demonstrated that the new model can be combined with the existing MARTINI PS to model PS-PEO block-copolymers. In conclusion, the new parametrization captures all the essential properties of the previous models and improves on their deficiencies, yielding a highly transferable and stable coarse grained model for PEO.

# References

- [1] Marrink, S. J.; Risselada, H. J.; Yefimov, S.; Tieleman, D. P.; De Vries, A. H. *Journal of Physical Chemistry B* **2007**, *111*, 7812–7824.
- [2] Rossi, G.; Monticelli, L.; Puisto, S. R.; Vattulainen, I.; Ala-Nissila, T. *Soft Matter* **2011**, *7*, 698–708.
- [3] Rossi, G.; Elliott, I. G.; Ala-Nissila, T.; Faller, R. *Macromolecules* **2012**, *45*, 563–571.
- [4] Alessandri, R.; Uusitalo, J. J.; De Vries, A. H.; Havenith, R. W.; Marrink, S. J. *Journal of the American Chemical Society* **2017**, *139*, 3697–3705.
- [5] Panizon, E.; Bochicchio, D.; Monticelli, L.; Rossi, G. *Journal of Physical Chemistry B* **2015**, *119*, 8209–8216.
- [6] Vögele, M.; Holm, C.; Smiatek, J. *Journal of Chemical Physics* **2015**, *143*.
- [7] Nawaz, S.; Carbone, P. *Journal of Physical Chemistry B* **2014**, *118*, 1648–1659.
- [8] Lee, H.; Pastor, R. W. *Journal of Physical Chemistry B* **2011**, *115*, 7830–7837.
- [9] Rossi, G.; Fuchs, P. F.; Barnoud, J.; Monticelli, L. *Journal of Physical Chemistry B* **2012**, *116*, 14353–14362.
- [10] Bulacu, M.; Goga, N.; Zhao, W.; Rossi, G.; Monticelli, L.; Periolo, X.; Tieleman, D. P.; Marrink, S. J. *Journal of Chemical Theory and Computation* **2013**, *9*, 3282–3292.
- [11] Velinova, M.; Sengupta, D.; Tadjer, A. V.; Marrink, S. J. *Langmuir* **2011**, *27*, 14071–14077.
- [12] Taddese, T.; Carbone, P. *Journal of Physical Chemistry B* **2017**, *121*, 1601–1609.
- [13] Lee, H.; De Vries, A. H.; Marrink, S. J.; Pastor, R. W. *Journal of Physical Chemistry B* **2009**, *113*, 13186–13194.
- [14] Huston, K. J.; Larson, R. G. *Langmuir* **2015**, *31*, 7503–7511.
- [15] Janeliunas, D. *PhD Thesis* **2014**,
- [16] Yuan, R.; Teran, A. A.; Gurevitch, I.; Mullin, S. A.; Wanakule, N. S.; Balsara, N. P. *Macromolecules* **2013**, *46*, 914–921.

- [17] Panday, A.; Mullin, S.; Gomez, E. D.; Wanakule, N.; Chen, V. L.; Hexemer, A.; Pople, J.; Balsara, N. P. *Macromolecules* **2009**, *42*, 4632–4637.
- [18] Wanakule, N. S.; Panday, A.; Mullin, S. A.; Gann, E.; Hexemer, A.; Balsara, N. P. *Macromolecules* **2009**, *42*, 5642–5651.
- [19] Rossi, G.; Giannakopoulos, I.; Monticelli, L.; Rostedt, N. K. J.; Puisto, S. R.; Lowe, C.; Taylor, A. C.; Vattulainen, I.; Ala-Nissila, T. *Macromolecules* **2011**, *44*, 6198–6208.
- [20] Abraham, M. J.; Murtola, T.; Schulz, R.; Páll, S.; Smith, J. C.; Hess, B.; Lindah, E. *SoftwareX* **2015**, *1-2*, 19–25.
- [21] Shirts, M. R.; Chodera, J. D. *Journal of Chemical Physics* **2008**, *129*.
- [22] Klimovich, P. V.; Shirts, M. R.; Mobley, D. L. *Journal of Computer-Aided Molecular Design* **2015**, *29*, 397–411.
- [23] Horta, B. A.; Merz, P. T.; Fuchs, P. F.; Dolenc, J.; Riniker, S.; Hünenberger, P. H. *Journal of Chemical Theory and Computation* **2016**, *12*, 3825–3850.
- [24] Horta, B. A.; Fuchs, P. F.; Van Gunsteren, W. F.; Hünenberger, P. H. *Journal of Chemical Theory and Computation* **2011**, *7*, 1016–1031.
- [25] Senac, C.; Urbach, W.; Kurtisovski, E.; Hünenberger, P. H.; Horta, B. A.; Taulier, N.; Fuchs, P. F. *Langmuir* **2017**, *33*, 10225–10238.
- [26] Shirts, M. R.; Mobley, D. L. *An Introduction to Best Practices in Free Energy Calculations*; 2013; pp 271–311.
- [27] Goga, N.; Rzepiela, A. J.; de Vries, A. H.; Marrink, S. J.; Berendsen, H. J. C. *Journal of Chemical Theory and Computation* **2012**, *8*, 3637–3649.
- [28] Parrinello, M.; Rahman, A. *Journal of Applied Physics* **1981**, *52*, 7182–7190.
- [29] de Jong, D. H.; Baoukina, S.; Ingólfsson, H. I.; Marrink, S. J. *Computer Physics Communications* **2016**, *199*, 1–7.
- [30] Bussi, G.; Donadio, D.; Parrinello, M. *The Journal of Chemical Physics* **2007**, *126*, 014101.
- [31] Beech, D. R.; Booth, C. *Journal of Polymer Science Part A-2: Polymer Physics* **1969**, *7*, 575–586.
- [32] Colby, R. H.; Rubinstein, M. *New-York: Oxford University* **2003**, *100*, 274.
- [33] Berendsen, H. J. C.; Postma, J. P. M.; van Gunsteren, W. F.; DiNola, A.; Haak, J. R. *The Journal of Chemical Physics* **1984**, *81*, 3684–3690.
- [34] Wassenaar, T. A.; Ingólfsson, H. I.; Böckmann, R. A.; Tieleman, D. P.; Marrink, S. J. *Journal of Chemical Theory and Computation* **2015**, *11*, 2144–2155.
- [35] Pedregosa, F. et al. *Journal of Machine Learning Research* **2011**, *12*, 2825–2830.

- [36] Buitinck, L.; Louppe, G.; Blondel, M.; Pedregosa, F.; Mueller, A.; Grisel, O.; Niculae, V.; Prettenhofer, P.; Gramfort, A.; Grobler, J.; Layton, R.; Vanderplas, J.; Joly, A.; Holt, B.; Varoquaux, G. **2013**,
- [37] Ester, M.; Kriegl, H.-P.; Sander, J.; Xu, X. A Density-Based Algorithm for Discovering Clusters in Large Spatial Databases with Noise. KDD'96 Proceedings of the Second International Conference on Knowledge Discovery and Data Mining Pages. Portland, Oregon, 1996; pp 226–231.
- [38] Gowers, R. J.; Linke, M.; Barnoud, J.; Reddy, T. J. E.; Melo, M. N.; Seyler, S. L.; Domański, J.; Dotson, D. L.; Buchoux, S.; Kenney, I. M.; Beckstein, O. MDAnalysis: A Python Package for the Rapid Analysis of Molecular Dynamics Simulations. 98 PROC. OF THE 15th PYTHON IN SCIENCE CONF. Austin, Texas, 2016; pp 98–105.
- [39] Michaud-Agrawal, N.; Denning, E. J.; Woolf, T. B.; Beckstein, O. *Journal of Computational Chemistry* **2011**, *32*, 2319–2327.
- [40] Chodera, J. D.; Swope, W. C.; Pitera, J. W.; Seok, C.; Dill, K. A. *Journal of Chemical Theory and Computation* **2007**, *3*, 26–41.
- [41] Hess, B. *Journal of Chemical Physics* **2002**, *116*, 209–217.
- [42] Young, R. J.; Lovell, P. A. *Introduction to polymers*; CRC press, 2011.
- [43] Bluestone, S.; Mark, J. E.; Flory, P. J. *Macromolecules* **1974**, *7*, 325–328.
- [44] Kato, T.; Nakamura, K.; Kawaguchi, M.; Takahashi, A. *Polymer Journal* **1981**, *13*, 1037–1043.
- [45] Henni, A.; Naami, A.; Tontiwachwuthikul, P. *Journal of Chemical & Engineering Data* **2005**, *50*, 1038–1042.
- [46] Kawaguchi, S.; Imai, G.; Suzuki, J.; Miyahara, A.; Kitano, T.; Ito, K. *Polymer* **1997**, *38*, 2885–2891.
- [47] Humphrey, W.; Dalke, A.; Schulten, K. *Journal of Molecular Graphics* **1996**, *14*, 33–38.
- [48] Lee, H.; Larson, R. G. *Biomacromolecules* **2016**, *17*, 1757–1765.
- [49] Hansen, P. L.; Cohen, J. A.; Podgornik, R.; Parsegian, V. A. *Biophysical Journal* **2003**, *84*, 350–355.
- [50] Kenworthy, A. K.; Hristova, K.; Needham, D.; McIntosh, T. J. *Biophysical Journal* **1995**, *68*, 1921–1936.
- [51] Ferreira, T. M.; Topgaard, D.; Ollila, O. H. S. *Langmuir* **2014**, *30*, 461–469.
- [52] Chu, W.; Qin, J.; De Pablo, J. J. *Macromolecules* **2018**, *51*, 1986–1991.
- [53] Sethuraman, V.; Mogurampelly, S.; Ganesan, V. *Macromolecules* **2017**, *50*, 4542–4554.
- [54] Young, W.-s.; Albert, J. N. L.; Schantz, A. B.; Epps, T. H. *Macromolecules* **2011**, *44*, 8116–8123.
- [55] Jada, A.; Hurtrez, G.; Siffert, B.; Riess, G. *Macromolecular Chemistry and Physics* **1996**, *197*, 3697–3710.



## Chapter 3

# MARTINI model for Lithium Bistriflimide

“ *Do not quench your inspiration and your imagination; do not become the slave of your model.*

”

---

Vincent Van Gogh,

## Summary

An atomistic and coarse-grained model for Lithium Bistriflimide (LiTFSI) is presented. The atomistic model is compatible with the GROMOS 2016H66 force-field, while the coarse-grained model is compatible with the MARTINI force-field. The TFSI was parametrized by (a) matching relative (QM-level) energies of conformers, (b) matching the QM dihedral rotation profile, and (c) reproducing the experimental density of the ionic liquid 1-Butyl-1-methylpyrrolidinium Bistriflimide (pyr14 TFSI). Subsequently the Lithium TFSI interaction strength was refined by reproducing qualitatively the experimental salt dissociation populations in dimethoxyethane (DXE). Using the atomistic model as reference the coarse-grained model was developed by matching the angle and dihedral distributions of atomistic LiTFSI in triglyme. After refinement of the EO Lithium interactions, the MARTINI model was able to correctly produce the LiTFSI association/dissociation properties in DXE (representative of the PEO phase) and benzene (bulk solvent and representative of the PS phase).

## Introduction

The Lithium salt is one of the key components of single-polymer-electrolytes (SPEs). SPEs work best if the salt largely dissociates in the conducting polymer phase and when the anion mobility is low.<sup>1</sup> Relatively low anion mobility and high degree of dissociation makes Lithium bistriflimide (LiTFSI, cf. 3.1a) one of the most studied and used salts in this context. However, the salt not only functions as charge carrier, but also enhances the phase-separation; the segregation strength ( $N\chi_{eff}$ ) is increased when salt is added to a block-copolymer system. This increase in segregation strength is often described in terms of an increased effective Flory-Huggins interaction parameter ( $\chi_{eff}$ ).<sup>2</sup> For modeling the phase-separation and self-assembly process of these block-copolymers it is therefore important to take this effect into account. This chapter presents the development of a MARTINI version of LiTFSI. In the spirit of MARTINI the model is parametrized based on experimental data and atomistic simulations.

## Methods

**QM calculations** Calculations using the theory of quantum mechanics were performed to obtain conformational properties of the TFSI anion; the minimum energy conformations along one dihedral rotation were determined as well as the energy profile of the rotation based on a restricted scan. The restricted scan gives an indication of the barrier of rotation of two strongly coupled dihedral angles, as the other dihedral is fixed. All optimizations were conducted using density-functional-theory (DFT) with the B3LYP exchange-correlation functional and the 6-31G\* basis set. The basis set and QM method (i.e. DFT/B3LYP) was chosen to be the same as used by the Automated Topology Builder (ATB).<sup>3</sup> For all calculations the program ORCA (4.0.1) was used employing a large DFT grid (Grid5) and numerical frequencies.

Partial charges were quantum mechanics based as well. To obtain partial charges the geometry of a single TFSI anion was optimized in vacuum at B3LYP/TZP level. Subsequently charge-model 5 (CM5) charges were obtained employing the Amsterdam Density Functional code (ADF) implementation of the method proposed by Marenich and coworkers.<sup>4</sup> The raw charges were then balanced in the third digit to yield fully symmetric charges and a neutral molecule. Note that this balancing process, since it is in the third digit will have no noticeable effect on the properties. Many force-fields do not even report charges up to that level of accuracy.

**Atomistic simulations** Mixtures of dimethoxyethane (DXE), triglyme (TRG), benzene (BENZ) with Lithium bistriflimide (LiTFSI), were simulated at the atomistic level. Table 3.1 gives an overview about all simulations. Additionally three simulations of the ionic liquid 1-Butyl-1-methylpyrrolidinium bis(trifluoromethanesulfonyl)imide (pyr14-TFSI) were performed (cg. table 3.2). Both sets of simulations were conducted using the GROMOS 2016H66 force-field by Horta et al.<sup>5</sup> with the run parameters adopted to GROMACS as discussed in chapter two; the oxygen Lithium interactions of the TFSI oxygens were refined with respect to the original force-field (C6:  $9.3241645 \times 10^5$ , C12:  $1.23375 \times 10^{-7}$ ) by matching the experimental degree of salt-dissociation in dimethoxyethane. In all cases the pressure was kept constant at 1 bar using the Parrinello-Rahman barostat.<sup>6</sup> The temperature was either kept constant by the stochastic-dynamics (SD) integrator<sup>7</sup> or the v-rescale thermostat by Bussi and coworkers.<sup>8</sup> A time-step of 2fs was used for the integration. Compressibility and the dielectric constant were set to the value of the major system component.

Table 3.1: Atomistic Simulations of LiTFSI dimethoxyethane (DXE), triglyme (TRG), Benzene (BENZ) mixtures

solvent	conc. LiTFSI	length	temperature	force-field
DXE	8.8mol%	130 ns	303.15K	refined
DXE	14.9mol%	130 ns	303.15K	refined
DXE	20mol%	130 ns	303.15K	refined
DXE	24.8mol%	130 ns	303.15K	refined
DXE	20 mol%	60 ns	303.15K	original
TIG	5.0 mol%	130 ns	303.15K	refined
BENZ	10.0 mol%	190 ns	298.15K	refined

*note that refined refers to the GROMOS-2016H66 force-field with refined parameters for the oxygen Lithium interactions of TFSI.*

Table 3.2: Atomistic Simulations of bistriflimide and 1-Butyl-1-methylpyrrolidinium bis(trifluoromethanesulfonyl)imide (pyr14)

ionic-liquid	length	temperature	force-field	atom-types
TFSI-pyr14	29.0 ns	393K	original	ATB-choice
TFSI-pyr14	31.7 ns	393K	original	refined-choice
TFSI-pyr14	22.3 ns	298.15K	original	refined-choicie

For the ionic-liquids the dielectric constant of the reaction field was set to 60. It should be noted some tests with the dielectric constant indicated it does not have a large effect on the density. All bonds were constrained using the LINCS algorithm.

**Coarse-Grained simulations** Mixtures of DXE or Benzene with LiTFSI were simulated at 298.15K using the MARTINI force-field<sup>9</sup> version 2, including the new PEO parameters presented in chapter 2. Table 3.3 gives an overview over all simulations. The pressure was kept constant at 1 bar using the Parrinello-Rahman barostat<sup>6</sup>, while the temperature was fixed using the v-rescale thermostat by Bussi and coworkers<sup>8</sup>. The run settings were the same as suggested by de Jong et al.<sup>10</sup> (cut-off for non-bonded interactions: 1.1 nm; Verlet neighborlist scheme) with the exception of the verlet-buffer-tolerance, which was decreased from the GROMACS default value to 10 -6 kJ/mol/ps per particle. It should be noted that MARTINI is usually used with a dielectric constant of 15 to make up for non-existent partial charges. This dielectric constant has been specifically

Table 3.3: Coarse-Grained simulations of of LiTFSI dimethoxyethane (DXE), triglyme (TIG), Benzene (BENZ) mixtures

solvent	conc. LiTFSI	length	temperature	force-field
DXE	14.0 mol%	106 ns	298.15K	refined
DXE	14.0 mol%	300 ns	298.15 K	original
TIG	4.0 mol%	126 ns	298.15K	refined
BENZ	10.0 mol%	212 ns	298.15 K	refined

*note that original refers to the MARTINI force-field (version 2 incl. the new paramters for PEO); refined refers to the same force-field except for changed PEO Lithium interaction paramters*

chosen for ion performance in the context of lipid membranes and water.<sup>9</sup> Although the dielectric constant of Benzene and DXE, which are the main solvents, are around 2 and 7 respectively<sup>11</sup> it was decided not change the dielectric constant. The main reason is that the charged-bead LJ interaction parameters were designed in part to make up for non-existent partial charges as well. On the other hand, they assume a dielectric constant of 15 as well. Thus changing the dielectric constant to some lower value could lead to larger repulsion between like ions and more attraction between unlike ions. As discussed in the next section it could be worth overall testing different dielectric constants and employing corrections for cutting of electrostatics.

$$f_{contac} = \frac{contacts(A,B)}{contacts(A,B) + contacts(A,A) + contacts(B,B)} \quad (3.1)$$

One method for classifying the degree of phase-separation is to compute the contact fraction. Sometimes the contact fraction is only normalized by the cross-contacts plus the self-contacts of the solute<sup>12</sup>. However, in this case we find it more useful to normalize by the total number of contacts (cf. 3.1). As the contact fraction decreases the mixture shows less mixing until it is fully phase-separated. The contacts between one phase and the other are computed by defining a cut-off and counting all molecules within this cut-off as having contact. In this study the cut-off was set to the non-bonded interaction cut-off as done previously for the clustering algorithm. In order to define the degree of phase-separation in the salt solvent system we counted all the solvent - TFSI anion contacts and all TFSI TFSI contacts in the mixture. Statistical analysis was conducted using the tools presented in Appendix C. Note that we do not count the Lithium ion contacts, because there will always be little Lithium ions around each

other; this means contacts(A,A) is always small regardless of whether the salt is fully associated or dissociated. In contrast TFSI is a large anion with uncharged CF<sub>3</sub> groups and large charge delocalization. Hence one can assume in the associated salt TFSI ions are fairly close to each other in space; at least they are much closer than in solvent-separated-ion-pairs. The equations of motion were integrated using the standard GROMACS MD integrator with a time-step of 20fs.

## Atomistic Model

Due to a lack of a good atomistic reference, it was decided to first develop a LiTFSI model compatible with the GROMOS 2016H66 force-field<sup>5</sup>; 2016H66 was already used in chapter 2 as basis for developing the coarse-grained PEO model. Thus with this choice largest compatibility between the two parametrizations is intended. Additionally the force-field already contains parameters for a Lithium cation. Hence only the anion needed to be parametrized from scratch to obtain the atomistic reference model.

The initial parameters for the TFSI anion were taken from the Automated-Topology-Builder (ATB).<sup>13 14 3</sup> Subsequently the TFSI model was refined by (1) selecting better atom types based on the density of ionic liquids, (2) computing new charges, and (3) refitting the dihedral potential. In the last stage the interactions with Lithium were optimized as well. Overall the new LiTFSI is supposed to show a reasonable amount of association and dissociation in dimethoxyethane and benzene. By extension we hoped to capture the appropriate dissociation effects in PEO and avoid too large salt aggregation; pronounced aggregation could negatively influence the self-assembly process and hinders charge transport. Because Benzene is the main solvent of the system of interest and also representative for a large part of Polystyrene, it is important to ensure the salt behaves reasonable in Benzene.

## Charges and Atom-Types

The atom-types (taken from the ATB<sup>13 14 3</sup>) were refined based on the density of the ionic liquid 1-Butyl-1-methylpyrrolidinium-bis-(trifluoromethanesulfonyl)-imide (pyr14-TFSI). The cation parameters were also taken from the ATB.<sup>13 14 3</sup> Using these initial parameters a density of  $1484 (\pm 1) \text{ kg} \times \text{m}^{-3}$  was obtained at 393K; the temperature was chosen to enhance equilibration of the otherwise slowly diffusing ionic-liquids.

Table 3.4: charges and atom-types of the bistriflimide anion

(a) CM5 charges		(b) atom-types	
atom	charge	atom	atom-type
S	0.756	S	SDmso
N	-0.594	N	NE
C	0.304	C	CTFE
O	-0.495	O	OE
F	-0.091	F	FTFE

Experientially, however, a density of  $1313 \text{ kg} \times \text{m}^{-3}$  is reported<sup>15</sup>; the deviation corresponds to 13%. We considered 13% too large compared to densities produced by other atomistic force-fields<sup>15 16</sup> for ionic liquids. Hence, the atom-types of the carbon, fluorine and oxygen atoms were changed from initially C, F, ODmso to CTFE, FTFE and OE respectively. The effect of the sulfur atom-type and nitrogen atom type was found negligible. Thus no refinement was undertaken. Using the new atom types (cf. table 3.4b) a density of  $1327.1 (\pm 0.3) \text{ kg} \times \text{m}^{-3}$  is obtained; the deviation to experiment is only about 1% and therefore acceptable. Whereas simulation at 393K allowed slightly more efficient selection of atom-types by trial and error, the target temperature for the model should be 298.15K; 298.15 K is the reference temperature commonly used with the MARTINI force-field. At 298.15K the model with the new atom-types yielded a density of  $1396.5 (\pm 0.5) \text{ kg} \times \text{m}^{-3}$  in excellent agreement with experiment ( $1399 \text{ kg} \times \text{m}^{-3}$ <sup>15</sup>).

One deficiency of the ATB parameters are that charges and bonded parameters can be conformer dependent. In the case of TFSI for example three conformers with different charges are provided by the ATB. However, we want to study Lithium binding, which drives a conformational change. Hence to avoid such problems new partial charges were computed, which are independent of the conformer. Note that the density is only little dependent on partial charges as long as they are consistent. Hence we did not recompute the density of the ionic liquids.

Partial charges of atomistic models are somewhat taste dependent, since there is no unique way of partitioning the electron density into atomic contributions. Usually it is good practice to use similar charges to those used in the force-field development. With the target force-field in this case it is not possible, because the charges are empirical; they are adjusted to fit a set

of thermodynamic properties.<sup>5</sup> Nevertheless any reasonable set of charges should be good enough. Thus the TFSI charges were calculated from the DFT based electron-density using the charge-model 5 (CM5) developed by Marenich and coworkers.<sup>4</sup> The CM5 model is specifically trained against reproducing dipole moments of small molecules and properties of charged ions. In addition it is very little basis set dependent and less conformer dependent than other models.<sup>4</sup> Due to these characteristics it is an ideal choice for TFSI, which has a fairly large charge delocalization<sup>1</sup>. In addition as discussed in the next section, TFSI has a rich set of conformers. Table 3.4a shows the final charges. One should note that the raw charges are already nearly symmetric; the final charges are balanced in the third digit to obtain exact identical charges for the same atoms.

## Dihedral Potential TFSI

Once the atom-types and charges were determined, the dihedral profile needed to be refit. TFSI has two important dihedral angles; these dihedral angles are defined as the angle between the two planes spanned by the C—S bond and N—S bonds and the reverse couple (cf. fig. 3.1a). Sometimes these two dihedral angles are also described solely in terms of a single dihedral angle (C-S-S-C); the distribution of this dihedral angle is a measure for the population of the two most stable conformers.<sup>17</sup> These two dominant conformers have also been identified experimentally for the TFSI anion at low salt concentration in ethers (e.g. dimethoxyethane or triglyme).<sup>18</sup> In simulations using polarizable force-fields it was found that upon Lithium binding the CIS conformer increases.<sup>17</sup> These results are in agreement with the IR measurements<sup>19</sup>. In the dilute regime, Lithium binding occurs through a bidentate coordination with two of the oxygens at different sulfurs. This forces a dihedral angle close to 90 degree for both angles resulting in the so called CIS form. Due to this conformational change upon Lithium binding it is important to fit an accurate dihedral profile. If this is not done, the Lithium binding might be over or underestimated depending on the energy difference between the two conformers; the intrinsic energy difference (i.e. without dihedral angle potential) arises mostly from steric hindrance, but is often not representative of the true barrier.

A simple QM based computation of the potential energy profile along

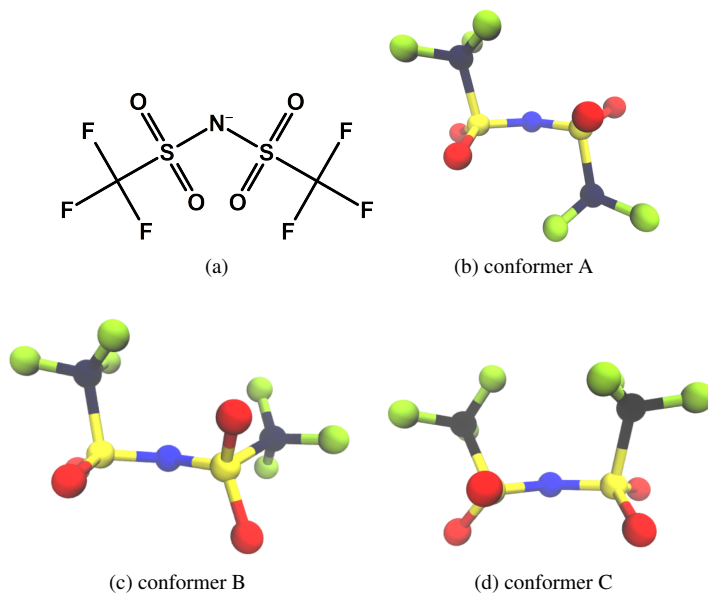


Figure 3.1: Chemical structure of TFSI (a) and three conformers along one dihedral turn of the S-N-S-C dihedral (b-d)

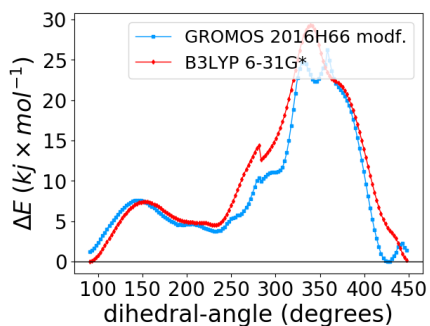


Figure 3.2: Potential energy profile along one dihedral turn starting from the CIS conformer

the rotation of one dihedral has proven difficult due to the strong coupling of the two dihedral angles; forward rotation gave a significantly different

profile than backward rotation. Hence, we chose to first compute all stable conformers along one dihedral rotation starting from the CIS conformer (3.1b), because that one is relevant in Lithium binding. We found three local minima along such path (cf. fig. 3.1b-3.1d). At these minima the other dihedral angle remains close to the initial value in CIS conformer (around 90 degrees). The energy differences between the three minima is the primary target for our parametrization of the dihedral angle.

In order to obtain a dihedral angle potential in MD, which at least qualitatively reflects these energy differences, a restricted QM scan was performed. This scan consisted of rotating only one dihedral while actively constraining the other; the so obtained profile is independent of the rotation direction and does not contain the response of the other dihedral (cf. 3.2 red line). Subsequently a MD potential was fit to this profile (cf. 3.2 blue line). Unfortunately this match did not immediately lead to the correct ordering of the energies of the three conformers in MD. Hence it was decided to apply a small dihedral restraint (simple harmonic oscillator potential) with a minimum located at 90 degrees. This additional restraint shifts the energies with respect to the global minimum and forces the correct ordering. Now the energy differences are acceptably close, while the overall rotational profile is not affected too much. In addition this potential can be applied to both dihedral angles without loss of generality. It should be noted that the molecule has more dihedral angles. However, the ATB only defined one more set of dihedral angles namely along the F-C-S-N axis; this dihedral restraints the CF<sub>3</sub> rotation. We observe also a strong coupling of this dihedral to the rest of the molecule and no extensive rotation of the CF<sub>3</sub> group. Hence, a term for this dihedral angle was omitted.

As an additional validation we simulated LiTFSI at low concentrations in triglyme. At such concentrations the salt is mostly dissociated from the anion. The ratio (R) of CIS to TRANS conformer was estimated as the ratio of the two distinct IR signals from each conformer ( $R \approx 0.25 \pm 1$ );<sup>18</sup> the ratio from the distribution (cg. fig. 3.3) of the dihedral angle in our simulation is about 0.13 in good agreement with experiment. The shape of the distribution showing a large peak at around 150 degrees and a smaller around 60 degrees is also similar to the one obtained by polarizable AA simulations.<sup>17</sup>

## Lithium TFSI interaction energy

The GROMOS force-field already has parameters for a Lithium cation. They were parametrized against single-ion solvation free energies in wa-

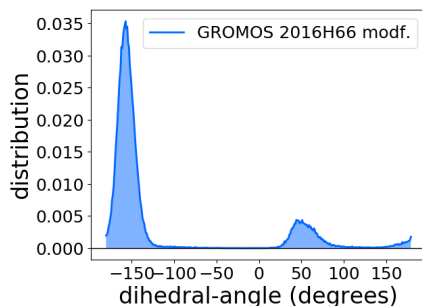


Figure 3.3: Distribution of the C-S-S-C dihedral angle, obtained in a simulation of TFSI in triglyme at 303.15K.

ter;<sup>20</sup> we assumed that such procedure already yields a rather accurate guess of the interaction energies. In previous simulations and experimental studies on LiTFSI in ethers, it was observed that the anions and cations exist in essentially two forms. In the first form they are completely separated from each other by solvent molecules; this form is called solvent separated ion pairs (SSIP). In the second form one Lithium ion is associated to one TFSI anion forming the so called contact-ion-pair (CIP).<sup>21 22</sup> At higher concentrations multiple CIPs can form salt crystal like aggregates.

Experimentally the relative amount of these two forms have been studied by Raman spectroscopy. Upon binding of Lithium Brouillette et al. observed a distinct shift in the Raman band of the TFSI anion. This shift is different depending on the amount of cations bound to TFSI and their binding position.<sup>21</sup> Hence one can distinguish the types of Lithium anion pairs formed and based on the signal intensities one can also distinguish their relative populations (at least up to an unknown factor). Appendix C offers some more detail of the shift of the Raman bands based on QM calculations. Our QM calculations are consistent with the shift of the Raman bands to higher intensity upon Lithium binding. Furthermore they show the intensities are not fully equivalent but close. Hence we assume that the intensities are directly proportional to the populations CIPs and SSIPs in solution.

Simulations of DXE LiTFSI mixtures with about 20mol% salt using the original parameters, showed quick aggregation of the salt into clusters of more than one anion and cation. This behavior is entirely at odds with experiment.<sup>21</sup> As a consequence we further refined the TFSI-oxygen Lithium interaction parameter by matching the relative amount of free to coordinated anions in the low concentration range (10mol%-30mol%). To change

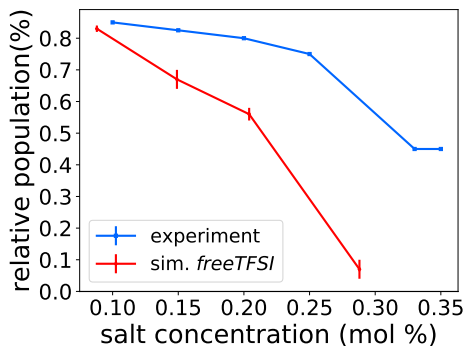


Figure 3.4: relative amount of SSIPs (i.e. free TFSI) in DXE measured in experiment<sup>21</sup> (blue) and MD simulations (red)

the interaction strength a new atom-type, called OT, was introduced. The OT type possesses the same interaction parameters with all other atoms as the OE type, but has an increased C12 parameter for the interaction with Lithium ions.

Increasing the C12 parameter from originally  $5.73375 \times 10^{-8}$  to  $1.23375 \times 10^{-7}$  yielded a more reasonable amount of free anions. Figure 3.4 shows the percentage of free Lithium ions in DXE as a function of concentration for our simulation using the refined parameters (red) and experiment (blue). Whereas the agreement is not perfect, the overall behavior greatly improves over the original case in three respects: (1) At low concentration Lithium is mostly free; (2) with increasing concentration Lithium becomes singly coordinated by at most one TFSI ion in agreement with experiment; (3) Over the entire concentration range only few complexes of Lithium with more than 1 TFSI are observed. Additionally the peak of the RDF Lithium-Oxygen RDF is located at  $0.23\text{\AA}$ , in reasonable agreement with previous simulations ( $\approx 2.0\text{\AA}$ ).<sup>17,22</sup> While there remains certainly room for improvements of the LiTFSI model, we are confident that the refinements presented here are sufficient to parametrize a coarse-grained model for LiTFSI.

## MARTINI LiTFSI

Free ions (i.e. not part of a molecule) in MARTINI 2 are normally considered to possess a solvation shell, which implicitly accounts for the size of the ion.<sup>9</sup> However, in the case of LiTFSI both anion and cation cannot

be assumed to have an implicit solvation shell. After all, we want to simulate the dynamic self-assembly process, which also implies the dynamic coordination of ions. In fact dynamic coordination should be possible to mimic the effect of the ions on the segregation strength. Therefore we seek to parametrize a "bare" cation and anion.

Using the atomistic model as reference the coarse-grained model was developed by (a) matching the angle and dihedral distributions of atomistic TFSI in triglyme, (b) reproducing the mixing properties of low concentrations of LiTFSI in DXE, and (c) reproducing the mixing properties of LiTFSI in Benzene. DXE was selected as it resembles the PEO polymer phase and Benzene, because it is the bulk solvent and representative of the PS phase.

## Mapping and Bonded Interactions

Since Lithium is a single ion the mapping can only be a single bead. Therefore it does not have any bonded interactions. However, the TFSI anion is rather large and therefore needs to be mapped by multiple beads. It was decided to map TFSI into four beads (cf. fig. 3.5a) retaining the C-S-S-C dihedral also presented in the real ion.

In MARTINI bonds between beads are normally fit to represent the distance between the center-of-mass of the atoms, which are represented by the two beads respectively. However, the distance is rather short for the SC4-SQa bond (0.247 nm) and also for the SC4-SQa bond (0.277 nm). Thus constraints were used instead of bonds and the non-bonded interactions between all beads were excluded; this measure is necessary to obtain a stable model. It is not expected that the lack of a flexible bond will significantly affect the self-assembly or in general LiTFSI properties.

Furthermore, the CG model of TFSI has two angles (SC4-SC4-SQa and SQa-SQa-SC4); these are represented by a simple harmonic angle potential. Figure 3.5b and 3.5c show the atomistic and CG distributions of both angles. Except for the small peak at around 80 degrees and 120 degrees, respectively, the agreement is very well. Since we do not expect the overall conformations of TFSI to influence the phase-separation much or the charge transport strongly, this match was considered acceptable.

The dihedral potential of TFSI was represented by a simple cosine based dihedral potential. As in the atomistic model a restraint potential was added to generate a bimodal distribution with preference for one distribution. Figure 3.5d shows the distribution of the C-S-S-C dihedral for the atomistic model and the coarse-grained model. While the initial agreement was fairly good, it was noticed later that in long simulations ( $\sim 100$  ns) the

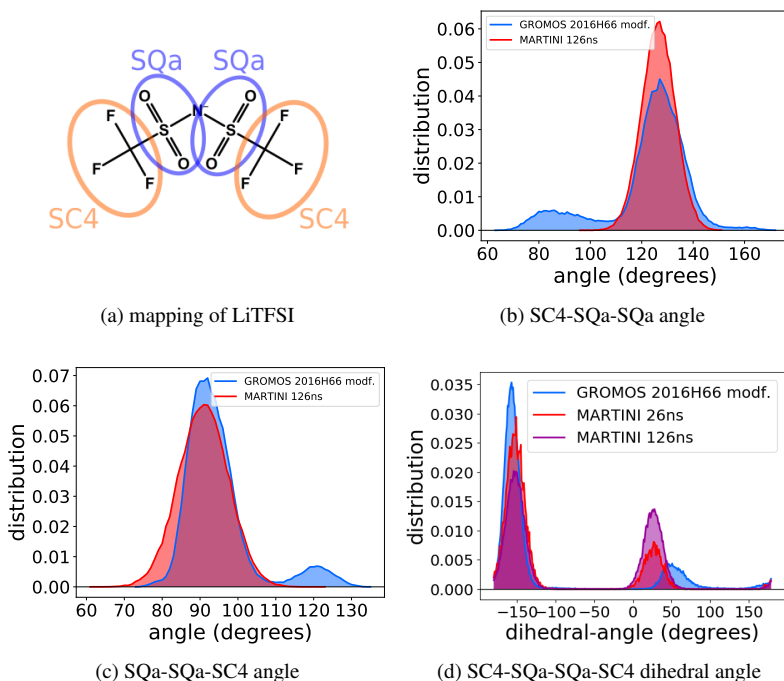


Figure 3.5: Mapping of LiTFSI in MARTINI and angle (a,b) as well as dihedral distributions shown for the coarse-grained (red, purple) and atomistic model (blue).

distribution tends to show two peaks almost equal in size. In other words the restraint is too weak to distinguish the two conformers. Since the equilibration of the distributions was initially not noticed, the dihedral potential was not improved any further. Whereas this is an unfortunate result, we do not expect that it changes the self-assembly process or charge transport properties adversely. As shown next, the phase properties can still be represented accurately.

## Non-bonded interactions

Usually the non-bonded interactions in MARTINI are based on selecting an appropriate bead-type, which reproduces an accurate free energy of transfer

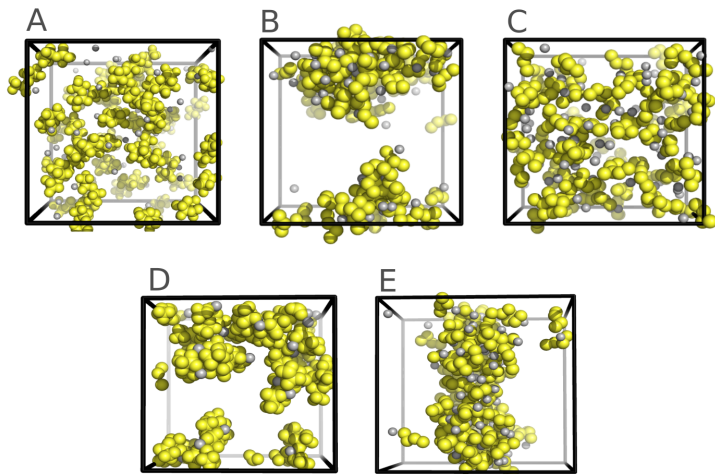


Figure 3.6: Mixtures of LiTFSI with dimethoxyethane (A-C) and Benzene (D-E), the solvent is omitted for clarity. Lithium is depicted gray while TFSI is shown in yellow. Panel A shows the simulation of DXE and LiTFSI at atomistic level while B and C correspond to MARTINI before and after the refinement process. Panel D corresponds to atomistic level LiTFSI in Benzene while panel E shows the corresponding MARTINI simulation.

(cf. eq. 3.2) obtained from experiment or atomistic simulations.

$$\Delta\Delta G_{transfer(A \rightarrow B)} = \Delta G_{solv(A)} - \Delta G_{solv(B)} \quad (3.2)$$

On the other hand MARTINI also offers some qualitative guidelines for selecting bead-types.<sup>9</sup> Since Lithium and TFSI have a full charge the interaction should be modeled by beads of the Q type. Furthermore as Lithium cannot undergo hydrogen bonding and is small, the SQ0 type is the most appropriate. In contrast TFSI is fairly large, so it was represented by four beads. In principle TFSI could undergo hydrogen bonding via the sulfur oxygens. Hence the middle two beads were selected to be of the SQa type; the outer two beads, representing the CF<sub>3</sub> moiety, were given the SC4 types, because they involve halogens and the group is neutral. The TFSI beads are all small, because the groups are branched and fluorines are rather small in terms of their vdw-radius anyways.

To verify that this assignment of beads yields reasonable properties, we

simulated mixtures of the salt in different solvents and matched the phase properties. Although this is more crude than computing partition free energies, it is nevertheless reminiscent of them; when the salt aggregates in one solvent whereas it does not in the other, it means the transfer from one to the other is favored. In this study we have chosen dimethoxyethane and Benzene as solvent, because the former is representative of the conducting polymer phase while the other solvent is the actual solvent for the assembly; it is hoped by obtaining the correct association dissociation behavior in the two separate solvents that in the combined case the salt will go to the PEO phase but not form large aggregates within the phase.

Figure 3.6 shows LiTFSI in DXE for the atomistic case (a), the unrefined CG model (b), and the refined CG model (c). One can clearly see that in the atomistic case the salt is not aggregated much nor phase-separated, in agreement with experiment.<sup>21</sup> In contrast the unrefined MARTINI model clearly shows phase-separation and large aggregation of ions.

To get a more quantitative feeling for the degree of phase-separation one can compute the contact-fraction (cf. 3.1). It is a measure for the degree of mixing of (normally) two liquids.<sup>12</sup> However, it is possible to extend the concept to the salt at hand without problems. When the salt forms clusters (i.e. phase-separates) the TFSI will have increased contact with itself compared to the solvated case. Thus a low contact fraction indicates phase-separation, whereas a high contact fraction indicates mixing; at ideal mixing (i.e. fully random distribution of neighbours) the contact fraction assumes a value of the molfraction of the solvent.

The contact fraction of dimethoxyethane and TFSI for the atomistic case (3.6 panel A) is  $0.2768 \pm 0.0003$ . In contrast the original coarse-grained MARTINI model yielded a contact fraction of  $0.1601 \pm 0.0002$ ; this significantly lower number indicates more aggregation than in the atomistic simulation, which is also seen from the snapshots. Hence it was decided to refine the interactions of DXE (2 EO beads) by setting the salt EO interactions attractive ( $\epsilon = 4.5$ ) and decreasing  $\sigma$  to 0.33 nm. The new refined model yields a contact fraction of  $0.2137 \pm 0.0004$  in better agreement with the atomistic simulation. It is possible that the interactions should be even more attractive to enhance mixing, however, as the interactions are already very favorable compared to the rest of the MARTINI interaction table no further adjustment was undertaken.

The contact fractions in the case of Benzene and TFSI are both lower than the ones in DXE; for the atomistic case a value of  $0.0970 \pm 0.003$  is obtained and coarse-grained case a value of  $(0.0688 \pm 0.0002)$ . Both are in good agreement and indicate a larger degree of salt association, which is

consistent with the snapshots shown in figure 3.6.

## Conclusion

A parametrization for an atomistic and coarse-grained model of LiTFSI was presented. During the parametrization special attention was given to the dissociation behavior in DXE (representative of PEO) and Benzene (bulk solvent and representative of PS). The atomistic TFSI was parametrized by (a) matching relative energies of conformers obtained from QM calculations, (b) matching the dihedral rotation profile from QM calculations, and (c) reproducing the density of ionic liquids. Subsequently the Lithium TFSI interaction was refined by reproducing qualitatively the experimental salt dissociation populations in dimethoxyethane. Based on this atomistic model the coarse-grained model was developed by (a) matching the angle and dihedral distributions of atomistic LiTFSI in triglyme and selecting appropriate bead types. While the mixing properties of LiTFSI at low concentrations in Benzene matched atomistic simulations, the interactions with the new EO bead were refined to reproduce the mixing properties in DXE.



# References

- [1] Savoie, B. M.; Webb, M. A.; Miller, T. F. *Journal of Physical Chemistry Letters* **2017**, *8*, 641–646.
- [2] Young, N. P.; Devaux, D.; Khurana, R.; Coates, G. W.; Balsara, N. P. *Solid State Ionics* **2014**, *263*, 87–94.
- [3] Malde, A. K.; Zuo, L.; Breeze, M.; Stroet, M.; Poger, D.; Nair, P. C.; Oostenbrink, C.; Mark, A. E. *Journal of chemical theory and computation* **2011**, *7*, 4026–4037.
- [4] Marenich, A. V.; Jerome, S. V.; Cramer, C. J.; Truhlar, D. G. *Journal of Chemical Theory and Computation* **2012**, *8*, 527–541.
- [5] Horta, B. A.; Merz, P. T.; Fuchs, P. F.; Dolenc, J.; Riniker, S.; Hünenberger, P. H. *Journal of Chemical Theory and Computation* **2016**, *12*, 3825–3850.
- [6] Parrinello, M.; Rahman, A. *Journal of Applied Physics* **1981**, *52*, 7182–7190.
- [7] Goga, N.; Rzepiela, A. J.; de Vries, A. H.; Marrink, S. J.; Berendsen, H. J. C. *Journal of Chemical Theory and Computation* **2012**, *8*, 3637–3649.
- [8] Bussi, G.; Donadio, D.; Parrinello, M. *The Journal of Chemical Physics* **2007**, *126*, 014101.
- [9] Marrink, S. J.; Risselada, H. J.; Yefimov, S.; Tieleman, D. P.; De Vries, A. H. *Journal of Physical Chemistry B* **2007**, *111*, 7812–7824.
- [10] de Jong, D. H.; Baoukina, S.; Ingólfsson, H. I.; Marrink, S. J. *Computer Physics Communications* **2016**, *199*, 1–7.
- [11] Horta, B. A.; Fuchs, P. F.; Van Gunsteren, W. F.; Hünenberger, P. H. *Journal of Chemical Theory and Computation* **2011**, *7*, 1016–1031.
- [12] Barnoud, J.; Rossi, G.; Marrink, S. J.; Monticelli, L. *PLoS computational biology* **2014**, *10*, e1003873.
- [13] Canzar, S.; El-Kebir, M.; Pool, R.; Elbassioni, K.; Malde, A. K.; Mark, A. E.; Geerke, D. P.; Stougie, L.; Klau, G. W. *Journal of Computational Biology* **2013**, *20*, 188–198.

- [14] Koziara, K. B.; Stroet, M.; Malde, A. K.; Mark, A. E. *Journal of computer-aided molecular design* **2014**, *28*, 221–233.
- [15] Borodin, O. *The journal of physical chemistry. B* **2009**, *113*, 11463–78.
- [16] Lopes, J. N. C.; Padua, A. A. H. *J. Phys. Chem. B* **2004**, *108*, 16893–16898.
- [17] Haskins, J. B.; Bennett, W. R.; Wu, J. J.; Hernández, D. M.; Borodin, O.; Monk, J. D.; Bauschlicher, C. W.; Lawson, J. W. *The Journal of Physical Chemistry B* **2014**, *118*, 11295–11309.
- [18] Herstedt, M.; Smirnov, M.; Johansson, P.; Chami, M.; Grondin, J.; Servant, L.; Lassegues, J. C. *Journal of Raman Spectroscopy* **2005**, *36*, 762–770.
- [19] Gejji, S. P.; Suresh, C. H.; Babu, K.; Gadre, S. R. *The Journal of Physical Chemistry A* **1999**, *103*, 7474–7480.
- [20] Reif, M. M.; Hünenberger, P. H. *The Journal of chemical physics* **2011**, *134*, 144104.
- [21] Brouillette, D.; Irish, D. E.; Taylor, N. J.; Perron, G.; Odziemkowski, M.; Desnoyers, J. E. *Physical Chemistry Chemical Physics* **2002**, *4*, 6063–6071.
- [22] Callsen, M.; Sodeyama, K.; Futera, Z.; Tateyama, Y.; Hamada, I. *Journal of Physical Chemistry B* **2017**, *121*, 180–188.

## Chapter 4

# Self-Assembly and Charge Transport of LiTFSI in PS-*b*-PEO

“ *Problems worthy of attack prove their worth by hitting back.* ”

”

---

Piet Hein,

## Introduction

Solid Polymer Electrolytes have been of great interest in the field of battery research, since it was discovered that specific polymers can solvate and also conduct ions. One of the most studied polymers in this respect is Polyethylene oxide (PEO). However, it has one major drawback: The shear modulus is too low to prevent the formation of Lithium crystals upon multiple cycles of recharging.<sup>1</sup> A solution to this problem has been to link PEO covalently with a non-conducting polymer that has a higher shear modulus (e.g. Polystyrene PS). When combined in the appropriate ratio the copolymer (e.g. PS-*b*-PEO) self-assembles into ordered morphologies. Whereas the mechanical stability can be improved, combination of the two polymers often goes hand in hand with a decrease in conductivity. As the synthesis of novel block-copolymers and their testing is time consuming, understanding and predicting the conductivity in such systems would be of great use to enhance the research in this area. In the past there have been

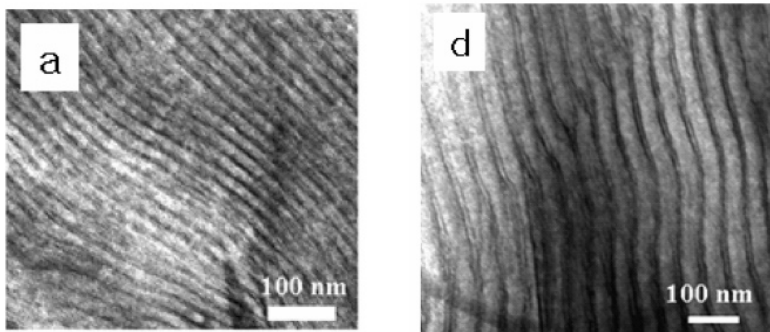


Figure 4.1: Lamella phases of PS-*b*-PEO at two different chain lengths (a:  $PS_{16}PEO_{16}$ , d:  $PS_{40}PEO_{54}$ ) imaged by TEM. taken from<sup>2</sup>

some studies on the conduction mechanism in pure PEO mostly based on molecular-dynamics simulations.<sup>3,4,5</sup> One of the drawbacks of all studies is the limited time-scale. As they are MD simulations at atomistic or even polarizable atomistic level, the computational effort is large and it is hardly possible to reach the time-scales necessary to study ion-conduction; normally diffusion of ions in these simulations is very slow ( $10^{-7} s \times cm^{-2}$ ). A second drawback is the fact that the force-fields often comprise only a limited number of molecules. Thus combination of different polymers or

salts may require a tedious parametrization.

In contrast quite recently there has also been progress in the matter of predicting conductivities based on simplified models. The group of Miller et al. have developed a bond-percolation model that can be used as part of a generic algorithm to predict conductivity.<sup>6</sup> Although their model is based on identifying high conductivity by means of observing a high mean-square-displacement (MSD) of the ions, a blind test has shown that the model does not predict an accurate qualitative ordering of the MSD values in experiment. However, the conductivities in fact did follow the trend suggested by the model. Thus the authors concluded the methodology still produces usable results.<sup>7</sup> Both problems of time-scale and force-field parametrization, become even more severe when dealing with block-copolymer systems. One of the most recent multi-scale studies employed a three step protocol: (1) bonded interactions of a simple bead spring model were determined by inverse Boltzmann coarse-graining of the homo-polymer melts; (2) interactions between PS and PEO beads are simple effective interaction parameters based on segregation strength ( $N\chi_{eff}$ ). (3) Lamella phases were equilibrated and back-mapped to atomistic resolution.

This procedure has advantages, such as easy selection of effective interaction parameters;  $N\chi_{eff}$  is available from experiment. Another advantage is not having to deal with explicit electrostatic interactions in the CG force-field. However, this approximation also has disadvantages: For studying the salt transport the ions need to be reintroduced into the simulation at a later stage. This has been done by randomly placing the ions into the phase-separated block-copolymer.<sup>8</sup> Although Sethuraman et al. presented some evidence, which suggest some degree of equilibration has taken place, it is also clear that the simulations did not reach the stage of linear diffusion. It therefore remains uncertain, if the salt distribution is truly equilibrated. Another disadvantage in respect to in-silico prediction of conductivities is that atomistic MD simulations are very costly for large systems.

Considering the alternative options MARTINI presents a promising third way: MARTINI includes parameters for ions and therefore the equilibration can be achieved in a very natural way when the morphology forms. In addition, as MARTINI is a coarse-grained force-field, it can reach time-scales required for studying ion transport. In this study we combine the existing MARTINI model of Polystyrene (PS)<sup>9</sup> with the new MARTINI model of PEO presented in this thesis to yield a model for the block-copolymer (PS-b-PEO); each polymer separately has been verified to reproduce experimental observations under various conditions. LiTFSI will be used as salt and the parameters were presented in the preceding chapter. As detailed

in the method section all simulations are conducted at chain lengths and a salt concentration as previously used by Yuan and coworkers in their experimental study.

## Methods

### CG-simulations

The self-assembly of PS-b-PE was simulated using a step-wise solvent removal procedure as used by Alessandri et al. in the context of OPVs<sup>10</sup>; the procedure mimics the experimental procedure of solvent evaporation. Starting point for the evaporation procedure was an initial box with z-dimension exceeding the x-y dimensions, It contained PS-b-PEO, LiTFSI, and Benzene as solvent. Subsequently the solvent was removed in a step-wise fashion consisting in removing a fixed percentage of solvent molecules, simulating for 0.5ns under constant volume, pressure and temperature (NVT), followed by a longer simulation under  $Np_zT$  conditions; the z dimension of the pressure was coupled using a compressibility of  $3 \times 10^{-4} \text{bar}^{-1}$  while the x-y dimension was kept fixed. The resulting structure was used as starting point for the next solvent removal. During the removal procedure temperature and pressure were kept constant using the velocity-rescale thermostat by Bussi et al.<sup>11</sup> and the Parinello-Rahman barostat respectively<sup>12</sup>. All simulations were conducted at 298.15K and 1 bar pressure. Table 4.1 gives an overview over the simulations and other details such as length and percentage of evaporated solvent per step.

The MARTINI force-field version 2 with the parameters for the PS-b-PEO copolymer developed in chapter two was used throughout the simulations. Refined parameters for the ions were used as developed in chapter 3. Following de Jong et al. electrostatic and Lennard-Jones interactions were cut-off at 1.1 nm in combination with using the Verlet neighborlist scheme.<sup>13</sup> It should be noted that MARTINI is usually used with a dielectric constant of 15 to make up for non-existent partial charges. This dielectric constant has been specifically chosen in the context of water.<sup>14</sup> However, we deal with a mostly organic system for which the dielectric constant is lower. The charged-bead LJ interaction parameters were designed in part to make up for non-existent partial charges as well. However, they assume a dielectric constant of 15. Thus changing the dielectric constant to some lower value could lead to larger repulsion between like ions and more attraction between unlike ions. As discussed in the next section it could be

worth testing different dielectric constants and employing corrections for cutting of electrostatics, but this work also is supposed to fulfill the role of a baseline. Hence it was decided not to change the dielectric constant. Besides the evaporation simulations some of the final structures were simulated at higher temperature; this simulation is equivalent to experimental annealing. The simulations used slightly different setups shown in table 4.1. During these simulations pressure and temperature coupling was the same as used before.

Table 4.1: Evaporation simulations

PEO-PS $M_N$	ID	polymer mol%*	$\epsilon_{PS-PEO}$ kJ/mol	steps	time/step ns	evap. %
75-28	A-I	$2.62 \times 10^{-3}$	2.682.	23	200	5.25
75-28	C-I	$2.62 \times 10^{-3}$	2.655	28	20	3.74
75-28	B-I	$2.62 \times 10^{-3}$	2.655	25	20	3.75
27-28	D-I	$2.91 \times 10^{-3}$	2.655	53	20	1.5
27-28	D-I	$25.83 \times 10^{-3}$	2.655	7	100	1.5
27-28	E-I	0.217	2.655	34	100	15

\* excluding ions

run D consisted of two parts

all simulations where run with  $r=0.0853$  (ions / EO beads)

Table 4.2: Annealing simulations

PEO-PS $M_N$	ID	Benzene mol%*	$\epsilon_{PS-PEO}$ kJ/mol	time ns
75-28	A-II	$4 \times 10^{-3}$	2.682	2690
75-28	B-II(298)	0.0	2.682	500
75-28	B-II(360)	0.0	2.682	500
75-28	B-III	0.0126	2.655	1600
75-28	B-IV	0.0	2.655	399
75-28	C-II	0.0086	2.655	546
27-14	n/a	0.0	2.655	298

excluding ions

all simulations where run with  $r=0.0853$  (ions / EO beads)

## Quantifying Phase-Separation

To identify phase-separation we consider only the PEO beads of the block-copolymer salt system. If a single PEO bead is surrounded by at least the same number of PEO beads as in the homo-polymer at the same salt concentration, that PEO bead is considered to be located in a region of high PEO density; this region of high PEO density is synonymous for a phase-separated region, because there is a maximum number of particles, which can surround one PEO bead. If this number is at least the one observed in the homo polymer, we are confident that no PS is around the PEO. To perform this type of analysis we employed a cluster-algorithm (DBSCAN<sup>15</sup>), which has already been used in chapter 2.

The principle of our procedure is schematically shown in figure 4.2.

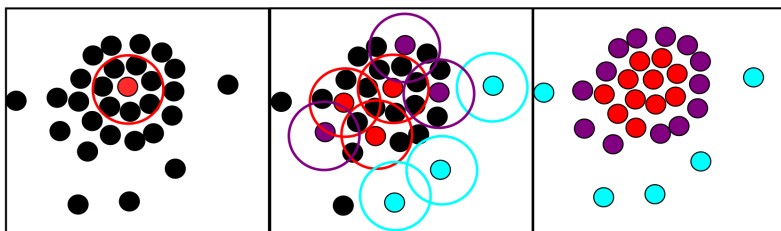


Figure 4.2: Principle of DBSCAN algorithm; red are core points, purple periphery points and cyan points not belonging to a cluster

Assume each of the points represents a PEO monomer. Further assume the empty space between not directly adjacent points is occupied by solvent or PS. Visual inspection tells us that there is one cluster of PEO monomers. However, what is the degree of phase-separation in that system? To find out we check for each point by how many neighbors it is surrounded. Panel A shows this for the most central red point. Assume our threshold is 5 points for a point to be considered in a region of high density. Clearly the red point in figure 4.2 belongs to such a region, because it is surrounded by 7 points. Next we check a few more points as shown in panel B of figure 4.2. At the periphery of our cluster we have points (purple), which are neighbors to points of high density (red), but they are themselves not surrounded by sufficient many points. Those purple points are also counted as part of the region of high density, because they are directly adjacent or connected to a region of high density. In a sense they represent the boundary. Depending on the search radius the boundary can be larger or smaller depending on the resolution one would like to obtain. Some points (cyan) are themselves not

surrounded by sufficient many other points, but are also not connected to any of the red points. These are considered to be located in mixed regions or regions of high PS density. Once the analysis has been performed the full classification is shown in panel C. The red points are in regions of high density, the purple points at the periphery and the cyan ones don't belong to regions of high density.

$$\text{phase - separation} = \frac{n_{PEO\text{-core}} + n_{PEO\text{-periphery}}}{n_{PEO\text{-total}}} \quad (4.1)$$

The phase-separation in percent can be computed as the percentage of PEO beads belonging to either the periphery or the core (cf. eq. 4.1). In the example case the system is 80% phase-separated. There are in total 26 points of which 21 are part of a region of high density and 5 are not.

Using the clustering algorithm has the additional advantage that it counts how many separate clusters there are. This gives information on how disperse the phase-separation is. For instance a system can be 100% phase-separated with spheres of one type of compound embedded in the other material. In this case a large number of clusters would be obtained for the embedded material. However, if the material is fully phase-separated and all regions connected, one would only count 1 cluster.

For the procedure to work a cut-off needs to be defined and a minimum number of beads. A cut-off of 1.1 nm was chosen consistent with the cut-off of the non-bonded interactions. To determine the minimum number of beads a melt of PEO chains with 27 repeat units and a salt concentration equal to the one used in all other instances ( $r=0.087$ ) was simulated at 360K. It was considered equilibrated when the density was converged. At 360K about 62 PEO beads surround each PEO bead within 1.1nm. The reference number at 298.15K is slightly higher (64) and was measured by cooling the melt and again equilibrating the density. The simulation parameters were the same as for the solvent evaporation simulations.

## Quantifying Salt Distribution

To establish a correlation between phase-separation and salt, the salt distribution was analyzed in terms of the increase of an ion in the phase-separated regions relative to the size of that region. If 50% of PEO monomers belong to the high-PEO density regions, we would expect to find 50% of the salts there; that is given the condition that the driving force is interaction with PEO. Hence we can define an index. This index is given by the number of ions found in high-PEO density region divided by the total number of ions,

minus the percentage of PEO monomers in that particular phase (cf. eq. 4.2). This tells us how much more ions relative to the size of the high-PEO density region are found in that region.

$$ion - increase = \frac{n_{ions-in-high-density}}{n_{ions-total}} - \frac{n_{high-density-PEO}}{n_{PEO-total}} \quad (4.2)$$

An ion is considered to be in the phase-separated region, if it is surrounded by more PEO monomers belonging to the high-PEO density region than to the depleted PEO density region. There are a few things to note about this index: (1) the interaction with the PS is by parametrization very unfavorable. Thus we do not expect the Benzene or PS to have a strong tendency to bind Lithium or TFSI. (2) At full phase-separation the index goes to zero. Thus it does not contain any information on how much salt is in the PS phase in the limit of full phase-separation. It more shows the temporal tendency of salt to be located in either phase. (3) the procedure by which the ions are classified to be in a distinct region of space is somewhat depended on the size of the interface. Hence very low numbers should be considered with a grain of salt. Nevertheless qualitative trends can be clearly distinguished.

## Self-Assembly

Figure 4.3 shows the phase-separation as function of total simulation time during the solvent evaporation of 250  $PS_{28}PEO_{75}$  chains at a salt concentration of 0.0853 (EO beads /Li beads); the three inset pictures show the entire system after the first step, the midpoint and last step, respectively from left to right. PEO is shown in red while PS is depicted in blue and Lithium is shown in cyan; TFSI is presented as yellow beads. Phase-separation is classified by regions of enhanced PEO number density as explained in the method section. When comparing the three inset pictures it is hard to spot any degree of phase-separation. This observation is in agreement with the method used to detect phase-separation: The red curve shows the percentage of PEO monomer units associated with regions of homo-polymer-like densities. It is effectively zero until the very end of the simulation when almost all solvent is evaporated; at this point the phase-separation reaches a mere 15%. Experimentally the very same systems shows lamellae phases with 100% phase-separation.<sup>16</sup>

However, as has been demonstrated by Alessandri et al. in the context of

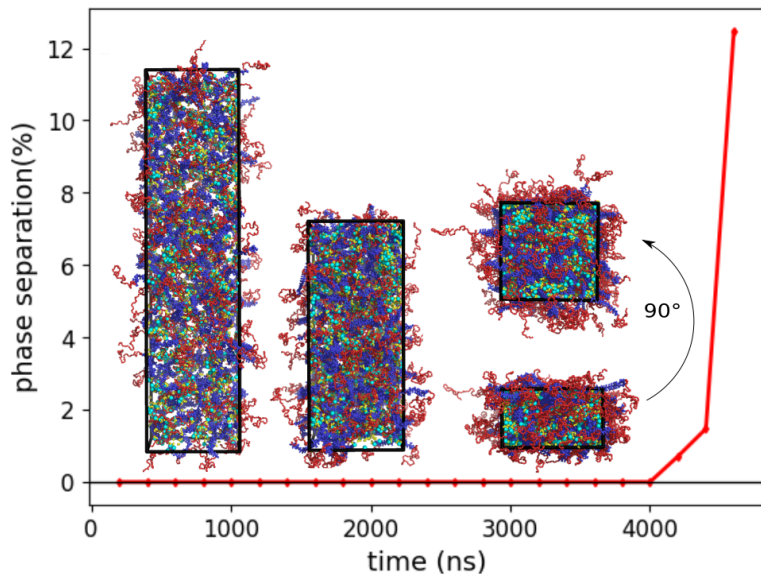


Figure 4.3: Phase-separation as function of simulation time for  $PS_{28} - PEO_{75}$  at  $r=0.0853$ ; the inset pictures show the box at the beginning, the midpoint and end of the evaporation simulation.

OPV micro-phase separated systems<sup>10</sup>, the speed of evaporation, total evaporation time, and also annealing can significantly impact the morphology. Thus it was decided to investigate several different settings to establish the best conditions for obtaining phase-separation and lamella.

However, beyond these technical settings there is one other important factor: The interactions between the PS ring unit and the PEO monomer are favorable ( $\epsilon = 2.655 \text{ kJ/mol}$ ); this was based on the observation that benzene is a good solvent for PEO. While it does not present a principle problem, it is nevertheless a conundrum, because PEO and PS are supposed to phase-separate. In this respect obtaining 15% phase-separation in the end of the first try is encouraging. However, as has been pointed out in the context of PS-b-PEO micelles in chapter 2 equilibration might be very slow; it might even be beyond the time-scales reached in coarse-grained MARTINI simulations. Hence we decided to set the interaction parameters to the same (more repulsive) level as with the PS back-bone bead (i.e.  $\epsilon = 2.27 \text{ kJ/mol}$ ). By this measure the phase-separation dynamics

are enhanced and it allows us to survey the effects of the other parameters with less effort. In the following graphs the color red is used to refer to the original parameters while blue and purple colors are used for these enhanced parameters.

## Effect of Time and Concentration

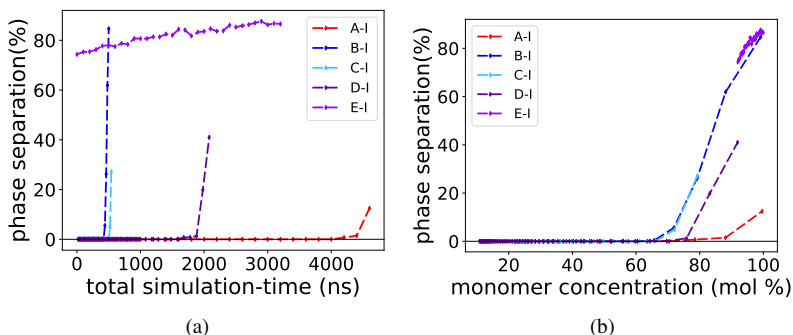


Figure 4.4: Phase-separation of  $PS_{28}PEO_{75}$  (blue, red) and  $PS_{14}PEO_{27}$  (purple) as function of total simulation time (a) and as function of concentration (b); letters indicate the specific run conditions outlined in the method section

In total 5 solvent evaporation simulations were set up. Each used a different time per step and different evaporation speeds. However, only one noticeable correlation between these different runs was found. Figure 4.4a shows the dependence of the phase-separation as function of total simulation time. The systems with the repulsive parameters has a much higher degree of phase-separation even reaching levels of 90% in two cases. However, there seems to be no correlation between the time aspect and the degree of phase-separation. Naively one could have suspected that longer simulation-times allow for a better equilibration and thus higher degrees of phase-separation. However, this hypothesis is actually disproved: For instance the first two curves are evaporations starting from the same system. In both cases each step lasts 20ns and the total evaporation time is about 500 ns. Nevertheless one system shows a phase-separation of almost 90%, while the other reaches a mere 27%. Similarly the purple curve shows

the phase-separation for the shorter block-copolymer (14-27); one should expect a higher degree of phase-separation, because shorter chains can better equilibrate and the total simulation time is longer. However, only one of the simulations reaches about 90% phase-separation, whereas the other remains at 41%. In addition almost all simulations show a rapid increase in phase-separation within only a few ten nanoseconds; in all cases this increase is towards the end of the simulation during the last 2-3 evaporation steps.

The reason for this unexpected behavior becomes apparent when plotting the same data as function of concentration of monomers to solvent (cf. fig. 4.4b); the phase-separation seems much more strongly correlated with concentration rather than time. For all cases the steps below a monomer concentration of about 70% are practically unimportant. Only above 70% monomer concentration significant phase-separation is observed for the repulsive cases. In contrast using the original parameters noticeable phase-separation can only be observed at about 90% monomer concentration. As the different simulations reach the critical concentrations in different times, there appears to be no time correlation with the phase-separation.

It is also apparent from the plot that the shorter chain seem to have a higher critical concentration, which is broadly speaking in agreement with experiment; the longer the chain the higher the segregation strength (i.e. propensity to phase-separate).

## **Correlation Salt Phase-Separation**

It is also instructive to look at the position of the Lithium-TFSI during the solvent evaporation. As it has been explained in the previous chapter salt is known to enhance the segregation strength. In fact the copolymers sampled here are not known to phase-separate unless the salt is added.<sup>16</sup> Hence we would expect a correlation between the salt and the regions, which are phase-separated.

Figure 4.5a shows the relative increase of Lithium with respect to the size of the phase-separated regions as function of concentration for the different simulations. For all simulations but one a decrease of Lithium in the phase-separated part is observed followed by a sharp increase. The out-lier simulation shows already enhanced Lithium over the entire concentration range. Because the increase in Lithium appears at around the critical concentration, there appears to be a clear correlation between phase-separation, critical concentration and an increase of Lithium in the PEO phase.

The big question is whether Lithium drives self-assembly or whether the

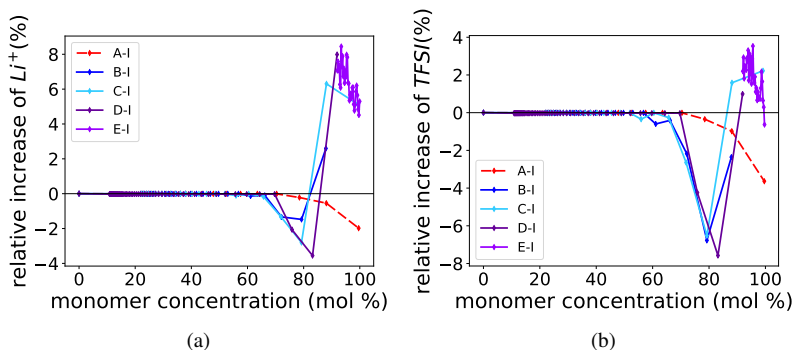


Figure 4.5: Relative increase of Lithium (a) and TFSI (b) with respect to the size of the phase-separated region for  $PS_{28}PEO_{75}$  (blue, red) and  $PS_{14}PEO_{27}$  (purple); letters indicate the specific run conditions outlined in the method section

phas-separated parts preferably absorb Lithium. It remains unclear what the causalities are. Nevertheless it is encouraging that Lithium shows an over-proportional tendency to be located in the phase-separated parts, because that confirms: Lithium globally prefers a PEO like environment in agreement with the recent study of de Pablo and coworkers.<sup>17</sup>

## Annealing

Usually in experiment but also in simulations annealing (i.e. the increase of temperature to dry the specimen) is a common procedure to enhance phase-separation and equilibration. We have conducted several simulations with increased temperature (360K) corresponding to the temperature used in experiment.<sup>16</sup> Figure 4.6a shows the degree of phase-separation for the six different simulations. Simulation A-II (using only original parameters) shows a phase-separation of about 17%, which is constant in time. This is an increase of about 5% with respect to the morphology directly obtained from evaporation. In contrast starting from a morphology obtained using the repulsive interactions and then real interaction parameters, the phase-separation decreases from around 80% to 60% within 500ns (B-II(390K)). Therefore using the original interaction parameters a large degree of phase-separation seems not to be the favored state. On the other hand when

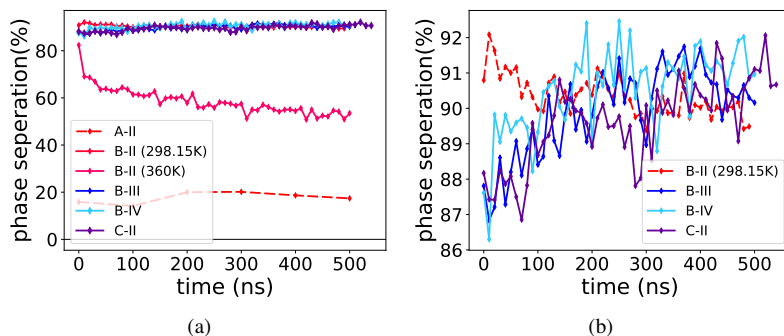


Figure 4.6: Phase-separation during annealing; the red curves represent simulations making use of the original PS-PEO interaction parameters and the blue samples of the repulsive interactions.

starting from a initially quite phase-separated structures and running at room temperature the decrease is much smaller (*sim* 3%). Therefore at 360K mixing is favored, whereas at room temperature phase-separation can be maintained. For practical purposes it might be feasible to generate phase-separation using repulsive interactions and then switch to the original interactions. However, from a theoretical point of view it would be more appealing to find a set of parameters that are based in the partitioning of the monomers, but also foster phase-separation; and potentially lead to long-range structural ordering.

The blue lines in figure 4.6a (repulsive PEO-PS interactions) show no large variation in degree of phase-separation with annealing time. They are about 90% phase-separated and the phase-separation only slightly increases. Thus the morphology is insensitive to residual Benzene and generally displays large phase-separation.

The only characteristic which slightly changes is the connectivity. So far assessment of phase-separation has been in global terms of total number of monomers associated to a region of high density. However, how many regions are there? The answer to this question tells us about the connectivity of the morphology; if the number of clusters (i.e. region of high densities) is 1, all regions of phase-separated PEO are connected. If there is more than 1 cluster it means that PS completely surrounds these regions with no connection. For example in case of simulation A-II and B-II the decrease in phase-separation goes hand in hand with an increase in clusters reminiscent

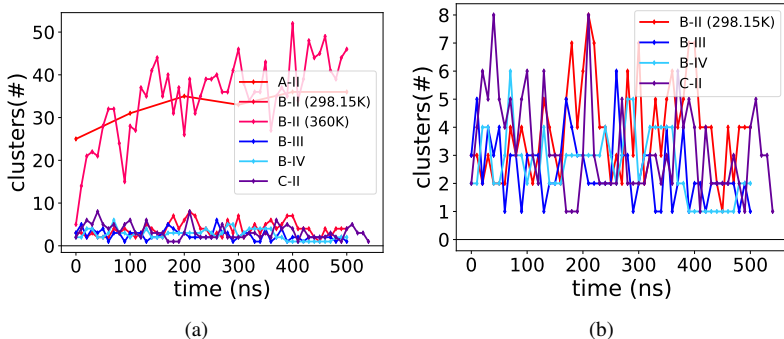


Figure 4.7: Number of regions of increased PEO density (cluster) as function of simulation time during annealing. Panel b is a zoom into the bottom region of panel A; the red curves represent simulations making use of the original PS-PEO interaction parameters and the blue samples of the repulsive interactions.

of a more disperse morphology (cf. 4.7a).

All simulations employing repulsive parameters have only few clusters (cf. fig. 4.7a). 4.7b shows a zoom into this region; the number of clusters fluctuates below 8 but in the end most morphologies end up with less than 3 clusters. In combination with the phase-separation this means: We have almost 100% of PEO located in regions of density comparable to the melt and they are largely connected. Whereas this generally is consistent with a lamellar phase, visual inspection shows no clear lamella (cf. fig 4.8). Nevertheless as shown in figure 4.8a there are continuous channels of PEO free space, which is consistent with an overall phase-separation and also some from of long-range assembly. Whether these structures could be reminiscent of other phases remains unknown.

The reasons why long-range structural order is not observed will be discussed in the following paragraph. However, before it is important to mention that for all cases the salt concentration is increased during annealing relative to the amount of PEO in the annealed phase. Visual examples of this correlation are shown in figure 4.8); they are also in agreement with the method employed before. On the one hand this confirms the correlation of salt and phase-separation. On the other hand it also illustrates that salt dynamics are slow, because the trend of relative salt increase is not converged within 500 ns. In part this is due to the not converged degree

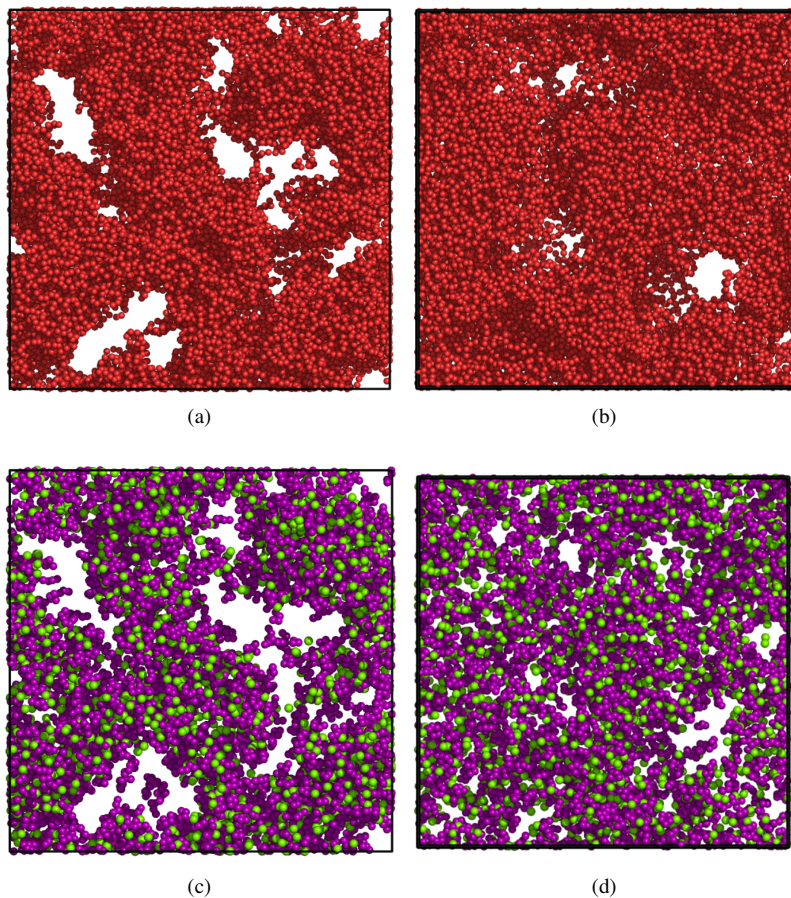


Figure 4.8: Final Snapshots of the morphology obtained after annealing with the repulsive parameters for PS and PEO for the chain length  $PS_{14}PEO_{27}$  (a) and  $PS_{28}PEO_{75}$  (b); for clarity only the PEO (a,b) or the (c,d) is shown.

of phase-separation. However, it might in part also be caused by slow salt diffusion. Overall this poses the question, if atomistic simulations are even able to reach an equilibrated salt distribution.

## Transport Properties

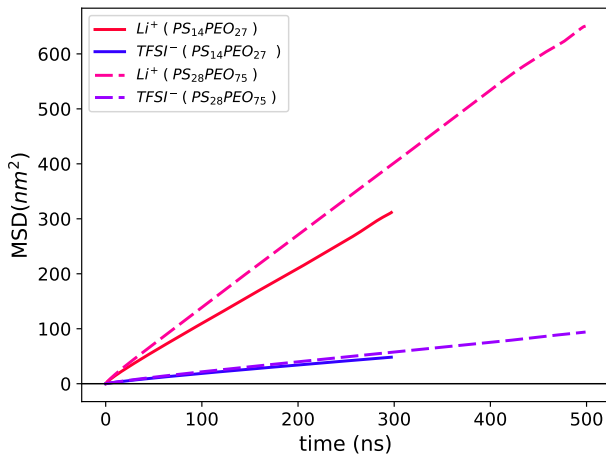


Figure 4.9: MSD of Lithium and TFSI during annealing at 360K.

Figure 4.9 shows the mean-squared-displacement of the Lithium and TFSI ions at 360K utilizing the repulsive PS-PEO interactions. The MSD is linear and hence diffusion is in the normal Einstein regime; therefore we have no trouble accessing the time-scales important for simulating accurate transport properties. This is the great advantage of MARTINI over other force-fields and simulation methods with explicit salt. However, in both cases the MSD of Lithium is larger than that of the TFSI anion. Although intuitively one would suspect that the significantly larger anion diffuses slower, it has been shown experimentally that TFSI diffuses much faster than Lithium.<sup>18</sup> Unfortunately MARTINI is not able to capture this effect neither in the case of normal nor repulsive chain parameters. Presumably the interaction between PEO and Lithium is still too weak compared with the less strong LJ interactions of the TFSI with PEO.

Next we can also compare the MSD for two different chain lengths. The dashed lines in figure 4.9 correspond to a shorter PS-b-PEO chain while the thick lines correspond to the longer chains; we see the MSD of both Lithium and TFSI is larger for the longer chains. From linear response theory we know that the conductance ( $\lambda$ ) can be related to the diffusion

coefficient of the anion ( $D_-$ ) and cation ( $D_+$ ) (cf. eq. 4.3).<sup>19</sup>

$$\lambda = \frac{N \times e^2 \times z^2}{k_B \times T \times V} \times \frac{1}{2} \times (D_+ + D_-) \quad (4.3)$$

Equation 4.3 is strictly speaking only valid, if the correlated motion of anions and cations is negligible. However, it is nevertheless sometimes applied in the context of finite salt simulations to estimate the conductance.<sup>19 18 20 4</sup> Using this approximation, the conductance for the longer chain is higher, because both diffusion coefficients are larger for the longer chain. In this case we don't report the specific value of the conductance, because that would anyways be largely influenced by morphology and preparation techniques. However, already the qualitative trend is the opposite than observed in experiment.<sup>16</sup>

While both the ordering of anion with respect to cation diffusion and the ordering of diffusion with chain length are incorrect, one important feature is encouraging nevertheless: MARTINI is able to produce different diffusions for different chain lengths irrespective of morphology. This effect is consistent with experiment and could pose a starting point for improving the description of the ion to yield better properties.

## Conclusion & Outlook

The previous simulations have shown: (1) Phase-separation is only seen at high concentrations of PEO; (2) Large phase-separation (i.e. > 70%) is only observed when using repulsive parameters between PEO and PS; (3) upon annealing more long-range phase-separation is obtained for the repulsive parameter set, whereas it decreases for the original parameter set; (4) it exists a clear correlation between phase-separation and an increase of LiTFSI in the phase-separated PEO domains; (5) anion and cation diffusion is in the linear regime albeit showing the reverse trend to experiment; (6) the diffusion is clearly influenced by chain length although again in opposite fashion as observed in experiment. Overall two questions remain: Why are no lamella or other long-range structural patterns observed? Why are the qualitative transport properties wrong? Both questions are related and might present different aspects of the same problem. We shall give three explanations, which may guide the way to a more refined mode:

- **The volume fractions in experiment do not match the volume fractions of our PS-b-PEO model.** It has been shown theoretically that the phase-diagram of a PS-b-PEO copolymer as a function of composition and chain length looks like a parabola.<sup>17</sup> In MARTINI the volume occupied by PS and PEO relative to each other might be different from one assumed in the experimental studies.<sup>16</sup> In addition we operate in the weak segregation limit, because the degree of polymerization is low and hence  $N\chi T$  is small. Both effects taken together might cause a shift in the phase-diagram from about 50% volume fraction. If that shift is sufficiently large, one enters into regions of no phase-separation or into regions that are very close to the phase-boundary. In these regions phase-separation could be suppressed or simply not be the most stable state. Comparing atomistic molecular density maps to those of our polymer could shed light on this phenomenon.
- **The long-range salt effects are missing.** It has been hypothesized by de Pablo and coworkers that differences in the local dielectric constant lead to a preference of LiTFSI for the PEO phase. In turn PS is excluded from these regions as to keep a high dielectric constant.<sup>17</sup> Since electrostatic effects are long ranged, global-phase-separation is observed; this leads to the characteristic phase-diagram. Based on CG simulations utilizing a Born solvation-free-energy with spatially varying dielectric constant de Pablo et al. were able to reproduce the phase-diagram of block-copolymers. Because MARTINI does not normally employ long-range electrostatics, only local phase-separation (i.e. within 1.1 nm) might be facilitated originating from the repulsive ion-PS interactions.
- **The dielectric constant is incorrect.** With respect to the previous argument the question arises, if the standard MARTINI dielectric screening of 15 is still appropriate. After all this dielectric constant was chosen based on properties in water, but our system only has much less polar components, which have a lower dielectric constant.<sup>14</sup>

- **Chain reptation is missing.** It is known that for good equilibration and Lithium transport in melt phases reptation of chains can be important.<sup>3 17</sup> Because these moves are normally implemented using Monte-Carlo, using MARTINI with GROMACS does not include this type of motion. Seeing that the phase-separation seems to only occur at high concentration of polymers almost as in the melt, equilibration and formation of long-range structural order, might simply be inhibited by this lacking component. However, there would still be the possibility of enhancing sampling by replica exchange or some form of Hamiltonian exchange; the latter could partially utilize a Hamiltonian with very repulsive interactions or effective parameters.



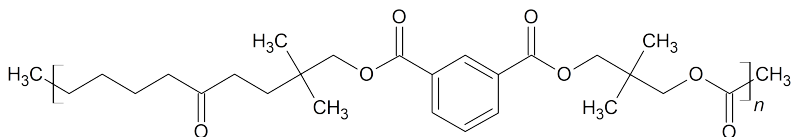
# References

- [1] Xue, Z.; He, D.; Xie, X. *J. Mater. Chem. A* **2015**, *3*, 19218–19253.
- [2] Singh, M.; Odusanya, O.; Wilmes, G. M.; Eitouni, H. B.; Gomez, E. D.; Patel, A. J.; Chen, V. L.; Park, M. J.; Fragouli, P.; Iatrou, H.; Hadjichristidis, N.; Cookson, D.; Balsara, N. P. *Macromolecules* **2007**, *40*, 4578–4585.
- [3] Diddens, D.; Heuer, A.; Borodin, O. *Macromolecules* **2010**, *43*, 2028–2036.
- [4] Chattoraj, J.; Knappe, M.; Heuer, A. *The Journal of Physical Chemistry B* **2015**, *119*, 6786–6791.
- [5] Diddens, D.; Heuer, A. **2012**,
- [6] Webb, M. A.; Savoie, B. M.; Wang, Z.-G.; Miller III, T. F. *Macromolecules* **2015**, *48*, 7346–7358.
- [7] Zheng, Q.; Pesko, D. M.; Savoie, B. M.; Timachova, K.; Hasan, A. L.; Smith, M. C.; Miller, T. F.; Coates, G. W.; Balsara, N. P. *Macromolecules* **2018**, *acs.macromol.7b02706*.
- [8] Sethuraman, V.; Mogurampelly, S.; Ganesan, V. *Macromolecules* **2017**, *50*, 4542–4554.
- [9] Rossi, G.; Monticelli, L.; Puisto, S. R.; Vattulainen, I.; Ala-Nissila, T. *Soft Matter* **2011**, *7*, 698–708.
- [10] Alessandri, R.; Uusitalo, J. J.; De Vries, A. H.; Havenith, R. W.; Marrink, S. J. *Journal of the American Chemical Society* **2017**, *139*, 3697–3705.
- [11] Bussi, G.; Donadio, D.; Parrinello, M. *The Journal of Chemical Physics* **2007**, *126*, 014101.
- [12] Parrinello, M.; Rahman, A. *Journal of Applied Physics* **1981**, *52*, 7182–7190.
- [13] Jong, D. H. D.; Singh, G.; Bennett, W. F. D.; Wassenaar, T. a.; Sch, L. V.; Periole, X.; Tieleman, P.; Marrink, S. J. *Journal of Chemical Theory and Computation* **2012**, *9*, 687–697.
- [14] Marrink, S. J.; Risselada, H. J.; Yefimov, S.; Tieleman, D. P.; De Vries, A. H. *Journal of Physical Chemistry B* **2007**, *111*, 7812–7824.

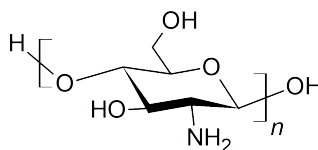
- [15] Ester, M.; Kriegel, H.-P.; Sander, J.; Xu, X. A Density-Based Algorithm for Discovering Clusters in Large Spatial Databases with Noise. KDD'96 Proceedings of the Second International Conference on Knowledge Discovery and Data Mining Pages. Portland, Oregon, 1996; pp 226–231.
- [16] Yuan, R.; Teran, A. A.; Gurevitch, I.; Mullin, S. A.; Wanakule, N. S.; Balsara, N. P. *Macromolecules* **2013**, *46*, 914–921.
- [17] Chu, W.; Qin, J.; De Pablo, J. J. *Macromolecules* **2018**, *51*, 1986–1991.
- [18] Savoie, B. M.; Webb, M. A.; Miller, T. F. *Journal of Physical Chemistry Letters* **2017**, *8*, 641–646.
- [19] Müller-Plathe, F. *Acta Polymerica* **1994**, *45*, 259–293.
- [20] Müller-Plathe, F.; Van Gunsteren, W. F. *The Journal of Chemical Physics* **1995**, *103*, 4745–4756.

# **Appendix A**

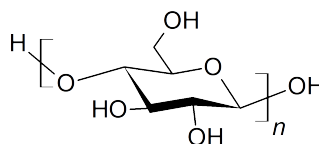
# **Polymer Structures**



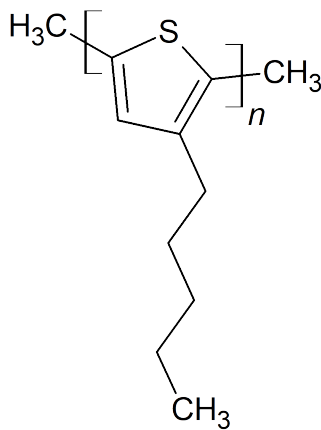
(a) (one) polyster-resin



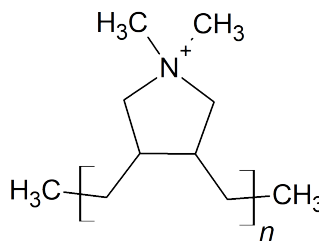
(b) Chitosane



(c) Poly-Glucose



(d) P3HT



(e) PDADMA

Figure A.1: Structures of Polymers that are available within the MARTINI-Force-Field

## Appendix B

# 2016H66 with the Verlet cut-off scheme and modifiers

The 2016H66 force-field was originally developed using the GROMOS molecular dynamics code with a twin-range cut-off scheme based on charge groups.<sup>1</sup> As such a twin-range cut-off is not available in GROMACS. Although the charge group scheme is still implemented it does not profit from the performance enhancement in modern versions of GROMACS. Therefore, we have decided to use the force-field (FF) with the Verlet cut-off scheme and also use modifiers for the Coulomb and Lennard-Jones (LJ) potential to accelerate the calculations. To verify that these changes do not substantially change the properties of the force-field, the heats of vaporization and densities for all solvents were computed. Table B.1 shows the heats of vaporization of the different solvents for experiment (exp.), the original settings used in the parametrization (original) and our new run settings with GROMACS. Overall the heat of vaporization increases in most cases by +1-2 kJ/mol. However, the difference to experimental heats of vaporization is still below +1.8 kJ/mol. Since the shift is consistent in one direction, it is not expected that these run settings affect the partition free energies adversely. In addition, we report the density of all solvents (cf. tab. B.2) and the solvation free energy of dimethoxy ethane in different solvents (cf. tab. B.3).

Table B.1: Heats of vaporization of different solvents using the 2016H66 force-field

Solvent	$\Delta H_{vap}$ exp. (kJ/mol)	$\Delta H_{vap}$ this work (kJ/mol)	$\Delta H_{vap}$ original (kJ/mol)
Octane	41.49*	$40.5 \pm 0.3$	n/a
Benzene	33.9	$32.9 \pm 0.3$	30.99
Propanol	47.49	$49.2 \pm 0.1$	47.86
Propanethiol	31.89	$31.0 \pm 0.1$	30.07
Acetone	31.3	$33.1 \pm 0.1$	31.13
Butanol	52.7	$53.9 \pm 0.3$	52.7
Cyclohexane	33.334*	$31.8 \pm 0.1$	n/a

\* taken from ref.<sup>2</sup>\*\* taken from ref.<sup>3</sup>

Table B.2: Densities of different solvents using the 2016H66 force-field

Solvent	$\rho$ exp. ( $kg \times m^{-3}$ )	$\rho$ this work ( $kg \times m^{-3}$ )	$\rho$ original ( $kg \times m^{-3}$ )
Octane	698.6*	$699.0 \pm 0.2$	n/a
Benzene	873.6	$882.2 \pm 0.5$	877.76
Propanol	799.6	$779.0 \pm 0.2$	783.12
Propanethiol	833.0	$854.1 \pm 0.2$	867.66
Acetone	784.4	$819.8 \pm 0.3$	811.78
Butanol	805.75	$788.0 \pm 0.2$	791.2
Cyclohexane	778.1**	$771.0 \pm 0.2$	n/a
Propylamine	712.1	$714.8 \pm 0.2$	726.4

taken from ref.<sup>2</sup>\*\* taken from ref.<sup>4</sup>All other experimental values are taken from the original work.<sup>1</sup>

Table B.3: Solvation Free Energies

Solvent	$\Delta G_{SOL}$ 2016H661	$\Delta G_{SOL}$ Lee model	$\Delta G_{SOL}$ Rossi model	$\Delta G_{SOL}$ this work
Water	$-20.48 \pm 0.2$	$-24.39 \pm 0.05$	$-29.34 \pm 0.05$	$-14.73 \pm 0.05$
Octane	$-13.16 \pm 0.02$	$-10.43 \pm 0.04$	$-10.48 \pm 0.04$	$-7.25 \pm 0.04$
Benzene	$-20.69 \pm 0.03$	$-14.67 \pm 0.06$	$-14.39 \pm 0.06$	$-14.67 \pm 0.06$
Propanol	$-19.00 \pm 0.03$	$-28.31 \pm 0.04$	$-38.25 \pm 0.04$	$-11.69 \pm 0.04$
Propanethiol	$-22.70 \pm 0.05$	$-26.18 \pm 0.03$	$-26.06 \pm 0.03$	$-16.76 \pm 0.03$
Acetone	$-21.70 \pm 0.04$	$-22.86 \pm 0.04$	$-41.43 \pm 0.04$	$-15.77 \pm 0.04$
Butanol	$-18.26 \pm 0.07$	$-19.00 \pm 0.04$	$-38.03 \pm 0.04$	$-11.58 \pm 0.04$
Cyclohexane	$-13.69 \pm 0.03$	$0.44 \pm 0.06$	$0.30 \pm 0.05$	$-6.07 \pm 0.05$
Octanol	n/a	$-24.24 \pm 0.04$	$-29.51 \pm 0.05$	$-13.75 \pm 0.04$



# References

- [1] Horta, B. A.; Merz, P. T.; Fuchs, P. F.; Dolenc, J.; Riniker, S.; Hünenberger, P. H. *Journal of Chemical Theory and Computation* **2016**, *12*, 3825–3850.
- [2] Haynes, W. M. *CRC handbook of chemistry and physics*; CRC press, 2014.
- [3] Aston, J. G.; Szasz, G. J.; Fink, H. L. *Journal of the American Chemical Society* **1943**, *65*, 1135–1139.
- [4] O’Neil, M. J. *The Merck index: an encyclopedia of chemicals, drugs, and biologicals*; RSC Publishing, 2013.



## Appendix C

# Error and Convergence Estimation

In this work, we estimate the error and assess the convergence based on the time-series analysis utilities available in the pymbar package (<https://www.github.com/choderalab/pymbar>).<sup>1,2</sup> A script utilizing pymbar and implementing the analysis methods described below is available online ([https://github.com/fgrunewald/tools\\_for\\_MD\\_analysis](https://github.com/fgrunewald/tools_for_MD_analysis)). Here we briefly summarize the main points of the theory and methods for estimating the error and assessing the convergence.

It is important to note that the error of an ensemble average obtained from MD is not representative of the true error, because MD simulations produce correlated data sets. It can be shown that the standard-error in the mean (SEM) of the true uncorrelated data set is larger than those of the correlated data set by a factor of  $\sqrt{g}$ . The quantity  $g$ , called the statistical inefficiency, is a measure for how much smaller an uncorrelated data set is, with respect to the correlated data set. Stated differently, the ratio of  $\frac{N_{\text{correlated}}}{g}$  is roughly equal to the number of uncorrelated samples:<sup>1</sup>

$$N_{\text{uncorrelated}} \approx \frac{N_{\text{correlated}}}{g} \quad (\text{C.1})$$

Thus,  $g$  provides a connection between the correlated data set obtained directly by MD and the corresponding uncorrelated data set. To estimate the error in an observable such as the radius of gyration, we first estimate the statistical inefficiency ( $g$ ) using the method suggested by Shirts and Chodera in the context of free energy calculations.<sup>1</sup> Subsequently, to obtain

an approximate uncorrelated data set, the original data set is sub-sampled at intervals of length  $n \times g$ . In this case  $n$  is increased by 1 until the length of the data set is exceeded. This method is itself already part of the pymbar package. The average and standard error of this uncorrelated data set are reported. In almost all cases, the error estimate was found to be identical to the one obtained by the method suggested by Hess<sup>3</sup>, which is implemented in the "gmx analyze" utility provided with the GROMACS package. Since  $g$  is also related to the dominant auto-correlation time of the system by:<sup>4</sup>

$$g = 1 + 2\tau \tag{C.2}$$

we can use the same procedure to assess convergence. Obtaining sufficiently many uncorrelated samples (i.e. the ratio  $\frac{N_{\text{correlated}}}{g}$  is large; that is  $N_{\text{correlated}} \gg \tau$ ) ensures, at least in principle, that the simulation is longer than the autocorrelation time. Unfortunately, molecular systems in general, but also simulations of polymers in particular, can have multiple long autocorrelation times. However, the method for estimating  $g$  assumes per default, that there are sufficiently many samples. In other words, in cases of large under sampling, one may obtain a smaller autocorrelation time than the one relevant for the system. To combat this problem, we plotted the mean with error-bar as fraction of simulation time as well as the estimate of  $\tau$ . Whereas for most systems  $\tau$  converged after sufficiently long times, there are selected cases for which it did not. In such cases, we note that the change in the mean and the error converge. Hence, we conclude that these simulation are sufficiently converged. To double check, we also applied the tool by Hess<sup>3</sup>, which estimates two autocorrelation times and found a similar to identical errors.

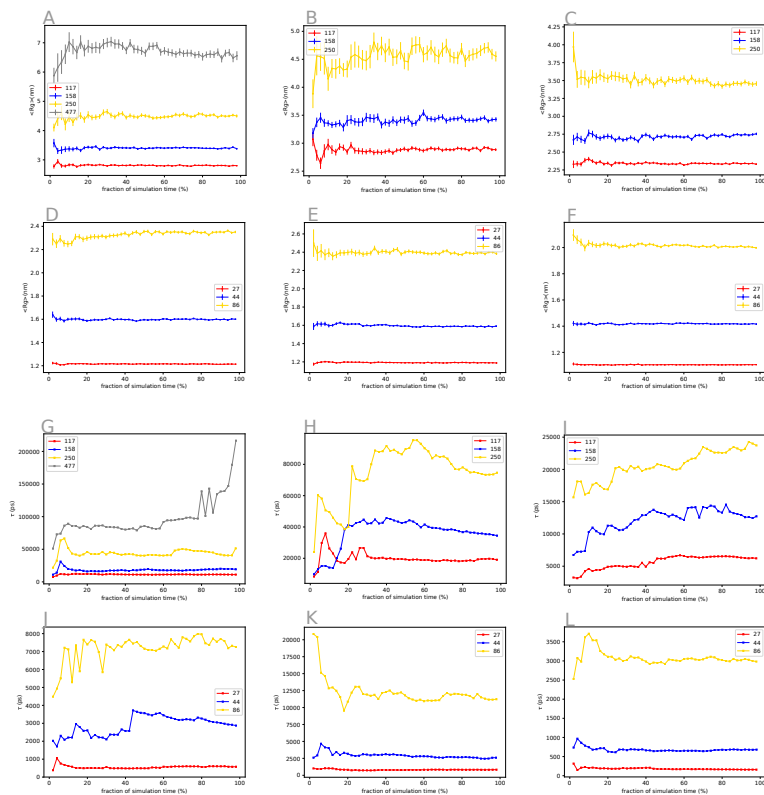


Figure C.1: Radii of gyration from single chain simulations as a function of simulation time (panel A-F) and corresponding autocorrelation time estimates (panel G-L). The plots in the first column (A,D,G,I) are for simulations in Water, the second column (B,E,H,K) for simulations in Benzene, and the third column (C,F,I,L) for simulations in Diglyme.



# References

- [1] Shirts, M. R.; Chodera, J. D. *Journal of Chemical Physics* **2008**, *129*.
- [2] Chodera, J. D.; Swope, W. C.; Pitera, J. W.; Seok, C.; Dill, K. A. *Journal of Chemical Theory and Computation* **2007**, *3*, 26–41.
- [3] Hess, B. *Journal of Chemical Physics* **2002**, *116*, 209–217.
- [4] Klimovich, P. V.; Shirts, M. R.; Mobley, D. L. *Journal of Computer-Aided Molecular Design* **2015**, *29*, 397–411.



## Appendix D

# Estimating the radius of gyration at low molecular weights

### Extrapolation from high molecular weights

One method for estimating polymer radii of gyration at molecular weights too low for direct scattering experiments, consist in extrapolating from high molecular weight radii of gyration. To obtain the radius of gyration in water and triglyme, we extrapolated using the following equations.

$$R_G = (4.08 \times 10^{-18} M_w^{1.16})^{0.5} \times 10^7 \text{ in } H_2O \quad (D.1)$$

$$R_G = (1.11 \times 10^{-17} M_w^{1.01})^{0.5} \times 10^7 \text{ in } Triglyme \quad (D.2)$$

These fitting relations were obtained from the fits presented by Kawaguchi et al.<sup>1</sup> by converting from  $cm^2$  to nm. One should note that extrapolations often span several orders of magnitudes. To single out potential problems due to these wide ranges, we used a second method for estimating low molecular weight radii of gyration, outlined below.

### Estimation based on intrinsic viscosity data

There are multiple ways to obtain the radius of gyration ( $\langle R_G^2 \rangle^{1/2}$ ) of a polymer in a good solvent from viscosity measurements. Here we present a

simple procedure, applicable when intrinsic viscosity data is available for a polymer in a  $\theta$ -solvent and in a good solvent at the same molecular weight. In general, the radius of gyration ( $\langle R_G^2 \rangle^{1/2}$ ) in a good solvent is related to the radius of gyration in a  $\theta$ -solvent ( $\langle R_G^2 \rangle_\theta^{1/2}$ ) by an expansion factor ( $\alpha$ )<sup>2</sup>:

$$\langle R_G^2 \rangle^{1/2} = \langle R_G^2 \rangle_\theta^{1/2} \times \alpha \quad (\text{D.3})$$

Using this equation, we can calculate the radius of gyration by first getting the radius of gyration under theta conditions (i.e. for an ideal chain) and then multiply it by the appropriate expansion factor. The radius of gyration in the  $\theta$ -solvent can be calculated from the Flory-Fox equation, with  $K$  being the Flory-Fox constant.<sup>2,3</sup>

$$\langle R_G^2 \rangle_\theta^{1/2} = \frac{K}{\Phi_\theta}^{\frac{1}{3}} \times M_w^{1/2} \quad (\text{D.4})$$

And following Flory and coworkers<sup>2</sup>, the expansion factor can be written in terms of the intrinsic viscosities ( $[\eta]$  and  $[\eta_\theta]$ ) in both solvents:

$$\alpha^\gamma = \frac{\Phi_{theta}}{\Phi} \times \frac{[\eta]}{[\eta_\theta]} \quad (\text{D.5})$$

In the above equation  $\gamma$ ,  $\Phi_{theta}$ , and  $\Phi$  are constants. We will address the nature and value of these constants in more detail below. Combining the above three expressions yields an equation for the radius of gyration in terms of the Flory-Fox constant and the viscosity of the good solvent and  $\theta$ -solvent:

$$\langle R_G^2 \rangle^{1/2} = \frac{K}{\Phi_\theta}^{\frac{1}{3}} \times M_w^{1/2} \times \frac{\Phi_{theta}}{\Phi} \times \frac{[\eta]}{[\eta_\theta]}^{\frac{1}{\gamma}} \quad (\text{D.6})$$

To simplify this expression we will suppose, following Flory<sup>2</sup>, that the viscosity constant  $\Phi$  is the same in the  $\theta$ -solvent and the good solvent (i.e.  $\frac{\Phi_\theta}{\Phi} = 1$ ) and given by the value of  $3.67 \times 10^{24} \text{ mol}^{-1}$ .<sup>4</sup> This leads to the following equation, in which only the value of  $\gamma$  and the Flory-Fox constant ( $K$ ) need to be defined, while the ratio of the intrinsic viscosities ( $\frac{[\eta]}{[\eta_\theta]}$ ) can be taken from experiment.

$$\langle R_G^2 \rangle^{1/2} = \frac{K}{\Phi_\theta}^{\frac{1}{3}} \times M_w^{1/2} \times \frac{[\eta]}{[\eta_\theta]}^{\frac{1}{\gamma}} \quad (\text{D.7})$$

For the constant  $\gamma$ , a value of 3.0 is often used.<sup>4,5,2</sup> The value of this constant was based on fits to experimental data only. In general, the best value to

be used for different systems is not clearly defined. Since we made the approximation of  $\frac{\Phi_\theta}{\Phi} = 1$ ), a value of 2.5 was suggested by Flory as being more applicable for the case of PEO in water.<sup>2</sup> We will discuss the effect of this choice below, after completing the description of the procedure for estimating an error bar on the so calculated radius of gyration.

The intrinsic viscosity values, which we used, were not reported with an explicit error estimate. However, we can try to estimate a lower bound to the error by estimating  $K$  and the error therein from the viscosity measurements in a  $\theta$ -solvent.  $K$  is related to the intrinsic viscosity by:

$$K = [\eta_\theta \times M_w^{-1/2}] \quad (\text{D.8})$$

In principle  $K$  should be a constant. Thus, the standard error in  $K$  reflects, to some extent, the uncertainty in the viscosity measurements. Based on the data by Kawaguchi et al.<sup>1</sup> and by Booth and Beech<sup>6</sup>, we computed a value of  $0.17 \pm 0.01 \text{ cm}^3 \text{ g}^{-1/2} \text{ mol}^{1/2}$ . The error propagates linearly into the final equation such that the error in the radius of gyration is given by:

$$\delta \langle R_G^2 \rangle^{1/2} = \delta K \times \frac{1}{3} \times \frac{1}{\Phi_\theta} \times \frac{K}{\Phi_\theta}^{\frac{-2}{3}} \times M_w^{\frac{1}{2}} \times \left( \frac{[\eta]}{[\eta_\theta]} \right)^{\frac{1}{7}} \quad (\text{D.9})$$

Figure S1.1 shows the radii of gyration obtained by using the two different values for  $\gamma$  in the case of the two good solvents, water and benzene. The required intrinsic viscosity values were taken from Kawaguchi and coworkers.<sup>1</sup> For all points, the error bars estimated by the above method are smaller than the size of the symbols, but in all cases they overlap. In the case of water, we also show a line corresponding to an extrapolation from high molecular weight. It is apparent that using a value of 3.0 for  $\gamma$  does not change the radii of gyration significantly. Thus, we shall report and compare to the set of values obtained by  $\gamma = 2.5$  exclusively.

Table S3.1 shows the estimated radii of gyration alongside the radii of gyration obtained from extrapolation and simulation. One should note that the error in the intrinsic viscosity based values is only a lower bound and likely to be higher. The extrapolated values were rounded to the same significant digit as the viscosity based values for a better comparison, but have no explicit error estimate.

Table D.1: Radius of gyration of PEO in three different solvents at different molecular weights, alongside with the extrapolated value and the viscosity-based value whenever available.

Solvent	$M_N$	$\langle R_G^2 \rangle^{1/2}$ MARTINI	$\langle R_G^2 \rangle^{1/2} \dagger$ extrapolated (nm)	$\langle R_G^2 \rangle^{1/2}$ viscosity (nm)
Water	27	$1.213 \pm 0.002$	1.23	n/a
Water	44	$1.600 \pm 0.005$	1.63	$1.646 \pm 0.004$
Water	86	$2.36 \pm 0.02$	2.4	$2.39 \pm 0.01$
Water	100	$2.605 \pm 0.006$	2.62	n/a
Water	117	$2.81 \pm 0.02$	2.87	$2.83 \pm 0.02$
Water	158	$3.39 \pm 0.03$	3.42	n/a
Water	250	$4.56 \pm 0.05$	4.46	n/a
Water	477	$6.6 \pm 0.2$	6.5	6.5*
Benzene	27	$1.190 \pm 0.003$	n/a	n/a
Benzene	44	$1.585 \pm 0.005$	n/a	$1.539 \pm 0.007$
Benzene	86	$2.40 \pm 0.02$	n/a	$2.11 \pm 0.01$
Benzene	117	$2.91 \pm 0.03$	n/a	n/a
Benzene	158	$3.42 \pm 0.04$	n/a	n/a
Benzene	250	$4.6 \pm 0.1$	n/a	n/a
Diglyme	27	$1.107 \pm 0.002$	1.19	$1.227 \pm 0.005$
Diglyme	44	$1.418 \pm 0.003$	1.52	$1.566 \pm 0.007$
Diglyme	86	$2.002 \pm 0.007$	2.14	$2.189 \pm 0.009$
Diglyme	117	$2.35 \pm 0.02$	2.5	$2.55 \pm 0.01$
Diglyme	158	$2.72 \pm 0.02$	2.9	$2.97 \pm 0.02$
Diglyme	250	$3.47 \pm 0.04$	3.66	$3.73 \pm 0.02$
Diglyme	250	$3.47 \pm \pm 0.04$	3.66	$3.73 \pm 0.02$

\* from scattering

# References

- [1] Kawaguchi, S.; Imai, G.; Suzuki, J.; Miyahara, A.; Kitano, T.; Ito, K. *Polymer* **1997**, *38*, 2885–2891.
- [2] Bluestone, S.; Mark, J. E.; Flory, P. J. *Macromolecules* **1974**, *7*, 325–328.
- [3] Flory, P. J.; Fox, T. G. *Journal of the American Chemical Society* **1951**, *73*, 1904–1908.
- [4] Young, R. J.; Lovell, P. A. *Introduction to polymers*; CRC press, 2011.
- [5] Colby, R. H.; Rubinstein, M. *New-York: Oxford University* **2003**, *100*, 274.
- [6] Beech, D. R.; Booth, C. *Journal of Polymer Science Part A-2: Polymer Physics* **1969**, *7*, 575–586.



## Appendix E

# Brush and Mushroom dimensions for PEG grafted to a lipid bilayer

We briefly summarize the estimation of chain dimensions in the mushroom and brush regimes, using well-established theories. We follow the notation and spirit of the book *Polymer Physics* by Rubinstein and Colby<sup>1</sup>, also recommended for more in-depth information.

### Mushroom dimensions

Chain conformations of grafted polymers belong to one of two regimes depending on the grafting density. In the low grafting density regime, known as “mushroom regime”, the chains are well separated, interact minimally, and therefore move freely within a space approximating a half-sphere. The size of this half-sphere, also referred to as “mushroom”, can be described in terms of its radius. This radius can be estimated using Flory theory and is thus equal to  $R_F$ , the so called Flory radius for a polymer in a good solvent.<sup>2</sup> The Flory radius is related to the Kuhn length ( $b$ ) of the polymer and the number of Kuhn segments ( $N$ ) by the relationship:<sup>1</sup>

$$R_F = b \times N^{\frac{3}{5}} \quad (\text{E.1})$$

This equation can be rewritten in terms of the average bond length ( $l$ ), the angle ( $\theta$ ), and the number of bonds ( $n$ ) making use of the following two

identities:

$$R_{max} = b \times N \quad (\text{E.2})$$

$$R_{max} \simeq (n \times l \times \cos(\frac{\theta}{2})) \quad (\text{E.3})$$

Note that the angle ( $\theta$ ) is  $180^\circ$  minus the average angle between two bonds. Combining these three equations and resolving for the number of Kuhn segments ( $N$ ) gives:

$$N = n \times l \times \cos(\frac{\theta}{2}) \times \frac{1}{b} \quad (\text{E.4})$$

Note that  $n$  is given by the number of backbone-bonds times the number of repeat units, which in the case of PEO leads to:

$$n = 3 \times n_{monomers} \quad (\text{E.5})$$

Substituting the definition for  $N$  into the equation for  $R_F$  yields:

$$R_F = b^{\frac{2}{5}} \times (3 \times n_{monomers} \times l \times \cos(\frac{\theta}{2}))^{\frac{3}{5}} \quad (\text{E.6})$$

## Brush dimensions

When the grafting density is high (“brush regime”), the polymer chains are close in space and repel each other; the height of the brush ( $H$ ) is larger than the radius of the mushroom ( $R_F$ ). Within a simple approach this height can be computed in terms of the Kuhn length and the grafting density using Alexander-de Gennes theory within the formulation by presented by Colby and Rubinstein.<sup>1</sup> The volume of a monomer is the approximated by  $b^3$ . Strictly speaking, this is only true for an athermal solvent. However, here we approximate water, which is a good solvent, as being athermal. It can be shown that  $b^3$  is an upper bound to the monomer volume for a good solvent.<sup>1</sup> Using these two approximations the height ( $H$ ) of a polymer brush is given by:

$$H \approx N \times \sigma^{\frac{1-\nu}{2\nu}} \times b^{\frac{1}{\nu}} \quad (\text{E.7})$$

$\sigma$  is the number of grafting points per unit area (i.e. the number of PEGylated lipid per unit area). The constant  $\nu$  is the Flory exponent and takes the value of 0.588 for good solvents such as water in the case of PEO. Substituting the definitions for  $N$  and the value for  $\nu$  into the first equation,

yields an expression for the brush height in terms of the Kuhn Length and the grafting density.

$$H = 3 \times n_{monomers} \times l \times \cos\left(\frac{\theta}{2} \times b^{\frac{3}{2}} \times \sigma^{0.65}\right) \quad (\text{E.8})$$

## Estimating the Kuhn Length

The Kuhn length was estimated from the characteristic ratio  $C_\infty$  of the chain. The value of the  $C_\infty$  for PEO at room temperature has been calculated by Flory and Mark to be 0.42 nm.<sup>3</sup> Using the appropriate conversion (see reference<sup>1</sup>), a Kuhn length of  $0.74 \pm 0.2$  nm is obtained. Note that the bond length was approximated as the average length of the O-C (0.153 nm)<sup>3</sup> and C-C bond (0.143 nm)<sup>3</sup>, which is 0.148 nm. In total PEO has three backbone bonds. The angle ( $\theta$ ) was taken to be  $70^\circ$  as done by Flory and Mark.<sup>3</sup>



# References

- [1] Colby, R. H.; Rubinstein, M. *New-York: Oxford University* **2003**, *100*, 274.
- [2] Lee, H.; Larson, R. G. *Biomacromolecules* **2016**, *17*, 1757–1765.
- [3] Mark, J. E.; Flory, P. J. *Journal of the American Chemical Society* **1965**, *87*, 1415–1423.



## Appendix F

# Dimension and Aggregation Number of Micelles

In order to compute the dimensions and aggregation numbers of the PS-*b*-PEO micelles from simulations, a small python script was made, which interfaces the python library MDAnalysis<sup>1,2</sup> (<https://www.mdanalysis.org>) with the sklearn library<sup>3,4</sup> (<https://scikit-learn.org>). The latter is a machine learning library, which offers various algorithms for generating clusters from a set of points. For this study we have chosen the algorithm DBSCAN by Ester and coworkers.<sup>5</sup> The unique feature of this algorithm is that it considers relative densities of (in this case) particles to sort the particles into clusters. The criterion for whether a particle is associated to a cluster depends on two input parameters: a minimum number of points and a cut-off. For a point to belong to a cluster it has to be surrounded by at least the minimum number of points within the cut-off and be reachable from at least one other point within the cluster by a step of at most the cut-off. We choose to take the cut-off equal to the cut-off of the non-bonded forces (i.e. 1.1 nm) and take the minimum number of samples approximately equal to the atom based cumulative number RDF at the cut-off (for PS-PEO 70). In the context of polymer micelles, this algorithm is superior to other algorithms based on the center-of-mass or minimum distances, because it does not generate artificially large micelles for cases where single chains stick out of the micelles coming close to other micelles.

In addition, it is less ambiguous to define the two input parameters (i.e. cut-off, min. particles), while it is not always clear which distance ( $\sigma$ , min(LJ) or in-between) to use for CoM or distance based clustering methods. The script is available from GitHub ([https://github.com/fgrunewald/tools\\_for\\_MD\\_analysis](https://github.com/fgrunewald/tools_for_MD_analysis)) and a jupyter notebook distributed along with it discuss the usage of the script and post-processing of the data generated by it.

# References

- [1] Gowers, R. J.; Linke, M.; Barnoud, J.; Reddy, T. J. E.; Melo, M. N.; Seyler, S. L.; Domański, J.; Dotson, D. L.; Buchoux, S.; Kenney, I. M.; Beckstein, O. MDAnalysis: A Python Package for the Rapid Analysis of Molecular Dynamics Simulations. 98 PROC. OF THE 15th PYTHON IN SCIENCE CONF. Austin, Texas, 2016; pp 98–105.
- [2] Michaud-Agrawal, N.; Denning, E. J.; Woolf, T. B.; Beckstein, O. *Journal of Computational Chemistry* **2011**, *32*, 2319–2327.
- [3] Buitinck, L.; Louppe, G.; Blondel, M.; Pedregosa, F.; Mueller, A.; Grisel, O.; Niculae, V.; Prettenhofer, P.; Gramfort, A.; Grobler, J.; Layton, R.; Vanderplas, J.; Joly, A.; Holt, B.; Varoquaux, G. **2013**,
- [4] Pedregosa, F. et al. *Journal of Machine Learning Research* **2011**, *12*, 2825–2830.
- [5] Ester, M.; Kriegel, H.-P.; Sander, J.; Xu, X. A Density-Based Algorithm for Discovering Clusters in Large Spatial Databases with Noise. KDD'96 Proceedings of the Second International Conference on Knowledge Discovery and Data Mining Pages. Portland, Oregon, 1996; pp 226–231.